PROBING IN SITU DYNAMICS OF POLYMERIC THIN FILMS BY LABEL-FREE OPTICAL TECHNIQUES

by

GARETH RAY SHEPPARD

(Under the Direction of Jason Locklin)

ABSTRACT

In this dissertation, interfacial interactions are explored using label-free optical techniques to probe the dynamics within polymer thin films. Label-free detection of interfacial interactions can be used to directly study the changes in organic thin films without adversely influencing the system by labeling with target molecules. Surface plasmon resonance (SPR) and spectroscopic ellipsometry were used to investigate these interactions by monitoring changes in thickness and refractive index at an interface due to reactions on monolayers and within polymer thin films as well as to explore polymer-solvent effects.

In order to facilitate the study of binding events particularly in organic solvents, thiolene-based microfluidic devices were coupled with surface plasmon resonance imaging (SPRI). By using commercially available materials, a robust microfluidic-SPRI device was produced using a simple fabrication scheme. This provided an integrated platform to investigate surface reactions in aqueous and organic solutions for high throughput, *in situ* analysis. Incorporation of microfluidics with SPRI allowed for direct control of the fluid dynamics within the areas of interest for interfacial tracking. A novel

linear mixer design was used to generate a controlled concentration gradient in order to determine the changes in solvent refractive index due to the presence of polymer in solution. Combining the *in situ* gradient generator with SPRI, the refractive index increment of polymers in solution can be determined using a single image.

A grating surface plasmon resonance sensor was created using blu-ray discs with a molecularly imprinted polymer. The 320 nm periodic structure on the blu-ray disc is an exemplary grating SPR sensor as it produces a single sharp plasmon when coated with a noble metal. Integrating the molecular sensing technique with grating coupled SPR has lead to the fabrication an inexpensive chemical sensor that is both selective for the imprinted target molecule and sensitive to minute refractive index changes within the polymer as binding occurs. In a parallel study, polymer-solvent effects in a thermo-responsive thin film hydrogel were investigated using spectroscopic ellipsometry. Measuring the film at multiple angles and wavelengths produces sufficient optical information to deconvolute the thickness and refractive index changes as the polymer collapses and swells in response to temperature changes.

INDEX WORDS: surface plasmon resonance, label-free optical techniques, interfacial reactions, ellipsometry, polymer thin films, microfluidics

# PROBING IN SITU DYNAMICS OF POLYMERIC THIN FILMS BY LABEL-FREE OPTICAL TECHNIQUES

by

GARETH RAY SHEPPARD

B.S., Georgia Institute of Technology, 2007

A Dissertation Submitted to the Graduate Faculty of The University of Georgia in Partial Fulfillment of the Requirements for the Degree

DOCTOR OF PHILOSOPY

ATHENS, GEORGIA

2012

PROBING IN SITU DYNAMICS OF POLYMERIC THIN FILMS BY LABEL-FREE OPTICAL TECHNIQUES

by

GARETH RAY SHEPPARD

Major Professor: Jason Locklin

Committee: Geoffrey Smith
John Stickney

Electronic Version Approved:

Maureen Grasso
Dean of the Graduate School
The University of Georgia
December 2012

## DEDICATION

I dedicate this dissertation to my family, especially my parents Jim and Kay Sheppard, who have supported me with every ounce of their being as I wandered a long way to get here. You are the reason I am part of the universe, to be able to walk amongst the trees and reflect the twinkle of the stars. My brother, Jes, who has been the cornerstone over the years, providing the stability needed to continue on. To my grandparents, Ray "Gran" and Margie "Nana" Houston as well as Jim "Bubber" and Agnes Sheppard, who always pushed my curiosity and thirst for knowledge, protecting while also letting me make the necessary mistakes. For my aunts, uncles, and cousins who have made time fly by and to help brush the dirt off when times got rough. Lastly, for Sarah Penn, who has been the keystone over the past several years as all of this hard work has come to fruition.

ACKNOWLEDGEMENTS

First and foremost, I would like to thank Dr. Jason Locklin for his patience and support over the years. Coming from an engineering background with a different mind set, Jason had his work cut out for himself to mold me into a scientist. It might have been rough at times on the way to this dissertation, but I appreciate everything he has done for me from focusing the research to instilling a motivation for constant improvement. I would also like to thank my committee members, Dr. Geoffrey Smith and Dr. John Stickney, for taking their time to provide research advice and to improve my scientific disposition. A special thank you goes to Dr. Akira Baba for stimulating several of the research projects and providing an opportunity to expand on these ideas at Niigata University. I appreciate Dr. Leidong Mao and Dr. Yiping Zhao for their guidance and willingness to help in my research endeavors. I am especially thankful for the fellow members of the Locklin Lab that were always there to provide support and constructive criticism. I would like to thank Kristen Fries, Vikram Dhende, Sara Orski, Nicholas Marshall, Shameem Abul, and Dr. Satyabrate Samanta for all the stimulating conversations and eagerness to share their intellect and friendship. A special thank you goes to Kyle Sontag, Rachelle Arnold, Eric Huddleston, and Takao Oseki for being there as a sounding board for research ideas as well as a friend to listen, offer suggestions, and to provide encouragement. I would also like to thank my fellow lab members Joe Grubbs, Jenna Bilbrey, Evan White, Anandi Roy, Jing Gao, Jeremy Yatvin, Taotao Zhu, and Nathan Usselman whose camaraderie I will never forget.

TABLE OF CONTENTS

Page

LIST OF TABLES

Page

LIST OF FIGURES

Page

# CHAPTER 1

# INTRODUCTION AND LITERATURE REVIEW

## Introduction to Polymer Thin Films

The evolution of lab-on-a-chip devices has lead to the miniaturization of a variety of analytical techniques, including biological and chemical sensing, due to the integration of microscale, parallel sensing surfaces with controlled fluid dynamics.[1-11] Optical techniques like UV-vis spectroscopy, fluorescence microscopy, surface plasmon resonance spectroscopy, and surface enhanced Raman spectroscopy are commonly employed to track the interfacial changes either directly or through chemical tagging.[2, 12-16] Through selective surface functionalization, several lab-on-a-chip devices have achieved high throughput analysis using patterned monolayer arrays.[17-21]

More specifically, self-assembled monolayers are molecules with functional head groups that will readily react with complementary groups on the surface.[22-24] Based on van der Waals forces, monolayers organize into densely packed thin films leaving terminal end groups free to react with corresponding analytes in solution.[24, 25] Monolayers have been used on a variety of surfaces to track the binding affinities of biological species such as DNA hybridization, protein-DNA interactions, and antibody-antigen binding.[10, 18, 26, 27] While self-assembled monolayers are advantageous when tracking the binding of biological molecules, the monolayer surface density limits chemical sensing due to steric crowding within the two-dimensional thin film.[25] By using

polymer thin films the surface functionality can be extended perpendicular to the surface increasing the functional area.[21, 28-32]

Homogenous polymer thin films can be created using physical deposition (physisorption) or covalent attachment to the surface by chemisorption. Physical deposition methods, such as spin coating or dip coating, exhibit weak interactions between the polymer and the surface that can lead to delamination of the film during a reaction. With similar end-group functionalities as self-assembled monolayers,[22, 23, 29, 33, 34] polymer molecules can be attached to the surface using a "grafting to" approach, as shown in Figure 1.1a. Polymer formed in solution is attached to the surface using appropriate end-group functionality to react with complementary end groups on the surface.[28, 35] However, the "grafting to" approach to creating densely packed polymer coatings is diffusion limited as the hydrodynamic radius of the coiled polymer, from solution, blocks other polymers from reacting with adjacent surface functionalities.[28, 35, 36] With large distances between tethering sites, "grafting to" has low grafting densities and is known as the "mushroom regime" of polymer coatings.[29]

In contrast, polymers can be created with higher grafting densities using a "grafting from" approach by polymerization from a surface bound initiator, as shown in Figure 1.1c. The initiator is a small molecule deposited onto the surface as a self-assembled monolayer with which monomer in solution reacts to grow polymer from the surface.[21] When the density of the polymer chain ends is high enough to alter the unperturbed solution dimensions, the polymers will reorient themselves perpendicular to the surface forming a polymer brush.[28, 36, 37] A change in the polymer occurs as a balance is reached between the entropic energy gained by a random walk configuration and the

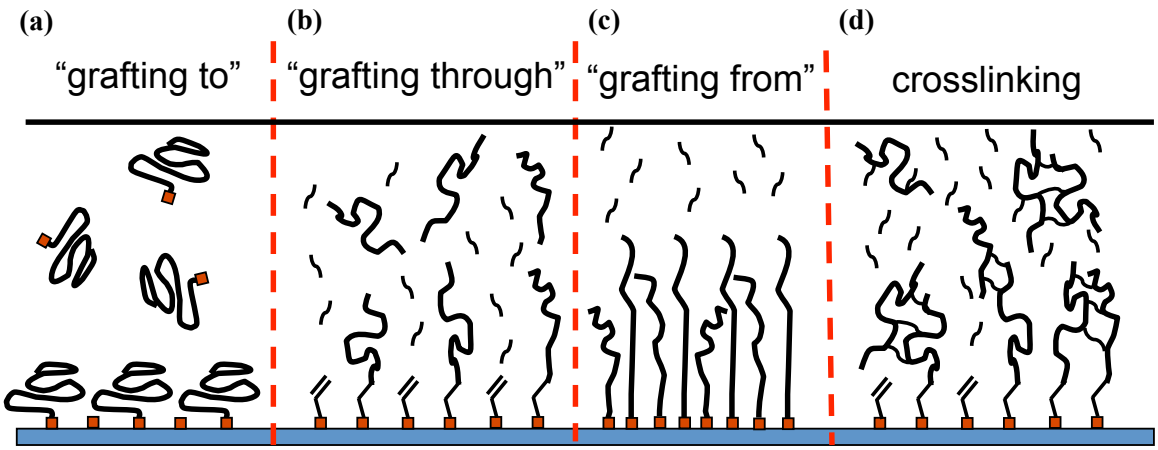


**Figure 1.1.** Grafting techniques used to tether polymers to surfaces. “Grafting to” attaches polymers made in solution to a surface. Polymers made in solution are tethered to a surface with a surface bound monomer in “grafting through.” Polymer brushes with high grafting densities are formed using the “grafting from” method. An example of crosslinking is demonstrated using “grafting through” polymerization.

energetic favorability of highly solvated, non-overlapping polymer chains.[30] Due to the excluded volume effects, the polymers in a “grafting from” reaction will grow in an extended conformation known as the “brush regime”.[38]

An intermediate approach to growing polymer brushes, known as “grafting through” uses a monolayer that is end-functionalized with a reactive monomer moiety that is used to tether the polymer to the surface as the polymerization proceeds in solution (Figure 1.1b).[39-42] This method of surface attachment has been shown to produce polymer coatings with moderate to high grafting densities. The ability to perform one-pot synthesis with “grafting through” methods can be advantageous when combined with free radical polymerization to achieve high conversion rates as molecular weight builds

rapidly before plateauing.[39] Fast polymerization is necessary when encapsulating molecules in their native state as with molecular imprinting as described in Chapter 4. In molecular imprinting, a synthetic antibody is formed by polymerizing a crosslinked network around a target molecule.[3, 43-45] Crosslinking monomers are used to reduce the mobility of polymer chains and can be used in any of the grafting methods,[39] however, Figure 1.1d shows crosslinking incorporated with "grafting through" polymerization.

**Surface Plasmon Resonance**

Surface plasmon resonace (SPR) spectroscopy has been widely utilized as a label-free detection method to study biological binding events on monolayers and within polymer thin films.[1, 10, 16, 19, 46-51] SPR is commonly implemented in the Kreteschmann configuration, where a noble metal layer is in direct contact with the glass of a prism as depicted in Figure 1.2a.[10, 46, 49, 52] The metal is either deposited directly to the bottom of the prism or onto a piece of glass. When using a glass substrate, the prism is attached to the substrate using refractive index matching fluid to create a single refractive index medium. P-polarized incident light is passed through the prism to excite surface plasmons from the backside of the noble metal layer and the reflected light is measured using a detector, typically a photodiode or CCD camera.[10] This backside reflection method is advantageous since the light does not directly interact with the medium of interest. SPR utilizes the evanescent wave created on a noble metal surface to track interfacial changes in contact with the metal layer, Figure 1.2b.[46] In order to create the evanescent wave, photons from a light source are coupled to the noble metal by matching the wave vector of the incident photon with that of the surface plasmon. This is accomplished only when the p-polarized light is totally internally reflected within the

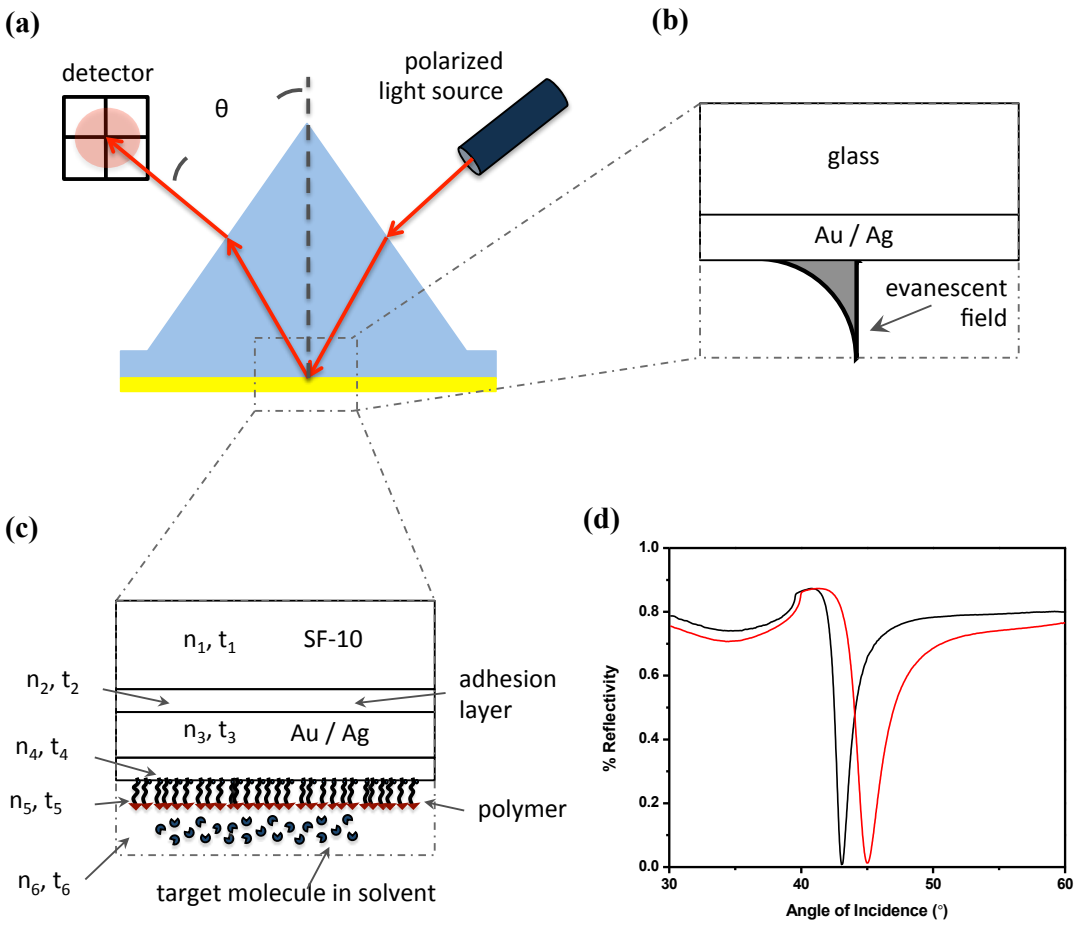


**Figure 1.2.** Surface plasmon resonance setup using the Kretschmann configuration. a) P-polarized light is coupled to the surface of the noble metal layer using a prism to match the wave vector of the incident photons with surface plasmons. b) The evanescent wave created by SPR decays into the dielectric medium and is sensitive to thickness and refractive index changes near the interface. c) Standard layer model for SPR substrates presented in this work where the addition of each layer affects the evanescent wave, thus altering the SPR angle as depicted by the increase in thickness due to a binding event. d) Reflectivity curves depicting the shift in the SPR angle due the increase in thickness from adding a 10 nm polymer layer.

glass to create an evanescent wave on the prism side of the metal layer. The surface plasmons then must transverse through the metal layer to create an evanescent wave on the dielectric side of the metal film. This limits the metal layer thickness to less than the optical penetration depth; an optimum thickness for gold and silver substrates has been shown to be between 45 and 50 nm.[46, 49] The addition of a dielectric material onto the noble metal surface distinctly alters the evanescent wave based on the optical properties of each additional layer. A layer model example is represented in Figure 1.2c with up to 3 layers added onto the noble metal layer that influence the properties of the evanescent wave.

The mathematical formulation for matching the wave vector of the photons with that of the surface plasmons starts with the Maxwell equations shown in Eq. 1 – 4,

$$\nabla \cdot \vec{H} = 0 \tag{1}$$

$$\nabla \cdot \vec{E} = 0 \tag{2}$$

$$\nabla \times \vec{E} + \frac{1}{c}\frac{\partial \vec{H}}{\partial \tau} = 0 \tag{3}$$

$$\nabla \times \vec{H} - \frac{\varepsilon}{c}\frac{\partial \vec{E}}{\partial \tau} = 0 \tag{4}$$

where $\vec{H}$ and $\vec{E}$ are the magnetic and electric field vectors, respectively, c is the speed of light in vacuum, $\varepsilon$ is the dielectric function of the material, and $\tau$ is time. The magnetic component of Maxwell's equations is ignored, as the metals used to excite SPR are non-magnetic. S-polarized light (or transverse electric modes, TE) propagates parallel to the surface, $\vec{E}_x$, which does not induce a surface charge density. The Cartesian coordinates are setup such that the z-direction is normal to the plane of the substrate. On the other hand, p-polarized light (or transverse magnetic modes, TM) has a normal component of

the electric field, $\vec{E}_z$, that creates a charge discontinuity in the z-direction. Due to the discontinuity in the electric field, the electrons in the metal layer collectively oscillate in resonance with the light wave.

The resulting plane solution to Maxwell equations for p-polarized light takes the form of Eq. 5 and 6 for medium 1 and medium 2, respectively,

$$\vec{E}_1 = \vec{E}_{1o} e^{i(\vec{k}_{x1}\vec{x} + \vec{k}_{z1}\vec{z} - \omega\tau)} \tag{5}$$

$$\vec{E}_2 = \vec{E}_{2o} e^{i(\vec{k}_{x2}\vec{x} - \vec{k}_{z2}\vec{z} - \omega\tau)} \tag{6}$$

where $\vec{k}_{xi}$ and $\vec{k}_{zi}$ are the x- and z-direction wave vectors for the i$^{th}$ layer and $\omega$ is the angular frequency. Similar equations can be written for $\vec{H}$ as those for $\vec{E}$ in Eq. 5 and 6. Continuity relations dictate that $E_{x1} = E_{x2}$ and $H_{y1} = H_{y2}$, which indicate that $k_{x1} = k_{x2} = k_x$ and reduces the general Maxwell equations to Eq. 7 and 8,

$$k_{z1} H_{y1} = \frac{\omega \varepsilon_1}{c} E_{x1} \tag{7}$$

$$k_{z2} H_{y2} = -\frac{\omega \varepsilon_2}{c} E_{x2}. \tag{8}$$

The nontrivial solution of Eq. 7 and 8 give rise to the dispersion relation, Eq. 9,

$$\frac{k_{z1}}{\varepsilon_1} = -\frac{k_{z2}}{\varepsilon_2} \tag{9}$$

which indicates that SPR only arises between materials of opposite sign dielectric constants. This sign condition is satisfied with metals such as gold and silver that have bulk dielectric functions of $\varepsilon_2 = -12.3 + 1.3i$ and $\varepsilon_2 = -14.0 + i$, respectively, and prisms with dielectric functions of $\varepsilon_1 = \varepsilon' + i\varepsilon''$, where $\varepsilon_2$ and $\varepsilon_1$ denote metal and prism, respectively. The real $\varepsilon'$ part of the prism's dielectric function depends on the type of glass used and is wavelength dependent when $\varepsilon'' = 0$. Often complex refractive index $\tilde{N}$ data is more readily available for dielectric materials, but these can be

interconverted with the dielectric function based on $\varepsilon' + i\varepsilon'' = (n + ik_o)^2$ where $\widetilde{N} = n + ik_o$, $n$ is commonly known as the refractive index, and $k_o$ is the extinction coefficient.

The wave vector matching conditions used to create surface plasmon resonance are dependent on several factors including; the wavelength and incident angle of the light as well as the optical properties of all subsequent layers.[10, 48, 49] The wave vector is composed of x- and z-direction components that give rise to Eq. 10,

$$k_{z2}^2 + k_x^2 = \left(\frac{\omega}{c}\right)^2 \varepsilon_2 \tag{10}$$

where $d$ denotes any dielectric material. Combination of Eq. 10 with Eq. 9 yields the dispersion or energy-momentum relation for surface plasmons in Eq. 11,

$$k_x = \frac{\omega}{c}\left(\frac{\varepsilon_1\varepsilon_2}{\varepsilon_1+\varepsilon_2}\right)^{1/2} \tag{11}$$

However, since $\varepsilon_m$ is complex, $k_x$ is also complex such that $k_x = k_x' + ik_x''$ which leads to Eq. 12 and 13 from Eq. 10 and 11,

$$k_{z1} \approx \frac{\omega}{c}\left(\frac{\varepsilon_1^2}{\varepsilon_1+\varepsilon_2''}\right)^{1/2} \tag{12}$$

$$k_{z2} \approx \frac{\omega}{c}\left(\frac{\varepsilon_1'^2}{\varepsilon_1+\varepsilon_2''}\right)^{1/2} \tag{13}$$

assuming that $|\varepsilon_2'| > \varepsilon_1$. With $(\varepsilon_1 + \varepsilon_2'') < 0$, the z component of the wave vector is purely imaginary and decays exponentially, $E_{zi} \propto e^{-\vec{k}_{zi}\vec{z}}$, into the i$^{\text{th}}$ medium with a decay length of $l_z = \frac{1}{k_z''}$. Similarly, a lateral decay length occurs as $l_x = \frac{1}{k_x''}$. These decay lengths give rise to the maximum distance in which the surface plasmons can propagate and interact with dielectric materials as a non-radiative evanescent wave.

In the wavelength range of interest, the dispersion relation of a free photon $k_{ph}$ in the dielectric medium (Eq. 14) is always smaller than the surface plasmon mode as shown by Eq. 15, where $k_{sp}$ is the equivalent of Eq. 11.

$$k_{ph} = \frac{\omega}{c}(\varepsilon_2)^{1/2} \tag{14}$$

$$\varepsilon_2 \leq \frac{\varepsilon_1 \varepsilon_2}{\varepsilon_1 + \varepsilon_2} \tag{15}$$

The dispersion relation for a photon in a dielectric medium $\varepsilon_d$ with a slope of $\frac{c}{\sqrt{\varepsilon_1}}$ is shown in Figure 1.3 as a black line such that $\varepsilon_1 \ll |\varepsilon_2'|$, which is the case with air as the dielectric layer. Increasing the dielectric of $\varepsilon_1$ to that of the prism $\varepsilon_p$, the wave vector shifts in slope from point 1 to 2 until the slope of the line becomes $\frac{c}{\sqrt{\varepsilon_p}}$. At a given frequency $\omega$ and incident angle $\theta$, the photon wave vector $k_{ph}$ will match that of the surface plasmons $k_{sp1}$. In Figure 1.3, the matching condition occurs at point 2 where the solid green and red lines intersect. Altering the wavelength of light from 632.8 nm to 800 nm, changes the intersection point of the photon and surface plasmon wave vectors from point 2 to 3. Increasing the dielectric from $\varepsilon_a$ to $\varepsilon_s$, where $\varepsilon_s > \varepsilon_a$, shifts the wave vector from $k_{sp1}$ to $k_{sp2}$. An example of such a shift is going from air as a dielectric to solvent. As the surface plasmon wave vector shifts, the intersection of the photon and plasmon wave vector will shift from point 3 to 4. At a constant wavelength (800 nm), the increase in dielectric will cause a shift in the incident angle at which SPR occurs from $\theta_1$ to $\theta_2$. The angular dependence of SPR is commonly resolved using Fresnel equations to describe the reflection of light from the noble metal. For a three layer system, the Fresnel equations take the form of Eq. 16,

$$R = \frac{r_1 + r_2 e^{-j2\delta_2}}{1 + r_1 r_2 e^{-j2\delta_2}} \tag{16}$$

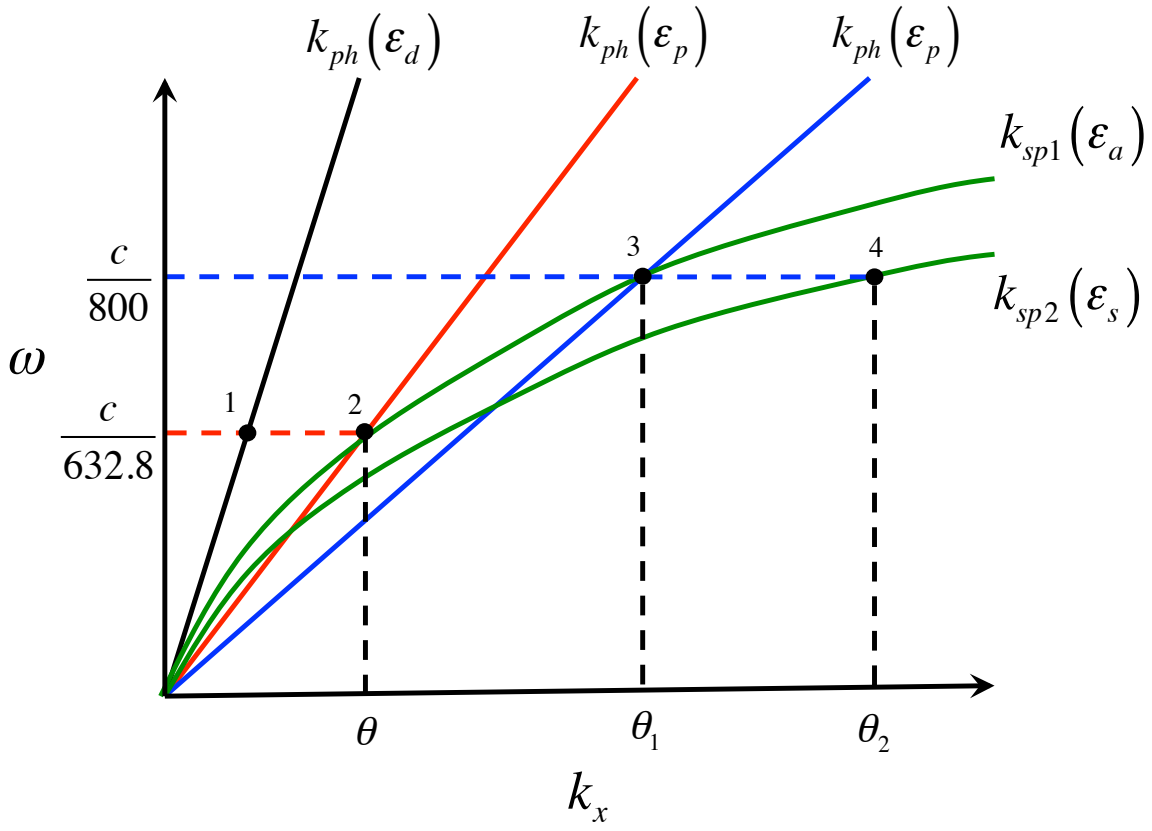


**Figure 1.3.** Dispersion relation for a p-polarized light traveling in air $\varepsilon_d$ and through a prism $\varepsilon_p$. Increasing the dielectric through which the photon travels alters the wave vector $k_{ph}$ (black line) from 1 to 2 to match the wave vector of the surface plasmons $k_{sp1}$ (green line). The wave vector matching conditions are wavelength dependent as depicted by where light at 632.8 nm (red dashed line) and 800 nm (blue dashed line) intersects $k_{sp1}$ at points 2 and 3, respectively. The surface plasmon wave vector shifts from $k_{sp1}$ to $k_{sp2}$ as the dielectric in contact with the interfaces increases from $\varepsilon_a$ to $\varepsilon_s$. With a constant wavelength at 800 nm, the angle at which plasmons are observed shifts from $\theta_1$ to $\theta_2$ as the wave vector goes from 3 to 4.

$$\delta_2 = \frac{2\pi\omega}{c} t_2 \widetilde{N}_2 cos(\phi_2) \quad (17)$$

where $R$ is the total reflection, $r_i$ is the reflection from the i[th] layer, and $\delta_2$ is given by Eq. 17 for a metal layer with finite thickness $t_2$ which shows the thickness dependence of the SPR. Angular dependence arises from the refraction angle $\phi_2$ based on Snell's Law, $\widetilde{N}_2 cos(\phi_2) = \widetilde{N}_1 cos(\phi_1)$, where $\phi_1$ is the incident angle in the prism.

In Figure 1.2d, the wavelength of light is held constant at 632.8 nm and the angle of incidence is adjusted to measure the reflectivity response. As the angle of incidence is increased from 30° to 60° the first distinct point on the reflectivity curve is the sharp increase around 40° which is the angle where total internal reflection (TIR) first occurs for a BK7 prism (n = 1.5151 at λ = 632.8 nm). Without a noble metal layer the TIR would maintain the same level of reflectivity for all higher angles, however, in the presence of the metal layer surface plasmons will start to form as indicated by the dip in the reflectivity curve.[46] The creation of SPR occurs with the absorbance of photons, which would be measured by a decrease in reflectivity. Using the ideal thickness of noble metal, the plasmon dip would have a reflectivity near 0 as all photons are absorbed as SPR. The plasmon dip in Figure 1.2d depicts a measurement using a 45 nm Au film (black curve). As a dielectric layer is added the angle of the surface plasmon dip will shift to higher incidence angles, Figure 1.2d (red curve), which was created by attaching a 10 nm polymer film (n = 1.5 at λ = 632.8 nm) to the gold.

The choice of noble metal plays an important role in determining the shape of the plasmon curve as well as in sensing applications.[46] Gold is found in a variety of SPR sensors as it is a stable metal with known affinities for thiols.[10, 23, 25, 46, 53] Alternatively, silver can also be used to create SPR and produces a plasmon dip that is much sharper

than gold, however, silver is prone to oxidation and will tarnish over time. Figure 1.4 demonstrates the contrast in the SPR properties of 47 nm of silver (black) and gold (red) on SF11 glass in ethanol. The dashed line indicates modeling of the optical properties in Winspall[54, 55] using the Fresnel equations for reflectivity. The silver plasmon dip is much narrower than the broader gold curve; which leads to increased sensitivity in reflectivity tracking applications when using a silver substrate.

While the TIR and SPR points are the most distinct on the curve the presence of the other layers in Figure 1.2c will also affect portions of the plasmon curve. The layer between the noble metal and glass is a thin metal layer of chromium or titanium added as an adhesion layer. The presence of the adhesion layer does not directly alter the plasmon dip angle, consequently, as the adhesion layer is increased in thickness the plasmon excitation will become less efficient resulting in a smaller change in reflectivity between the total internal reflection point and plasmon minimum. To maintain optimum plasmon conditions the adhesion layer is kept to 2 to 3 nm, which is also sufficient to prevent delamination of the noble metal. The addition of any layer on top of the noble metal will cause a similar shift to the SPR dip as that shown in Figure 1.2d. Depending on the desired surface chemistry the presence of the $4^{th}$ layer, denoted by $n_4$ and $t_4$, can be varied to allow for a broader range of surface functionalization. When attaching monolayers using a thiol group the $4^{th}$ layer is not present as gold and silver readily bond with thiols.[22, 23, 53] Depositing a thin oxide layer (~10 nm) on top of the noble metal allows for other chemistries to be performed on SPR substrates, such as the attachment of silanes. In order to track changes in the organic layer ($5^{th}$ layer) all the other layers must be fully characterized prior to monitoring any changes in the layer of interest. Therefore, as the

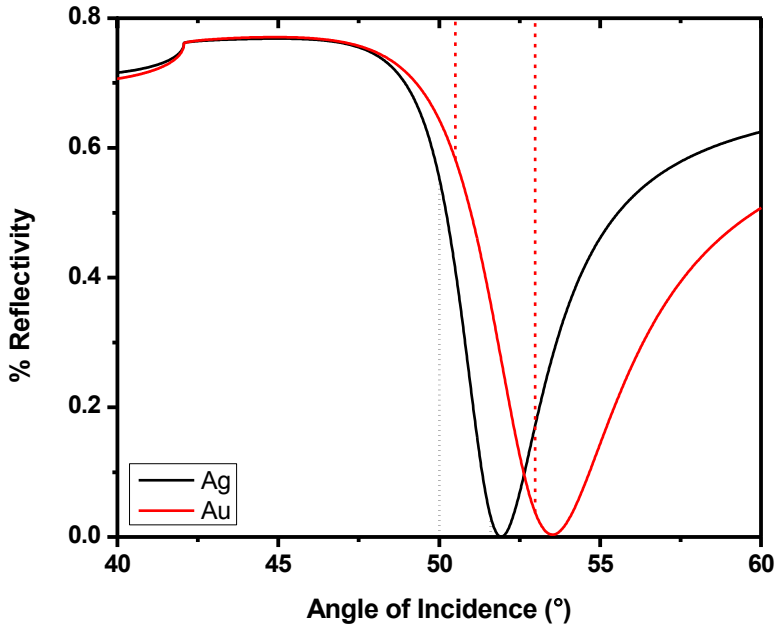


**Figure 1.4.** Reflectivity curves from SPR substrates relative to the incident angle at a fixed wavelength (λ = 632.8 nm) for Au (red) and Ag (black) films on SF11 glass (n = 1.7786 at λ = 632.8 nm) with a 2 nm adhesion layer. The 47 nm films have plasmon minimums at 53.5° and 51.9°, respectively. Data framed by the dashed lines represent the linear region used in kinetic tracking. The regions span 1.6° and 2.5° for Ag and Au, respectively.

SPR substrates are created using various deposition techniques (e-beam, thermal evaporation, plasma sputtering, etc.), they are analyzed to determine the optical properties of each of the layers.

The last layer in Figure 1.2c, indicates the presence of a solvent layer, with a refractive index of $n_6$. For *ex situ* measurements, like those in Figure 1.2d, the solvent layer is air ($n_6 = 1$).[46] However, for *in situ* measurements the refractive index of the

solvent layer is greater than one, which causes the plasmon dip and TIR angles to shift to higher angles of incidence, Figure 1.5. The data was modeled using a 47 nm Ag coated SF11 glass (n = 1.7786 at λ = 632.8 nm) substrate. The refractive index of the solvent layer $n_6$ was increased from n = 1.3614 (black) to n = 1.3772 (red) by changing the solvent layer from ethanol to isopropanol, respectively. The ability to predict how the plasmon will shift in solvent is important when monitoring reaction *in situ*, especially when transitioning from one solvent to another for different reactions and to distinguish between the shift in the plasmon dip due to refractive index changes from those of thickness.

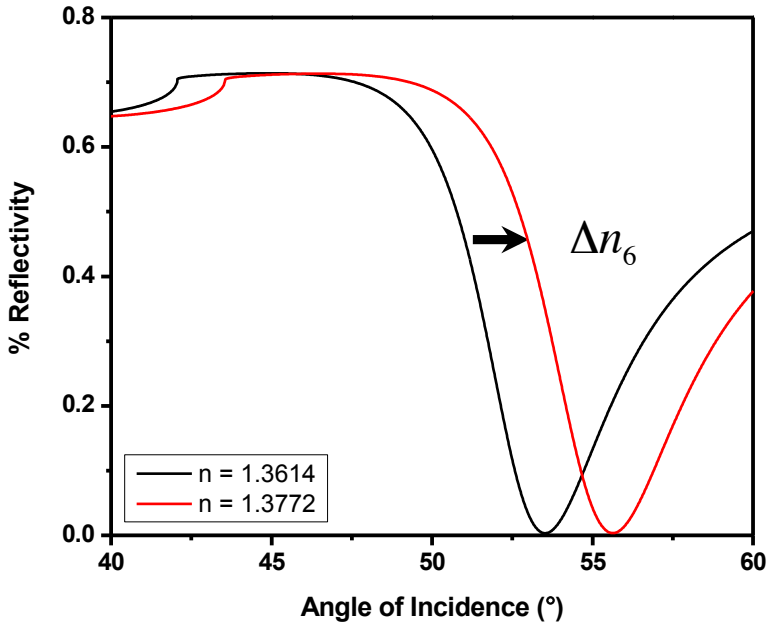


**Figure 1.5.** SPR curve shift due to changes in the refractive index of the solvent layer, $n_6$, from ethanol (n = 1.3614, black) to isopropanol (n = 1.3772, red). This refractive index increase induces an increase in the plasmon dip angle as well as in the TIR angle. Data is modeled using a 47 nm Ag coated SF11 glass (n = 1.7786 at λ = 632.8 nm) substrate.

Monitoring the changes in the organic film, layer 5 from Figure 1.2c, can be accomplished *ex situ* by scanning versus all incident angles at various time intervals. While the *ex situ* method can be modeled to accurately determine the thickness and refractive index of the organic film it does not provide real time analysis of a reaction. In order to measure a reaction as it occurs with SPR different technique needs to be applied known as reflectivity tracking.[10, 46, 48, 49] This method utilizes a linear portion of the SPR curve to directly correlate the change in reflectivity to the shift in the plasmon dip angle, which was previously established to be dependent on the optical properties of the film. A linear portion of the curve is used as it provides a direct relationship between reflectivity and thickness increase. Non-linear portions of the curve cannot be directly correlated and result in erroneous kinetic information.

Kinetic reflectivity tracking uses a fixed wavelength, fixed angle method to monitor reactions *in situ*.[10, 46, 48, 49] The angle of incidence chosen for reflectivity tracking is dependent on the starting SPR substrate layer and the direction of the plasmon will shift. As there are two linear portions of the SPR curve the angle of incidence for reflectivity tracking can be monitored from the right or left of the plasmon dip. In most applications reflectivity tracking is used to track the increase in thickness, which results in a shift in the plasmon to the right. A simulated example of kinetic data is shown in Figure 1.6a using a 47 nm Au coated SF11 substrate with ethanol as the solvent layer. Monitoring the thickness increase in Figure 1.6a by reflectivity tracking requires the angle of incidence to be set at 52.7° as shown on black curve by the red circle. As the polymer layer is increased in thickness from 0 nm to 16 nm in 2 nm increments at a constant refractive index of 1.5, the plasmon shifts to the right at equivalent intervals as

denoted by Δt. Alternatively, the reflectivity at the tracking angle increases as the thickness is increased as denoted by the Δ%R.

The increase in reflectivity from Figure 1.6a, can be measured relative to time to produce a reflectivity tracking curve as shown in Figure 1.6b. As the data is simulated the time intervals are arbitrary. The initial flat part of the reflectivity curve represents the formation of a stable baseline from which any noise fluctuations in the measurement can be determined. As the reaction proceeds, the reflectivity will increase over time. If the reaction is complete within the linear portion of the curve, the reflectivity increase will plateau. However, a second form of plateau can also occur which does not represent the completion of the reaction. This effect occurs when the plasmon shift, at the set angle of incidence, causes the reflectivity tracking to measure outside the linear portion of the curve. In Figure 1.6, this transition starts to occur around the 16 nm thickness. As the plasmon continues to shift the reflectivity tracking will measure the non-linear portion at the top of the plasmon curve just after the onset of TIR. A post-reaction angular scan will determine if the plateau is due to the completion of the reaction or from going beyond the linear portion of the SPR curve.

Despite being limited to the linear portion of the curve, there are many techniques available to improve either sensitivity in reflectivity tracking or the maximum plasmon shift. As previously discussed the use of silver can increase the sensitivity of a reflectivity tracking measurement. With a narrower plasmon dip the linear portion of the curve has a larger slope than that of Au. In Figure 1.6, the slope (d%R/dθ) of the linear portion of the curve is -0.236 for the Au film while a Ag film has a slope of -0.352 (Figure 1.4) as computed in Winspall using a 47 nm metal layer on SF11 glass in ethanol.

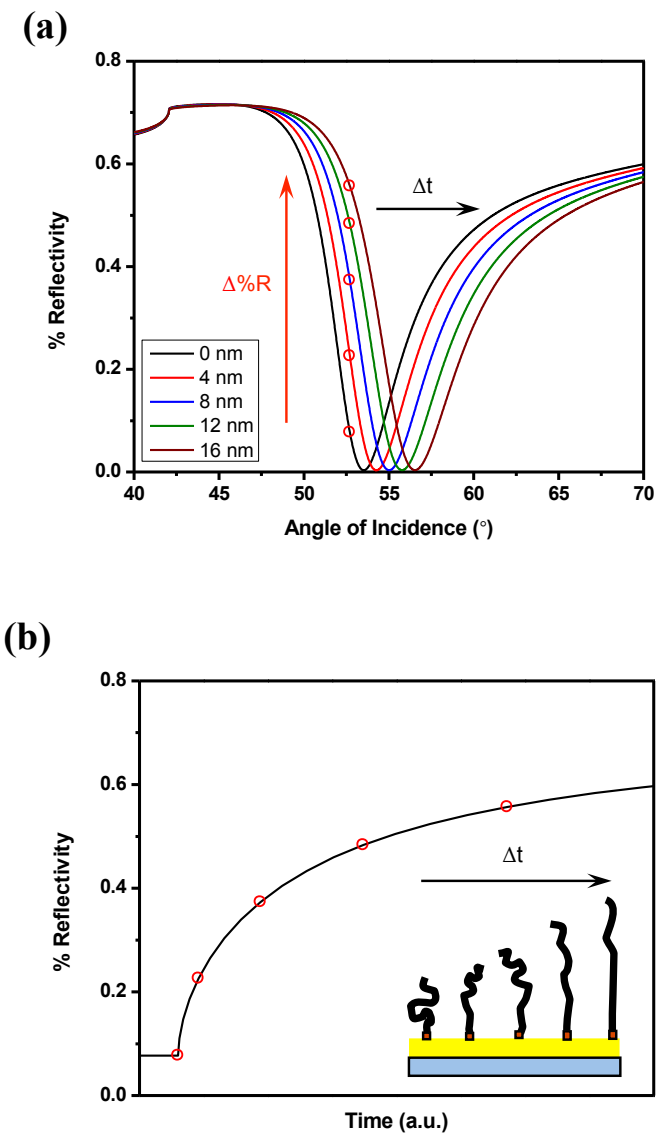


**Figure 1.6.** Simulated SPR reflectivity tracking of due to the increase in thickness of an organic layer. a) Data modeled from an SF11 glass (n = 1.7786) substrate with 2 nm of Cr and 47 nm of Au with an organic dielectric layer (n = 1.5) of varying thickness in ethanol (n = 1.3614). Refractive indices are reported at λ = 632.8 nm. b) Monitoring the increase in reflectivity (Δ%R) over time at a specified incident angle, 52.7° (red circles), can then be directly correlated to the increase in thickness (Δt) of the polymer brush (inset).

With a larger slope the change in reflectivity will be greater for every equivalent shift in the plasmon dip thus increasing sensitivity. Adversely, due to the smaller slope, gold can be used to scan across larger shifts in the plasmon dip position. As shown in Figure 1.4, the Ag film has a linear curve between the TIR and the reflectivity dip that is 1.6° wide, while Au has a 2.5° range that is useful as a direct correlation between reflectivity and angular shift. By adjusting the metal layer, the sensitivity and the angular scanning range of SPR can be tuned.

SPR has thus far been limited to measuring a single plasmon excitation point. In order to achieve the high throughput analysis desired for kinetic tracking a large area of the substrate needs to be scanned simultaneously. SPR Imaging (SPRI) accomplishes this using a wide light beam and a CCD camera to collect the light relative to the area.[2, 10, 47, 48, 56] In order to achieve the large scanning areas, white light is passed through a band-pass filter to select the wavelength at 800 nm. While this deviates from 632.8 nm used to create the diagrams previously mentioned, the change in the wavelength only slightly alters the plasmonic properties of the substrate, Figure 1.7. The red solid line was modeled using a 47 nm Au film with an equilateral SF11 prism with ethanol as the solvent layer at $\lambda$ = 632.8 nm. At this wavelength, the plasmon dip goes to zero reflectivity at 53.5°. However, when the wavelength is increased to 800 nm (black, solid curve) the minimum of the plasmon curve is non-zero at 53.8°. The increase in reflectivity indicates a decrease in the efficiency of the plasmon generation at higher wavelengths. Increasing the thickness of the film to 57 nm (black, dashed curve) improves the plasmon depth with a minimum at 53.4°. However, this is not necessary as SPRI is used as a reflectivity tracking instrument where only the relative change in

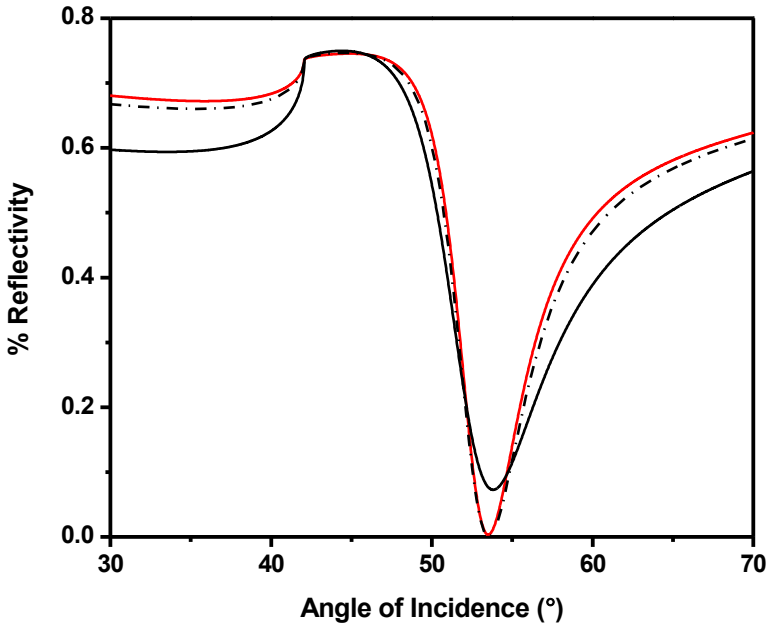


**Figure 1.7.** Comparison of SPR responses at 632.8 nm (red) and 800 nm (black) wavelengths. A 47 nm Au layer is the optimized thickness for the measurements at λ = 632.8 nm (red). With a 800 nm light the plasmon minimum is non-zero (black, solid) for a 47 nm Au film. Increasing the Au thickness to 57 nm produces the optimum SPR conditions at λ = 800 nm. Data is modeled using Au coated SF11 glass (n = 1.7786 at λ = 632.8 nm) substrate.

reflectivity (Δ%R) are important. Since the SPRI is limited to reflectivity tracking the characterization of each layer is performed using the 632.8 nm light source. Such a distinction is crucial only when comparing the amount of reflectivity taken over a given time interval between the two wavelengths.

Data taken with an SPR Imager is recorded as pixel values where the intensity of the pixel is directly related to the amount of reflected light.[10, 47, 57, 58] Figure 1.8a is an

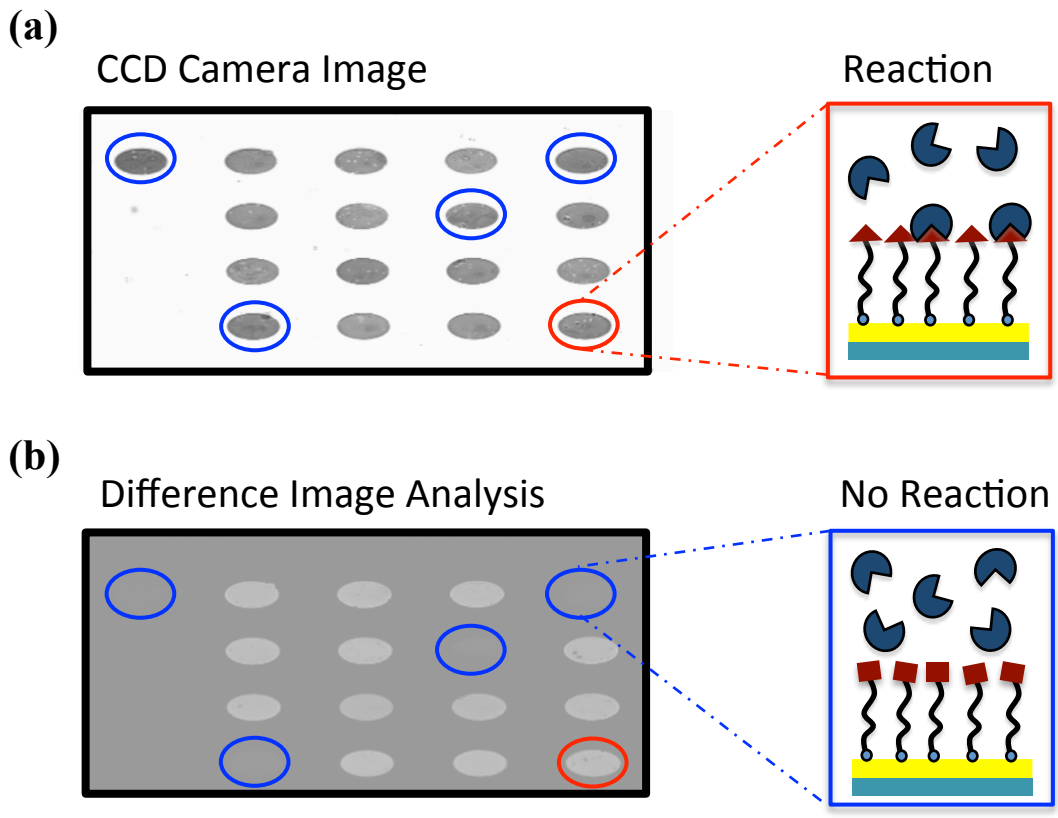


**Figure 1.8.** SPR imaging uses a CCD camera as a detector where each pixel value is directly related to the reflectivity curve. a) Pixel values on the image are dark when the incident angle matches the plasmon dip. b) Reflectivity tracking is performed using difference image analysis, where the first image is used as a reference and is subtracted from all subsequent images in order to monitor the change in reflectivity (Δ%R). Images depict an array for parallel analysis where the reaction (red) of streptavidin binding to a surface bound biotin monolayer occurs on some spots while a passivated layer (blue) is used to determine non-specific binding.

SPR image taken using an array of 47 nm gold dots that were functionalized with a biotylated monolayer.[59, 60] The angle of incidence is adjusted to the substrates tracking angle, analogous to the red circles in Figure 1.8a, in order to match the plasmon dip angle for the gold dots. In this setup, the plasmon dip is observed by the absence of a reflection, the darker areas on the image indicate a decrease in the reflected light. The pixels in each dot can be analyzed to determine the amount of reflected light that is present. Analyzing the same pixels in subsequent images yields the time dependent data for which the SPR imager was designed. Kinetic data from the SPR imager is referenced to the initial images taken prior to a reaction, much like the positions in Figure 1.8b. This referencing, known as difference image analysis, is done to all images from a given experiment to produce the Δ%R data attributed to a reaction. A difference image is shown in Figure 1.8b, where the image was taken at the end of a reaction of the biotintylated monolayers with streptavidin, red zoomed diagram. As the reaction proceeds the plasmon dip angle shifts away from the starting angle causing an increase in reflectivity which results in the spots getting lighter over time.

Due to the visual change in the images, the SPR imager can provide both quantitative data from a binding event as well as a direct analysis indicator of a reaction. With the large surface area for measuring SPR, the imager can be incorporated with various patterning methods to create separate and discrete surface functionalization reactions used for simultaneous analysis across the whole surface.[47, 56, 61-63] In Figure 1.8, two different monolayers are used to compare the gold array created by selective deposition through a patterned mask. In these images the spots with the blue circles are passivated with an oligoethyleneglycol monolayer with a terminal thiol group to which

streptavidin will not bind, Figure 1.8b, zoomed diagram. These spots act as a referencing method to determine the amount of non-specific binding that occurs between the interaction of streptavidin and an organic layer.[10, 52, 64, 65] Non-specific binding is not limited to passivated surfaces but can also occur on the biotin functionalized spots. By comparing these two surfaces the amount of non-specific binding can be removed from the kinetic data taken from the remaining functionalized surfaces. This ensures that any observed reaction rates are of the actual reactions taking place on the surface rather than the formation of physisorbed material.

**Grating Coupled SPR**

Prism coupling is not the only method that can be used to excite surface plasmon resonance. Diffraction gratings can also couple polarized light to the surface as surface plasmons.[46, 49, 66, 67] This method to creating SPR has been known for sometime as the Wood's anomly where the plasmon modes were created when metallic gratings were used in spectrophotometers as a dispersive element.[46, 49] Just as the prism is used to provide the extra momemtum in the Kretschmann configuration, the diffraction grating can couple photons to the surface using the dispersion curve that is dependent on the grating periodicity. Grating SPR sensors therefore have up to four parameters that can be tuned to produce the desired SPR response: periodicity, wavelength, incident angle, and dielectric functions.[46, 49, 68, 69] The interdependence of these parameters is auspiciously depicted through Eq. 18;

$$sin(\theta_m) + m\frac{\lambda}{\Lambda} = \pm Re\left\{\sqrt{\frac{\varepsilon_a n_d^2}{\varepsilon_a + n_d^2}}\right\} \quad (18)$$

where the incident angle where the plasmon dip forms is given by $\theta_m$ and can be predicted for a given grating period $\Lambda$ and wavelength $\lambda$. As the equation shows, the

excitation of SPR retains its dependence on the dielectric function of the metal $\varepsilon_a$ as well as the refractive index $n_d$ of the medium in contact with the surface. Consequently, the excitation of the SPR is also dependent on the diffraction order $m$ produced by the grating. The effects of each of these criteria for diffraction coupled SPR have been reported in the literature[46, 67, 70, 71] but are reviewed here in order to elucidate how grating structures can be used as a SPR chemical sensors.

Despite the advantages of grating coupled SPR, diffraction gratings have not been widely implemented for SPR due to limitations in fabricating the subwavelength to wavelength-sized features needed to create the necessary diffractions. Several lithiographic techniques have been used to create diffraction structures for SPR sensing.[72-75] However, these methods are tedious to accurately reproduce the grating structures or require deep UV techniques or projection optics to create grating structures of the appropriate size and spacing.[34, 72, 75] While the periodicity of these structures is important, the size of repeated features has also been shown to affect the plasmonic properties of the grating substrates.[76] Such dependence in the feature size and periodicity aspect ratios can lead to a variety of possibilities for the grating structure without an uniform method to directly compare between experimental conditions. In order to circumvent this problem, recent research has used a commercially available grating structure found in optical discs, such as CDs, DVDs, and blu-ray discs (BDs).[70, 76, 77]

Optical storage media utilize a grating structure to guide the reading and writing of information either into a metal layer or an organic dye.[76] By decreasing the grating periodicity and adjusting the wavelength of light, digital media has been stored on grating structures with 1600 nm, 740 nm, and 320 nm pitches on CDs, DVDs, and BDs,

respectively. The optical disc drive of a computer reads the data stored on these discs by scanning along the continuous grating track and a detector reads the reflection off the metallic backing layer. This setup maintains the optical components of the scanner in a position that is nearly perpendicular to the substrate. By adjusting the optics to shine light perpendicular to the grating structure (Figure 1.9a) a series of diffraction orders can be produced.[46, 49, 71] If the metal used as the backing layer was silver or gold, this setup would produce surface plasmons at the various diffraction orders. While some discs can be purchased with noble metal reflective layers, the thickness of the layer is either too thin to be used in reflectively measured SPR applications or too thick for transmission mode SPR excitation.[46, 71, 76, 77] The applications presented herein utilize the reflection mode configuration, depicted in Figure 1.9a, for grating measurements and thus required the deposition of an optically thick (> 100 nm) noble metal coating.

The diffraction modes created when p-polarized light is shown onto the noble metal coated grating are represented in Figure 1.9a, as the pink arrows. As the angle of incidence, θ, is increased from 0° the reflected light will match the diffraction angle where surface plasmons are formed. The evanescent field formed when the plasmons are created is sensitive to the presence of any dielectric layer on the surface of the noble metal.[49, 51] The layer model for a grating surface is presented in Figure 1.9b and is similar to that used with in Figure 1.2. With the grating structure, light passes through each layer before exciting surface plasmon resonance at the metal interface. Layer numbering for the grating setup is inverted from the prism setup when using a numbering scheme where the first layer is the film initially encountered by the incident light. While most of the data presented here is for reflective measurements, the refractive index and

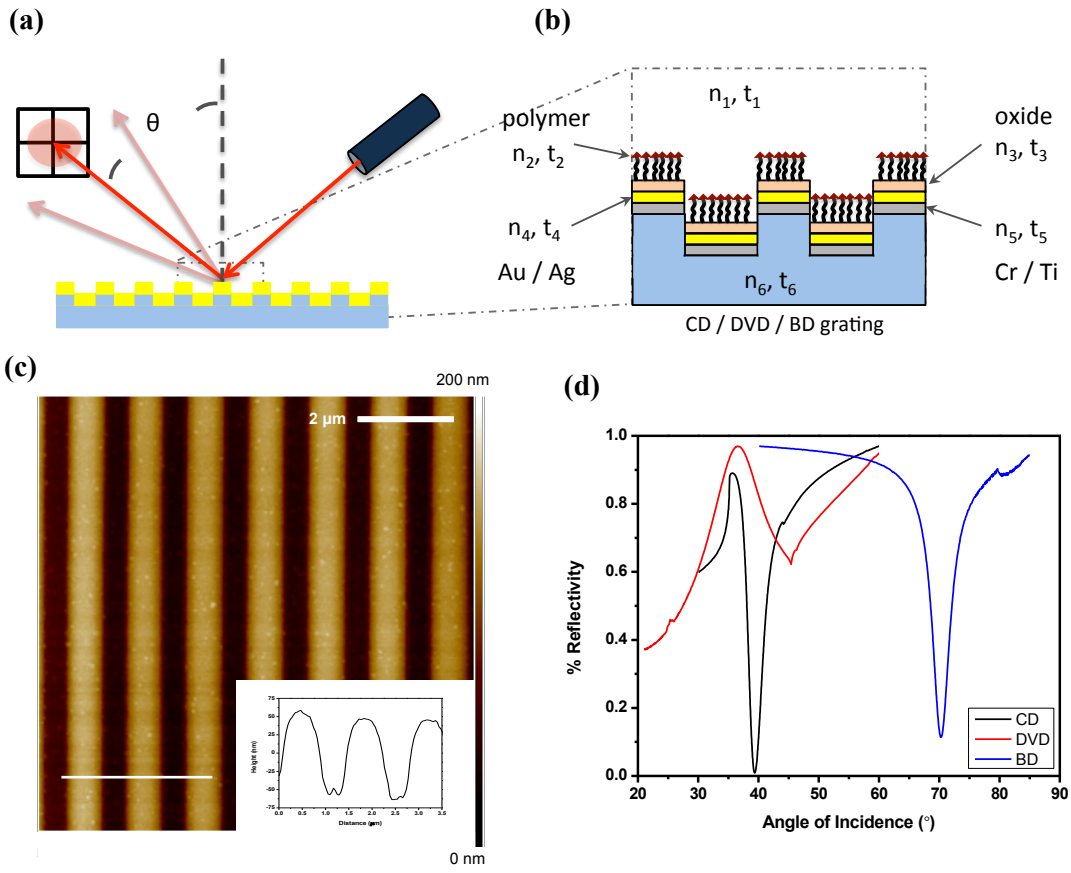


**Figure 1.9.** Diffraction coupled surface plasmon resonance using optical discs (CDs, DVDs, and blu-rays) as a source for consistent gratings. a) Polarized light is coupled to the noble metal coated grating surface at the various diffraction orders indicated by the multiple reflected arrow and are measured by a detector. b) Block layer model for grating sensors, which includes the adhesion layer, an optically thick noble metal layer, and oxide layers for adjusting binding chemistries for the polymer layer. c) AFM image of a CD grating structure with a Au film. Inset depicts the line profile taken along the white line. d) SPR curves from a CD, DVD, and BD with a 100 nm thick Ag layer using p-polarized light with an incident plane parallel to the grating direction. Each disc exhibits different SPR qualities due to the various grating periodicities; 1600 nm, 740 nm, and 320 nm, respectively.

thickness of the polycarbonate layer will affect transmission measurements.[77] An adhesion layer is present to ensure that the noble metal layer does not delaminate. The surface chemistry can be altered with the addition of an oxide layer for growing or attaching polymer thin films. Each layer has to be optically transparent due to the necessity of light passing through each layer, the thickness of each film must to be less than the penetration depth of the respective material.[49, 51]

The established layer model in Figure 1.9b, illustrates the grating structure as series of repeating blocks. While precise lithographic techniques have been shown to produce such features, the periodic grating structure for the optical discs is more sinusoidal than square.[76] A 50 nm Au coated CD's grating structure is depicted in Figure 1.9c with an atomic force microscopy (AFM) image. The inset plot contains the height profile data taken from the AFM image along the white line in the bottom left corner. A peak to trough distance for the CD was determined to be ~120 nm across the entire AFM image, which is dissimilar to 150 nm reported in the literature. While some of the difference can be attributed to the Au film deposition, the net variance could be from the different CD manufacturers. This was confirmed with a height profile measurement of a different manufacturer, which gave a height profile of ~140 nm.

Despite the variance in the height, the plasmonic properties of the CD grating coincide with those previously reported in the literature.[76] An angular scan of 100 nm Au coated CD, DVD, and BD substrates are given in Figure 1.9d. With the 632.8 nm light source, the CD produces a plasmon dip at 39° created by the m = +1 diffraction order. Alternatively, the m = -1 diffraction order can be seen when using the smaller pitched BD with a plasmon dip at 70°. The sign of the plasmon dip can be determined from the

equation previously discussed as well as from the presence of the sharp increase in reflectivity at 35° and 87° for the CD and BD. The order of the plasmon dip will also dictate the direction the plasmon curve will shift when a dielectric layer is added.[69] Upon adding a monolayer to the CD or BD, the plasmons shift to the higher and lower angles of incidence. Contrary to the CD and BD, the DVD produced an increase in reflectivity with maximum around 37°. Enhanced optical properties have been observed when measuring DVDs in transmission mode[78], however, the mechanism for the increase in reflectivity is beyond the scope of this document and DVD will be excluded from this point forward.

The angular measurement method of producing diffraction coupled SPR is less common than measuring relative to wavelength and is attributed to the dependence on the wavelength-periodicity ratio found in Eq. 1.[46, 48, 76, 79] The black curves in Figure 1.10 a) and b) represent the angular dependence of a 100 nm Au coated CD and BD substrates at an incident angle of 70° and incident plane parallel with the direction of the grating pitch. The CD exhibits two distinct plasmon dips at 740 and 970 nm, which correspond to a positive and negative diffraction order. Each plasmon shifts with the addition of a polymer resulting in the plasmon diffraction orders occurring at increasing and decreasing wavelength. With convergent plasmon dips, monitoring a reaction over time can prove to be difficult. Alternatively, the BD disc produces a single sharp plasmon dip making it easier to track as it shifts with a reaction. The advantages of the BD disc as a chemical sensor are further explored in Chapter 4.

A unique feature of the grating coupled SPR substrate occurs when the incidence plane of light is non-parallel to the grating's pitch direction.[46] If the discs are rotated

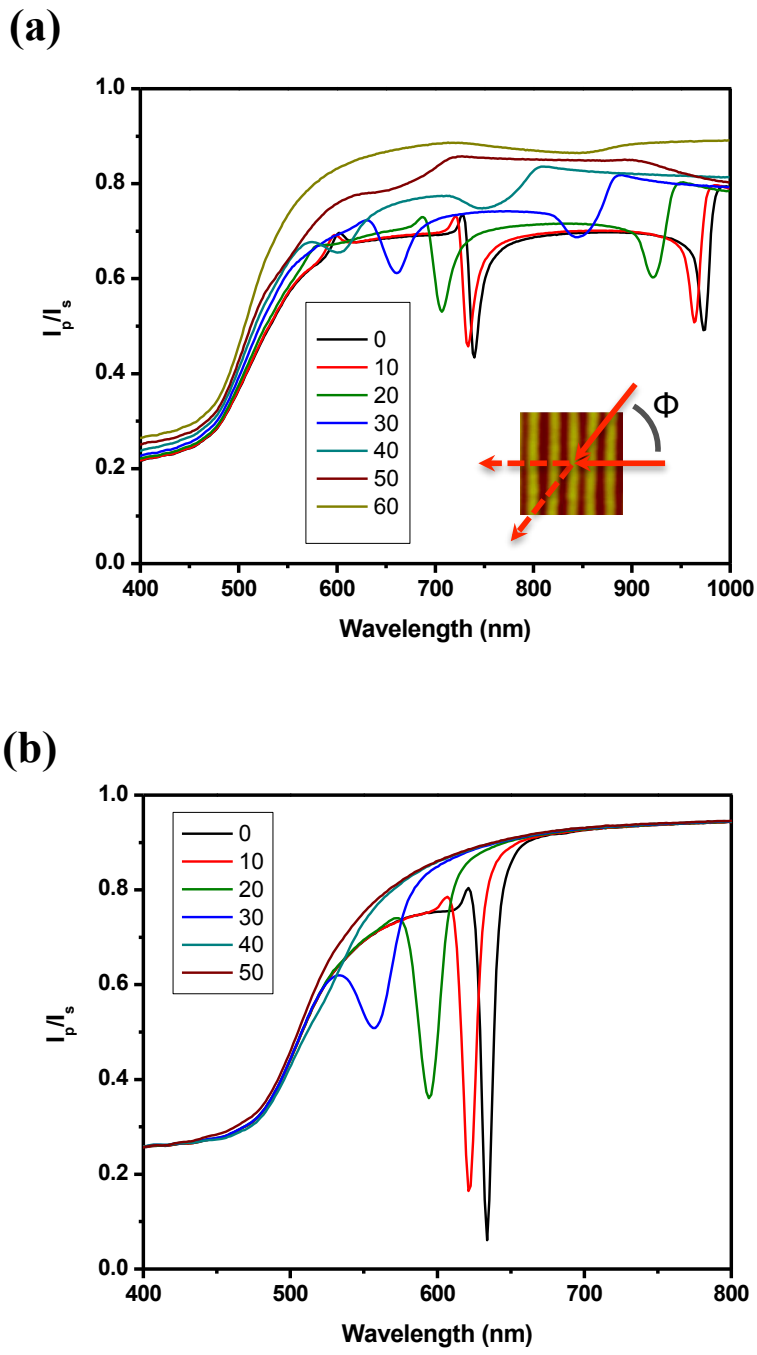


**Figure 1.10.** Wavelength and planar rotation effects on diffraction coupled SPR using a) a CD and b) a BD with 1600 nm and 320 nm grating periodicities, respectively. The inset in a) depicts the rotation of the incident plane relative to the grating structure Φ. Data was taken at 10° rotational intervals with at a 70° angle of incidence.

about the substrate normal, all plasmons will shift to lower angles of incidence, Figure 1.10. The angle formed between the incident plane of light and pitch direction of the grating is increased by 10° to produce the left plasmon shifts for the CD in a) and BD in b). As the plane is altered the wave vector matching conditions are adjusted namely through adjusting the periodicity the p-polarized light encounters. Similar uniform shift can be observed with angular scans, however, in this case plasmon dip will shift to higher angles of incidence.[46] While this feature of grating SPR has been previously reported, it is important to note here as this will affect the alignment of the gratings, which can result in false positives when used in chemical sensors.

**Ellipsometry**

Ellipsometry is another powerful, label-free sensing technique that is used in determining optical properties as well as monitoring changes in thin films.[80-83] While the setup for ellipsometry, Figure 1.11a, is similar to grating coupled SPR there are a several distinct differences. Where SPR measures interfacial properties using p-polarized light, ellipsometry uses both p- and s-polarized light to determine the thickness and refractive index of films. Polarized light a light source is passed through a quarter wave plate at non-axial polarization angles, by inducing a phase lag onto the s-component of the polarized light, elliptically polarized is created.[84, 85] As with measuring the grating substrates, the light passes through each layer before reflecting off of a bulk reflective surface, therefore requiring all upper layers to be transparent. When the light passes through the organic layer, denoted with $N_2$ and $t_2$, the elliptically polarized light is altered resulting in intensity and phase changes as denoted by Eq. 19,

$$\rho = \frac{R_p}{R_s} = tan(\psi)e^{i\Delta} \quad (19)$$

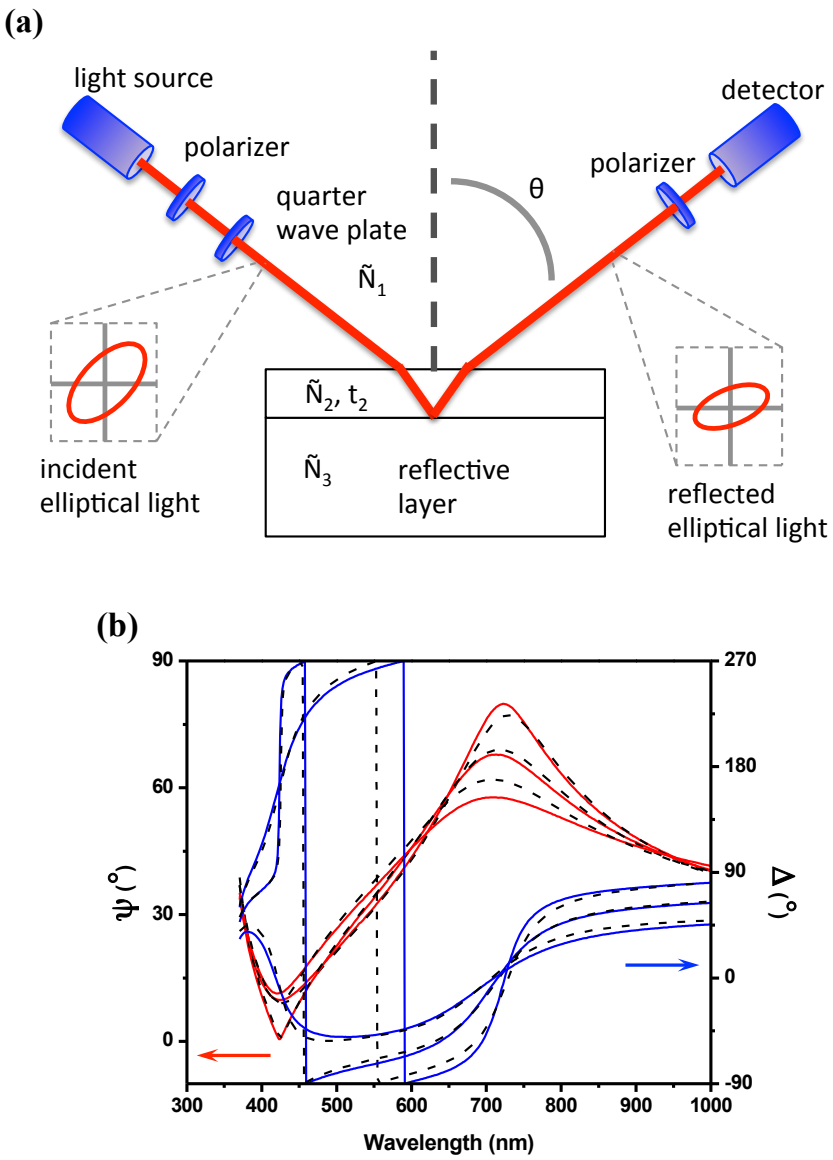


**Figure 1.11.** An exemplar setup for both null and spectroscopic ellipsometry. a) Incident light is elliptically polarized using a quarter wave plate. As the light interacts with the film and is reflected off the underlying surface, the magnitude and phase of the light will alter based on the optical properties of the film. b) Reflected data is recorded as $\psi$ and $\Delta$ which are related to the intensity ratio of p- and s-polarizied light and the phase change of the light, respectively. Data is modeled (dashed lines) to determine the thickness and complex refractive index of the layer.

where $\rho$ is the reflectivity ratio of p-polarized light to the s-polarized and is measured by the amplitude $tan(\psi)$ and phase shift $\Delta$ of the ellipse.[84] Ellipsomtry data is recorded and displayed in terms of $\psi$ and $\Delta$ rather than reflectivity ratios, a key difference from SPR. The measured values for amplitude and phase shift are modeled by applying Fresnel equations in order to determine properties like thickness and refractive index. As with SPR, in order to determine the optical properties of the polymer layer all other layers must be accurately characterized, therefore simplifying the Fresnel model to manageable fitting algorithms.

The wavelength and incident angle dependence of $\psi$ and $\Delta$ are not directly present in Eq. 19, however, the dependence arises within the parameters by the implementation of the Fresnel equations.[84, 85] Refractive index $\tilde{N}$ is wavelength dependent and the reflectivity ratio is angular dependent. A similarity of the angular dependence can be drawn with the Brewster angle where p-polarized light exhibits a minimum for most materials.[86] These dependencies should be considered when measuring with ellipsometry either at fixed wavelength and angle or spectroscopically. With fixed wavelength and angle, the thickness or refractive index of a material can be accurately determined, however, it is difficult to determine both parameters simultaneously.[85] In order to deconvolute the refractive index of a layer from the thickness, $\psi$ and $\Delta$ are measured spectroscopically allowing the wavelength dependence of the refractive index to be utilized in data modeling. An example set of spectroscopic ellipsometry data is shown in Figure 1.11b with a 120 nm polymer film on a silicon wafer with native oxide. $\psi$ and $\Delta$ values are measured at each wavelength and are plotted as red and blue curves. The spectroscopic measurement is repeated at three angles of incident taken around the

Brewster angle to improve the computation of the refractive index and thickness.[85] The Fresnel approximations for $\psi$ and $\Delta$ (black dashed line) are fit to the recorded data through a layer model applied by specialized spectroscopic ellipsometer software. Using empirical models for the complex refractive index, the fit will return the predicted thickness and optical properties of the thin film.

For the three-layer model in Figure 1.11a, the Fresnel equations take on the form of Eq. 20 and 21,

$$R_p = \frac{r_{12}^p + r_{23}^p e^{-j2\beta}}{1 + r_{12}^p r_{23}^p e^{-j2\beta}} \tag{20}$$

$$R_s = \frac{r_{12}^s + r_{23}^s e^{-j2\beta}}{1 + r_{12}^s r_{23}^s e^{-j2\beta}} \tag{21}$$

where $R_p$ and $R_s$ is the net reflectivity while $r$ represents Fresnel coefficients at each interface denoted by the layer numbers 1, 2, and 3 for the $p$ and $s$ polarization. In Eq. 20 and 21, $\beta$ is denoted by Eq. 22,

$$\beta = 2\pi \left(\frac{t}{\lambda}\right) \tilde{N}_2 cos(\phi_2) \tag{22}$$

where $\lambda$ is the wavelength of light $\tilde{N}_2$ and $\phi_2$ are the complex refractive index and refraction angle of layer 2, respectively, and t is the thickness of the layer. The Fresnel coefficients relate the reflection at each interface the light to light refracted as it passes from one medium to the next. For the first interface, the Fresnel coefficients incorporate the complex refractive index of each layer $\tilde{N}_1$ and $\tilde{N}_2$ as well as the angle of refraction $\phi_1$ and $\phi_2$ as denoted by Eq. 23,

$$r_{12}^{p,s} = \frac{\tilde{N}_2 cos(\phi_1) - \tilde{N}_1 cos(\phi_2)}{\tilde{N}_2 cos(\phi_1) + \tilde{N}_1 cos(\phi_2)} \tag{23}$$

which takes the same form for $p$ and $s$ polarization of light. A vital distinction arises amongst Eq. 20-23 that is important for separating the convoluted thin film refractive

index and thickness using reflection measurements. In Eq. 19, the exponential term is only associated to changes in Δ. Similarly, in the Fresnel equations an exponential term $\beta$ is dependent on the refractive index and thickness of the second layer. However, the Fresnel coefficients do not contain a dependence on thickness signifying that $tan(\psi)$ is only dependent on the refractive index of the film and not thickness. With $\psi$ independent of thickness the modeling in Figure 1.11b can be done interactively by approximating the refractive index of the film with $\psi$ and then determining the thickness with Δ until a good fit is achieved.

The optical properties of polymer thin films are determined by modeling the real and imaginary parts of the complex refractive index $\tilde{N}$ separately, where $\tilde{N} = n + jk$. These terms are referred to as the refractive index, $n$, and extinction coefficient, $k$. A Cauchy model, Eq. 24, is used to fit the refractive index, $n$,[81, 87] while the Urbach equation, Eq. 25, is used to determine the extinction coefficient, $k$,[88]

$$n = A + \frac{B}{\lambda^2} + \frac{C}{\lambda^4} \tag{24}$$

$$k = k_o e^{D(E-B')} \tag{25}$$

where A, B, and C are Cauchy parameters and $k_o$ and D are Urbach parameters. While bulk measurements of organic materials have a zero extinction coefficient, polymer thin films can exhibit light scattering effects due to domain differences within the film or from surface roughness creating a non-zero value for $k$.

*In situ* measurements can be performed with ellipsometry using specialized flow cells with glass windows through which light can pass normal to the plane of the glass. With spectroscopic ellipsometry, kinetic data is recorded at a single angle of incidence but across all wavelengths retaining the ability to model both the refractive index and

thickness of polymer films as changes in the film occur. Owing to the fact that the light is passing through the solvent and polymer layers there are no thickness limitations on polymer films. These capabilities make elliposmetry a powerful tool in determining the properties of thin films.

**Thin Film Reaction Kinetics**

With optical techniques like SPR and ellipsometry, thin film reactions can be observed *in situ* and applied for a variety of reactions from the deposition of monolayers to functionalization of polymers. Interfacial reactions are unique as they involve a variety of limitations from mass transport phenomena to reaction conditions.[89-91] One limitation of interfacial reactions is the barrier presented by the surface, which is a boundary layer preventing mass transport.[89, 91, 92] In diffusion limited reactions, this barrier is simply the point beyond which no diffusion occurs. However, in systems where flow is involved, the surface is a boundary condition where fluid flow is restricted. While mass transport dynamics need to be addressed, some simple steps can be used to reduce the necessity of solving the mass transport equations. Similarly, the reaction has limitations such as an unknown concentration of any surface bound reactive species.[93-96] Regardless of these limitations the solutions to the differential reaction dynamic equations can be derived from fundamental kinetic rate equations.[90]

Derivation of the rate equations for surface reactions begins by appropriately defining the reaction being studied.[90, 95, 97, 98] For most surface reactions, the rate equation will involve only two reactive species and follow the second order reaction presented in Eq. 26,

$$A + S \xrightarrow{k} SA \tag{26}$$

where an analyte in solution A will react with a surface bound species S to form a single, surface bound product SA. The rate equation can therefore be derived for the formation of the product in terms of concentration $[SA]$ by Eq. 27,

$$r_{SA} = \frac{d[SA]}{dt} = k[A][S] \tag{27}$$

where $r_{SA}$ is the rate of formation of SA and $k$ is the rate constant for the reaction. In order to solve the differential, a correlation between the product's rate of formation and the reactant's rate of consumption is made such that the rates are equivalent; $r_{SA} = -r_A = -r_S$, where $r_A$ and $r_S$ are the consumption rates for A and S, respectively. By writing the rate equation for S, the rate can be written as Eq. 28,

$$r_S = \frac{d[S]}{dt} = -k[A][S] \ . \tag{28}$$

The rate expression for S can be simplified to a pseudo-first order reaction with the use of excess reagent. In the case of a surface reaction, solution analyte is in excess of the surface bound reactant, $[S] \ll [A]$. As the reaction proceeds, the rate of change in A is considered to be negligible, $r_A \approx c$, where $c$ is a constant. With a constant concentration of A, the differential can be simplified to a pseudo-first order reaction by $k' = k[A]$ which can then be explicitly solved to produce Eq. 29,

$$S = S_o e^{-k't} \tag{29}$$

where $S$ can be any measured parameter and $S_o$ is the initial value for $S$ at t = 0. The pseudo-first order rate constant $k'$ is then determined by fitting Eq. 29 to kinetic data. With a series of reactions using different concentrations of the analyte, the second order rate constant can be determined from the slope of the pseudo-first order rate constant relative to the analyte concentrations.

The derivation up to this point can be applied for solution and surface reactions and thus far has assumed no limitations on the reaction. Interfacial reactions are strongly influenced by steric effects, which has been shown on monolayer systems or involve diffusion limitations in polymer brushes.[92, 95, 96, 99] In each of these cases, the kinetic data exhibit a plateau which is normally indicative of a complete reaction, however, all surface sites might not have reacted, $[S]_{tot} \neq [S_r]_{t=\infty}$, where $[S]_{tot}$ is the total concentration of S and $S_r$ is the amount of reacted S. In order to compensate this disparity, a limit is placed onto the kinetic model to account for the reduced concentration, Eq. 30,

$$ln\left(\frac{S-S_\infty}{S_o-S_\infty}\right) = -k't \tag{30}$$

where $S_\infty$ is taken as the asymptotic limit in the kinetic data. This technique is advantageous as it applies to any surface reaction where $[S]$ is implicitly interpreted from the kinetic data. It is imperative to note that the negative sign denotes the disappearance of the measured quantity for S. When monitoring surface reactions, it is often difficult to monitor S directly. For example, polymer growth in a "grafting from" reaction is limited by the concentration of the surface bound initiator, but in order to monitor the growth, a series of thickness measurements can be performed. In this example, kinetic data is measured only as the product is formed to which the same rate equations can apply based on correlation between the rates, $r_{SA} = -r_A = -r_S$. These limitations on kinetic rates have been applied to several surface reactions in order to elucidate rate constants for monolayer coverage formation and polymer brush functionalization.[95, 97, 98]

In determining kinetic rates, the conditions of the reactions are typically set such that mass transport phenomena are negligible. These conditions can be met in solution

reactions by continuous mixing of the solution. For surface reactions, the continuous supply of A to the reaction interface can be accomplished by convective mixing, steady fluid flow, or sufficiently high concentrations of A to negate diffusion limitations in solution. In these cases, the concentration of A at the reactive interface can be considered a constant, thus satisfying the pseudo-first order reaction condition used to solve for Eq. 29. In the presence of a permeable reactive layer, such as in the case of functional polymer brushes, the mass transport through the brush cannot be assumed to be negligible in all reactions. This phenomena is important when considering a reaction within a polymer brush, such as the post-polymerization functionalization of activated esters.[95, 97]

Reactions within polymer films add another dimension to the kinetic analysis which can potentially effect the dynamics of the reaction.[95, 96] Figure 1.12 depicts a generalized post-polymerization reaction where the reaction proceeds over time. Surface reactions occur when the analyte in solution comes into contact with the reactive surface as shown in Figure 1.12a. For two-dimensional reactive surfaces, such as monolayers, the depth of the film does not affect the reaction due to all reactive species being in the same plane. Polymers brushes with reactive side chains require the analyte to penetrate into the brush in order for the reaction to occur.[95, 96] As the polymer brush reaction progresses the analyte will react in a top-down fashion causing the top of the polymer layer to be functionalized before reacting with the active sites buried within the brush, Figure 1.12b. Over time, the functionalized layer, $d_2$, will increase relative to the amount of unreacted polymer, $d_1$. The degree of functionalization can be estimated by using the grafting density σ and thickness d relationship from Eq. 31,

$$\sigma = \frac{d\rho N_A}{M_n} \tag{31}$$

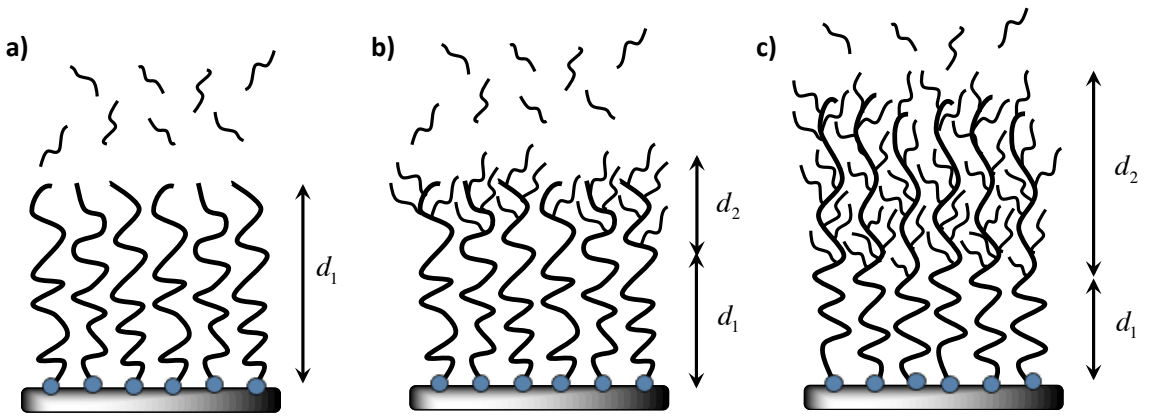


**Figure 1.12.** Post-polymerization functionalization of a surface bound polymer brush. As a) the analyte is exposed to the brush b) functionalization will form in a top down fashion until c) a mass transport barrier is created.

where $M_n$ is the molecular weight of the brush and $N_A$ is Avogadro's number.[94, 96] As the reaction proceeds, the mass transport of the analyte into the brush can become hindered by a diffusive barrier created either from the functionalized layer or from penetrating further into the brush, Figure 1.12c. The formation of this barrier will result in a deviation from the interfacial reaction kinetic model.

While the diagram in Figure 1.12 depicts the polymer brush in a near vertical fashion, the actual layering of the polymer chains takes on more of a random walk configuration with chain ends buried within polymer. The density of free chain ends as a function of polymer height takes on a parabolic shape relative to the thickness of the polymer.[100, 101] Monomer density within the polymer was also computed relative to the molecular weight and height at a constant grafting density with higher densities near the surface.[100] As the molecular weight was increased, monomer density adopts a monotonically decreasing slope with lower monomer densities at the top of the brush and

increases going down into the brush. The increase in monomer density coincides with the theory that mass transport will be affected as analyte penetrates into the brush. While Figure 1.12 does not accurately depict the polymer brush, such non-idealities are not incorporated into the kinetic and mass transport rate equations.

In a previous study with poly(NHS4VB), the mass transport rate through a polymer brush with activated esters was shown to affect the reaction rate under certain conditions.[95] In this case, application of Eq. 30 is not valid as it assumes negligible mass transport effects within a polymer brush. To account for the change in the kinetic rates, a diffusion rate equation was added to the series of reaction equations, Eq. 32,

$$\frac{dA}{dt} = k_d A = C \tag{32}$$

where $k_d$ is the time dependent diffusion rate constant and C is a constant. Time dependent diffusion is considered constant as the analyte's diffusion coefficient within the polymer brush is assumed to be constant. Adaptation of this condition into the rate equations yielded Eq. 33,

$$\frac{S_\infty}{S_o - S_\infty} ln\left(\frac{S - S_\infty}{S_o - S_\infty}\right) = -k't \tag{33}$$

which was applied for the functionalization measurements in the diffusion limited region only. While the decreased rate of functionalization did indicate a limitation on mass transport, the rate equations can not elucidate whether the change is due to the diffusion through the polymer or if a blocking layer is forming.

In either scenario, other effects on reaction conditions are also important in determining rates of reaction. Of these, polymer solvation, grafting density, and location of the reactive groups are the most important.[37, 93, 96, 97, 102, 103] Without proper solvation of the polymer film the transport of the analyte to the reactive sites will be greatly

limited. At high grafting densities, the crowding of polymer chain side groups can occur as the polymers become densely packed together. This can lead to slower mass transport into the brush as analyte diffuses to the reactive site, decreasing the rate of reaction and percent functionalization. Overcrowding of post-functionalized polymer brushes has been taken into account by Schuh *et al*. by diluting reactive side group by co-polymerizing with a second monomer,[96] however, a correlation between grafting density and reaction rates has yet to be determined. Congruently, the combined effects of solvation and grafting can alter the pictorial model represented in Figure 1.12. With low grafting density and a bad solvent, polymer films can be pictured much like the mushroom image in Figure 1.1. Lastly, the location of the functionalization sites will also determine the rate of the reaction. Despite all these possible variances, the basic interfacial reaction principles discussed can be applied to derive an appropriate kinetic model.

**Objective and Outline of this Dissertation**

In this dissertation, label-free tracking techniques are utilized to probe the dynamics of polymer thin films. More specifically, optical techniques such as SPR and ellipsometry are explored as versatile, non-invasive tool for monitoring interfacial interactions. By using these tools the optical properties of thin films have been investigated. Providing not only thickness and refractive index information but also elucidating how films change when acted on by external stimuli. Similarly, the interaction between light and polymer film allows for observation of dynamic properties in reaction kinetics and polymer-solvent interaction. Integration of these tools with fluid dynamic systems has led to *in situ* kinetic tracking of polymer thin films.

Chatper 2 of this dissertation focuses on the incorporation of microfluidic SPR devices with the goal of developing high-throughput devices for *in situ* tracking of interfacial reactions. Microfluidic devices were created using thiolene resins with a photolithographic technique that conserved the integrity of the SPR substrate for surface modification through self-assembly. These devices exhibit improved organic solvent compatibility over conventional materials used to fabricate microfluidics. *In situ* SPRI tracking of a binding event and solvent effects are presented to demonstrate the versatility of the thiolene microfluidics.

Chapter 3 investigates how a microfluidic SPRI device can be used to monitor refractive index increments of polymers. A linear concentration gradient was generated within a microfluidic device using a baffled mixing design. Flow dynamics within the mixer are explored using COMSOL simulations and fluorescence microscopy. SPR

imaging is used to track polymer refractive index increments as the linear mixer creates a concentration gradient of water-soluble polymers.

Chapter 4 utilizes the gratings on a blu-ray disc to create a molecularly imprinted SPR sensor. Molecularly imprinted polymers are attached to the surface of a Ag coated blu-ray disc using "grafting-through" photopolymerization to encapsulate a target molecule. Rigorous coupled wave analysis is used to predict the shifts in the single, grating coupled plasmon dip due to changes in thickness and refractive index of the imprinted polymer. Binding of histamine and microcysin-LR toxins are used to demonstrate the effectiveness of the blu-ray disc SPR sensor.

Chapter 5 explores the dynamics of thermo-repsonsive hydrogels for the release of therapeutic drugs. Poly(N-isopropyl acrylamide) is used as a drug carrier that can collapse when ambient temperatures are raised about its lower critical solution temperature. The swelling and collapse of the polymer is investigated using *in situ* spectroscopic ellipsometry. Drug release rates are explored using doxorubicin and are monitored by UV-vis.

Chapter 6 summarizes the various projects presented in this dissertation and provides an outlook on their impacts on future studies.

## References


1. Schasfoort, R. B. M., *Expert Review of Proteomics* **2004,** *1* (1), 123-132.

2. Lee, H. J.; Wark, A. W.; Corn, R. M., *Langmuir* **2006,** *22* (12), 5241-5250.

3. Asanuma, H.; Hishiya, T.; Komiyama, M., *Adv. Mater.* **2000,** *12* (14), 1019-1030.

4. Takeuchi, T.; Haginaka, J., *Journal of Chromatography B: Biomedical Sciences and Applications* **1999,** *728* (1), 1-20.

5. Haes, A. J.; Chang, L.; Klein, W. L.; Van Duyne, R. P., *J. Am. Chem. Soc.* **2005,** *127* (7), 2264-2271.

6. de Jong, J.; Lammertink, R. G. H.; Wessling, M., *Lab on a Chip* **2006,** *6* (9), 1125-1139.

7. Hansen, C.; Quake, S. R., *Current Opinion in Structural Biology* **2003,** *13* (5), 538-544.

8. Arnold, R. M.; Huddleston, N. E.; Locklin, J., *J. Mater. Chem.* **2012,** *22* (37), 19357-19365.

9. Jain, P.; Baker, G. L.; Bruening, M. L., *Annual Review of Analytical Chemistry* **2009,** *2* (1), 387-408.

10. Brockman, J. M.; Nelson, B. P.; Corn, R. M., *Annu. Rev. Phys. Chem.* **2000,** *51* (1), 41-63.

11. Whitesides, G. M., *Nat Biotech* **2003,** *21* (10), 1161-1165.

12. Fries, K. H.; Driskell, J. D.; Sheppard, G. R.; Locklin, J., *Langmuir* **2011,** *27* (19), 12253-12260.

13. Roy, D.; Fendler, J., *Adv. Mater.* **2004,** *16* (6), 479-508.

14. Pieczonka, N. P. W.; Aroca, R. F., *ChemPhysChem* **2005,** *6* (12), 2473-2484.

15. Stiles, P. L.; Dieringer, J. A.; Shah, N. C.; Van Duyne, R. P., *Annual Review of Analytical Chemistry* **2008,** *1* (1), 601-626.

16. Liebermann, T.; Knoll, W., *Colloids and Surfaces A: Physicochemical and Engineering Aspects* **2000,** *171* (1-3), 115-130.

17. Lee, H. J.; Goodrich, T. T.; Corn, R. M., *Anal. Chem.* **2001,** *73* (22), 5525-5531.

18. Lee, H. J.; Wark, A. W.; Corn, R. M., *Analyst* **2008,** *133* (8), 975-983.

19. Boozer, C.; Kim, G.; Cong, S.; Guan, H.; Londergan, T., *Curr. Opin. Biotechnol.* **2006,** *17* (4), 400-405.

20. Whitesides, G. M., *Nat Biotech* **2003,** *21* (10\), 1161\-1165\.

21. Orski, S. V.; Fries, K. H.; Sontag, S. K.; Locklin, J., *J. Mater. Chem.* **2011,** *21* (37), 14135-14149.

22. Love, J. C.; Estroff, L. A.; Kriebel, J. K.; Nuzzo, R. G.; Whitesides, G. M., *Chem. Rev.* **2005,** *105* (4), 1103-1170.

23. Ulman, A., *Chem. Rev.* **1996,** *96* (4), 1533-1554.

24. Schreiber, F., *Prog. Surf. Sci.* **2000,** *65* (5-8), 151-257.

25. Schwartz, D. K., *Annu. Rev. Phys. Chem.* **2001,** *52* (1), 107-137.

26. Smith, E. A.; Thomas, W. D.; Kiessling, L. L.; Corn, R. M., *J. Am. Chem. Soc.* **2003,** *125* (20), 6140-6148.

27. Lee, H. J.; Wark, A. W.; Corn, R. M., *Analyst* **2008,** *133* (5), 596-601.

28. Brittain, W. J.; Minko, S., *J. Polym. Sci., Part A: Polym. Chem.* **2007,** *45* (16), 3505-3512.

29. Chen, W. Y.; Zheng, J. X.; Cheng, S. Z. D.; Li, C. Y.; Huang, P.; Zhu, L.; Xiong, H.; Ge, Q.; Guo, Y.; Quirk, R. P.; Lotz, B.; Deng, L.; Wu, C.; Thomas, E. L., *Phys. Rev. Lett.* **2004,** *93* (2), 028301.

30. Milner, S. T., *Science* **1991,** *251* (4996), 905-914.

31. Toomey, R.; Tirrell, M., *Annu. Rev. Phys. Chem.* **2008,** *59* (1), 493-517.

32. Edmondson, S.; Osborne, V. L.; Huck, W. T. S., *Chem. Soc. Rev.* **2004,** *33* (1), 14-22.

33. Rühe, J., Polymer Brushes: On the Way to Tailor-Made Surfaces. In *Polymer Brushes*, Wiley-VCH Verlag GmbH & Co. KGaA: 2005; pp 1-31.

34. Xia, Y.; Whitesides, G. M., *Angew. Chem. Int. Ed.* **1998,** *37* (5), 550-575.

35. Ionov, L.; Zdyrko, B.; Sidorenko, A.; Minko, S.; Klep, V.; Luzinov, I.; Stamm, M., *Macromol. Rapid Commun.* **2004,** *25* (1), 360-365.

36. Advincula, R. C., Brittain, W. J., Caster, K. C. and Rühe, J. (eds), In *Polymer Brushes*, Wiley-VCH Verlag GmbH & Co. KGaA: 2005.

37. Michailidou, V. N.; Loppinet, B.; Prucker, O.; Rühe, J.; Fytas, G., *Macromolecules* **2005,** *38* (21), 8960-8962.

38. Zhou, F.; Huck, W. T. S., *PCCP* **2006,** *8* (33), 3815-3823.

39. Odian, G., *Principles of Polymerization*. John Wiley & Sons, Inc.: 2004.

40. Sheiko, S. S.; Sumerlin, B. S.; Matyjaszewski, K., *Prog. Polym. Sci.* **2008,** *33* (7), 759-785.

41. Braunecker, W. A.; Matyjaszewski, K., *Prog. Polym. Sci.* **2007,** *32* (1), 93-146.

42. Bialk, M.; Prucker, O.; Rühe, J., *Colloids and Surfaces A: Physicochemical and Engineering Aspects* **2002,** *198-200* (0), 543-549.

43. Mosbach, K.; Ramstrom, O., *Nat Biotech* **1996,** *14* (2), 163-170.

44. Cai, D.; Ren, L.; Zhao, H.; Xu, C.; Zhang, L.; Yu, Y.; Wang, H.; Lan, Y.; Roberts, M. F.; Chuang, J. H.; Naughton, M. J.; Ren, Z.; Chiles, T. C., *Nat Nano* **2010,** *5* (8), 597-601.

45. Chen, H. C.; Lee, Y. C.; Hwang, D. F.; Chiou, T. K.; Tsai, Y. H., *Journal of Food Safety* **2011,** *31* (3), 320-325.

46. Knoll, W., *Annu. Rev. Phys. Chem.* **1998,** *49* (1), 569-638.

47. Lee, H. J.; Goodrich, T. T.; Corn, R. M., *Anal Chem* **2001,** *73* (22), 5525-5531.

48. Campbell, C. T.; Kim, G., *Biomaterials* **2007,** *28* (15), 2380-2392.

49. Homola, J., *Chem. Rev.* **2008,** *108* (2), 462-493.

50. Mayer, K. M.; Hafner, J. H., *Chem. Rev.* **2011,** *111* (6), 3828-3857.

51. Schuck, P., *Annu. Rev. Biophys. Biomol. Struct.* **1997,** *26* (1), 541-566.

52. Schasfoort, R. B. M. a. T., Anna J., In *Handbook of Surface Plasmon Resonance*, Schasfoort, R. B. M.; Tudos, A. J., Eds. The Royal Society of Chemistry: 2008.

53. Senaratne, W.; Andruzzi, L.; Ober, C. K., *Biomacromolecules* **2005,** *6* (5), 2427-2448.

54. Azzam, R. M. A.; Bashara, N. M., *Ellipsometry and Polarized Light*. Elsevier: Amsterdam, 1987.

55. Knoll, W. Max Planck Institute for Polymer Research, Winspall Software. http://www.mpip-mainz.mpg.de/groups/knoll/software.

56. Lee, K.-H.; Su, Y.-D.; Chen, S.-J.; Tseng, F.-G.; Lee, G.-B., *Biosensors & Bioelectronics* **2007,** *23* (4), 466-472.

57. Smith, E. A.; Thomas, W. D.; Kiessling, L. L.; Corn, R. M., *Journal of the American Chemical Society* **2003,** *125* (20), 6140-6148.

58. Wegner, G. J.; Wark, A. W.; Lee, H. J.; Codner, E.; Saeki, T.; Fang, S.; Corn, R. M., *Anal. Chem.* **2004,** *76* (19), 5677-5684.

59. Azzaroni, O.; Mir, M.; Knoll, W., *J. Phys. Chem. B* **2007,** *111* (48), 13499-13503.

60. Pei, R.; Yang, X.; Wang, E., *Analyst (Cambridge, United Kingdom)* **2001,** *126* (1), 4-6.

61. Iwasaki, Y.; Tobita, T.; Kurihara, K.; Horiuchi, T.; Suzuki, K.; Niwa, O., *Meas. Sci. Technol.* **2006,** *17* (12), 3184-3188.

62. Liu, J.; Eddings, M. A.; Miles, A. R.; Bukasov, R.; Gale, B. K.; Shumaker-Parry, J. S., *Anal. Chem.* **2009,** *81* (11), 4296-4301.

63. Ly, N.; Foley, K.; Tao, N., *Anal Chem* **2007,** *79* (6), 2546-2551.

64. Ayres, N., *Polymer Chemistry* **2010,** *1* (6), 769-777.

65. Wegner, G. J.; Wark, A. W.; Lee, H. J.; Codner, E.; Saeki, T.; Fang, S.; Corn, R. M., *Anal. Chem.* **2004,** *76* (19), 5677-5684.

66. Yu, F.; Knoll, W., *Anal. Chem.* **2004,** *76* (7), 1971-1975.

67. Homola, J.; Koudela, I.; Yee, S. S., *Sensors and Actuators B: Chemical* **1999,** *54* (1-2), 16-24.

68. Piliarik, M.; Homola, J., *Opt. Express* **2009,** *17* (19), 16505-16517.

69. Lin, K.; Lu, Y.; Chen, J.; Zheng, R.; Wang, P.; Ming, H., *Opt. Express* **2008,** *16* (23), 18599-18604.

70. Baba, A.; Aoki, N.; Shinbo, K.; Kato, K.; Kaneko, F., *ACS Applied Materials & Interfaces* **2011,** *3* (6), 2080-2084.

71. Raether, H., *Optics Communications* **1982,** *42* (4), 217-222.

72. Chien, F. C.; Lin, C. Y.; Yih, J. N.; Lee, K. L.; Chang, C. W.; Wei, P. K.; Sun, C. C.; Chen, S. J., *Biosens. Bioelectron.* **2007,** *22* (11), 2737-2742.

73. Marikkar, F. S.; Carter, C.; Kieltyka, K.; Robertson, J. W. F.; Williamson, C.; Simmonds, A.; Zangmeister, R.; Fritz, T.; Armstrong, N. R., *Langmuir* **2007,** *23* (20), 10395-10402.

74. McPhillips, J.; McClatchey, C.; Kelly, T.; Murphy, A.; Jonsson, M. P.; Wurtz, G. A.; Winfield, R. J.; Pollard, R. J., *The Journal of Physical Chemistry C* **2011,** *115* (31), 15234-15239.

75. Bratton, D.; Yang, D.; Dai, J.; Ober, C. K., *Polym. Adv. Technol.* **2006,** *17* (2), 94-103.

76. Kaplan, B.; Guner, H.; Senlik, O.; Gurel, K.; Bayindir, M.; Dana, A., *Plasmonics* **2009,** *4* (3), 237-243.

77. Singh, B. K.; Hillier, A. C., *Anal. Chem.* **2008,** *80* (10), 3803-3810.

78. Singh, B. K.; Hillier, A. C., *Anal. Chem.* **2006,** *78* (6), 2009-2018.

79. Yeh, W.-H.; Kleingartner, J.; Hillier, A. C., *Anal. Chem.* **2010,** *82* (12), 4988-4993.

80. Habicht, J.; Schmidt, M.; Ruhe, J.; Johannsmann, D., *Langmuir* **1999,** *15* (7), 2460-2465.

81. Bittrich, E.; Burkert, S.; Müller, M.; Eichhorn, K.-J.; Stamm, M.; Uhlmann, P., *Langmuir* **2012,** *28* (7), 3439-3448.

82. Theeten, J. B.; Aspnes, D. E., *Annu. Rev. Mater. Sci.* **1981,** *11* (1), 97-122.

83. Zudans, I.; Heineman, W. R.; Seliskar, C. J., *The Journal of Physical Chemistry B* **2004,** *108* (31), 11521-11528.

84. Fujiwara, H., *Spectoscopic Ellipsometry: Principles and Applications*. John Wiley & Sons, Ltd, Chichester, UK: 2007.

85. Tompkins, H. G. a. M., William A., *Spectroscopic Ellipsometry and Reflectometry: A User's Guide*. Wiley-Interscience: 1999.

86. Azzam, R. M. A., *physica status solidi (a)* **2008,** *205* (4), 709-714.

87. Plunkett, K. N.; Zhu, X.; Moore, J. S.; Leckband, D. E., *Langmuir* **2006,** *22* (9), 4259-4266.

88. Dow, J. D.; Redfield, D., *Physical Review B* **1972,** *5* (2), 594-610.

89. Freeman, D. L.; Doll, J. D., *The Journal of Chemical Physics* **1983,** *78* (10), 6002-6009.

90. Levenspiel, O., *Chemical Reaction Engineering*. 3rd Ed. ed.; John Wiley & Sons: 1999.

91. Welty, J. R.; Wicks, C. E.; Wilson, R. E.; Rorrer, G. L., *Fundamental of Momentum, Heat, and Mass Transfer*. 4th Ed. ed.; John Wiley & Sons, Inc.: 2001.

92. Filippidi, E.; Michailidou, V.; Loppinet, B.; Rühe, J.; Fytas, G., *Langmuir* **2007,** *23* (9), 5139-5142.

93. Schönherr, H.; Feng, C.; Shovsky, A., *Langmuir* **2003,** *19* (26), 10843-10851.

94. Murata, H.; Prucker, O.; Ruhe, J., *Macromolecules* **2007,** *40* (15), 5497-5503.

95. Orski, S. V.; Sheppard, G. R.; Arumugam, S.; Arnold, R. M.; Popik, V. V.; Locklin, J., *Langmuir* **2012,** *28* (41), 14693-14702.

96. Schuh, C.; Rühe, J., *Macromolecules* **2011,** *44* (9), 3502-3510.

97. Arnold, R. M.; Sheppard, G. R.; Locklin, J., *Macromolecules* **2012,** *45* (13), 5444-5450.

98. Sontag, S. K.; Sheppard, G. R.; Usselman, N. M.; Marshall, N.; Locklin, J., *Langmuir* **2011,** *27* (19), 12033-12041.

99. Prucker, O.; Ruhe, J., *Macromolecules* **1998,** *31* (3), 602-613.

100. Milner, S. T., *J. Chem. Soc., Faraday Trans.* **1990,** *86* (9), 1349-1353.

101. Spiliopoulos, N.; Koutsioubas, A. G.; Anastassopoulos, D. L.; Vradis, A. A.; Toprakcioglu, C.; Menelle, A.; Mountrichas, G.; Pispas, S., *Macromolecules* **2009,** *42* (16), 6209-6214.

102. Advincula, R. C., The Analysis and Characterization of Polymer Brushes: From Flat Surfaces to Nanoparticles. In *Polymer Brushes*, Wiley-VCH Verlag GmbH & Co. KGaA: 2005; pp 187-212.

103. Kwon, Y.; Mrksich, M., *J. Am. Chem. Soc.* **2002,** *124* (5), 806-812.

# CHAPTER 2

# THIOLENE-BASED MICROFLUIDIC FLOW CELLS FOR SURFACE PLASMON RESONANCE IMAGING[1]

[1] Sheppard, G. R.; Oseki, T.; Baba, A.; Patton, D.; Kaneko, F.; Mao, L.; and Locklin, J., 2011, *Biomicrofluidics*, 5 (2), 026501-6. Reprinted here with permission from the American Institute of Physics.

**Abstract**

Thiolene based microfluidic devices have been coupled with surface plasmon resonance imaging (SPRI) to provide an integrated platform to study interfacial interactions in both aqueous and organic solutions. In this work, we develop a photolithographic method that interfaces commercially available thiolene resin to gold and glass substrates to generate microfluidic channels with excellent adhesion that leave the underlying sensor surface free of contamination and readily available for surface modification through self-assembly. These devices can sustain high flow rates and have excellent solvent compatibility, even with several organic solvents. To demonstrate the versatility of these devices, we have conducted nanomolar detection of streptavidin-biotin interactions using *in situ* SPRI.

## Introduction

Surface plasmon resonance imaging (SPRI) is a label-free detection technique that can provide real-time monitoring of spatially-resolved refractive index changes that occur near a noble metal surface.[1-7] SPRI devices use a CCD camera to monitor the reflected light, which is sensitive to differences in refractive index (RI) and film thickness at the sensor's interface. This technique is extremely powerful, in that real-time kinetic and thermodynamic analysis of surface and interfacial interactions can be monitored.[3-6, 8-12] It is also amenable to parallel analysis of adsorption events in an array format.[13, 14] Rapid analyses of biomolecular interactions using SPRI arrays have been investigated recently.[15-18] Coupling SPRI with microfluidics provides an integrated platform for *in situ* biomolecular studies while greatly reducing the consumption of sample reagents.[11, 19-22] Polydimethylsiloxane (PDMS) is a widely used material in the fabrication of microfluidic devices with aqueous systems, because of its excellent optical properties, biocompatibility, air-permeability and low cost.[14, 23-27] However, PDMS devices perform poorly with the introduction of organic solvents into the channels, resulting in solvent leakage or swelling.[23, 28, 29] Swelling of PDMS can lead to significant changes in the cross-sectional area of microchannels, which can alter the flow rates and flow dynamics, leaching of uncured monomers from the side-walls into the channel or sensor surface, cross-contamination of adjacent microchannels, leakage of solvents, and ultimately, device failure. The incompatibility between PDMS and organic solvents also limits the variety of chemical processes that can be performed in microfluidic devices, particularly when interfaced to a gold substrate, where the adhesion is very weak. This is a limiting factor when developing microchannels for SPRI applications, even for aqueous systems,

since surface functionalization of the channels typically starts with an organic phase alkane thiol modification step.

Due to solvent incompatibility and adhesion difficulties between PDMS and Au substrates, an alternative material is necessary to develop organic-phase based microfluidic devices. Thiolene-based optical adhesives are excellent candidates for these applications, as they have provided excellent versatility and solvent compatibility in both water and a wide variety of non-halogenated organic solvents.[28, 30] Rapid prototyping with commercially available thiolene resins allows simple fabrication of microfluidic devices with feature sizes as small as 70 μm.[28, 31-33] However, current fabrication techniques of thiolene-based microfluidic devices present challenges for their integration with SPRI systems. Thiolene resins bind strongly to gold surfaces through free thiols, making reproducible functionalization of gold sensor surfaces arduous. In this study, we have developed an alternative strategy of fabricating thiolene-based microfluidic devices and successfully integrated them with a SPRI system without contaminating the sensor surface. As a proof of concept, we demonstrated the reproducible functionality of the sensor surface using a common binding assay of biotinylated monolayers and streptavidin (SA). The devices were also able to sustain high flow rates with very limited swelling effects and no solvent leakage in several organic solvents. Samples of finished microfluidic devices are shown in Figure 2.1(a). Figures 2.1(b) and (c) depict representative mask designs of microfluidic channels and the corresponding SPR images of solvents within the channels.

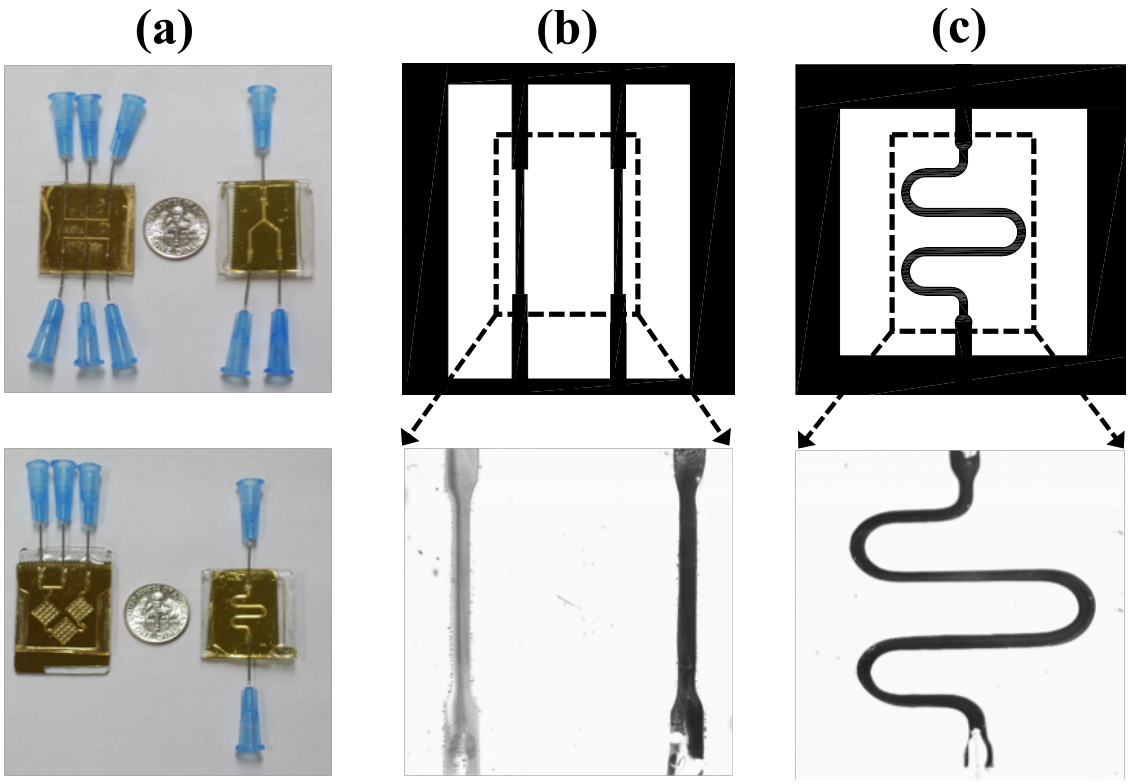


**Figure 2.1.** (a) The fabricated microfluidic devices with dime-sized imaging windows. (b) Mask design (top) and SPR image (bottom) of straight channels. The SPR image compares channels filled with water (left) to isopropanol (right). The difference in pixel intensity is due to the refractive index mismatch of two solutions. (c) Mask design (top) and SPR image (bottom) of serpentine channel. SPR image was taken using phosphate buffer solution (PBS). The width of channels in (b) and (c) is 600 μm; the thickness is 1000 μm.

**Device Fabrication**

Standard photolithographic techniques require ultra clean environments and typically involve negative master molds. The method used in this work utilizes standard office equipment to produce a variety of microfluidic designs that do not require a master mold for replication nor clean room facilities. Figures 2.2(a) – (e) show the materials and fabrication process of thiolene-based microfluidic devices. Masks of microfluidic devices were drawn to scale using AutoCAD (Autodesk Inc., San Rafael, CA) and printed on laser transparency films with a commercial laser printer (HP LaserJet 1022, 1200 DPI). The transparency mask was taped to a glass slide for selective photopolymerization of thiolene resin (NOA 81 optical adhesive, Norland Product Inc., Cranbury, NJ), which occur under ultra-violet (UV) light exposure. Polymerization occurs where the UV radiation passes through the mask, the channels formed from masked areas where the radiation is blocked. The microfluidic channel thickness depends upon the UV light penetration into liquid thiolene. It has been observed previously that the maximum penetration depts. is 63.5 cm.[34] A PDMS "reactor" was used to cure the thiolene because of very poor adhesion between thiolene and PDMS. The reactor was formed from a mixture of silicone elastomer base and curing agent (Sylgard 184 Kit, Dow Corning, Hemlock, MI) in a 10:1 mass ratio. Degassed PDMS is poured over a glass slide or silicon wafer, 1.0 mm and 0.5 mm thick, cut to the desired reactor size and cured at 70°C for 2 hours. Once cured, the spacer slide is removed leaving a uniform reactor. The PDMS reactor can be filled with thiolene resin as shown in Figure 2.2(a).

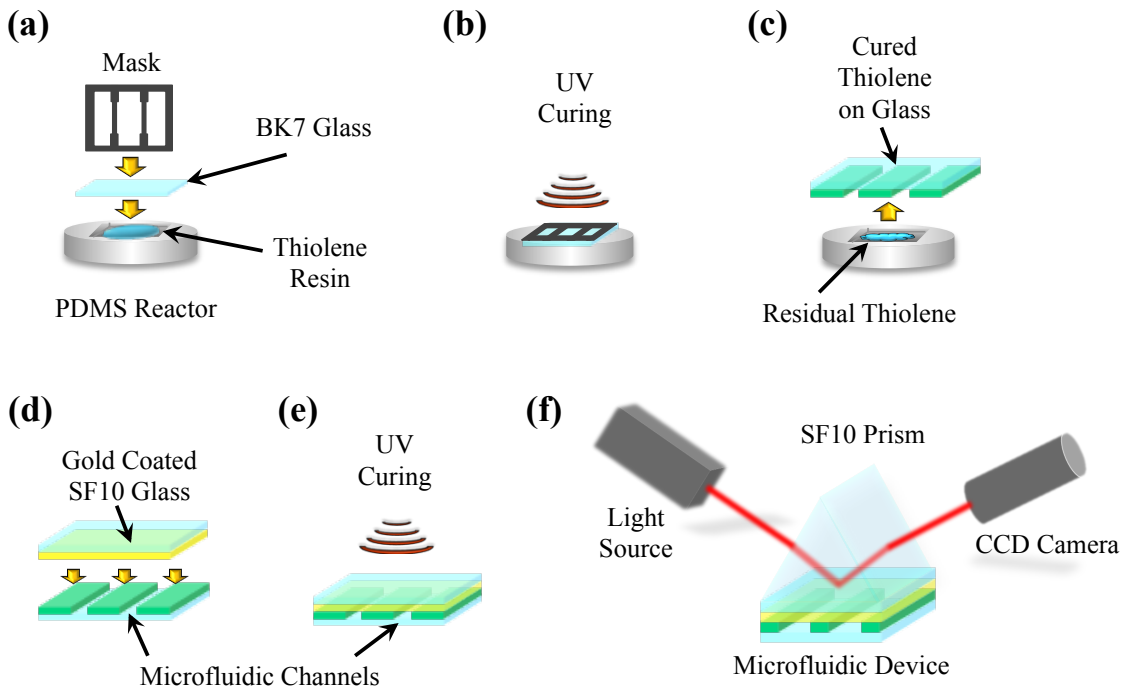


**Figure 2.2.** (a – e) Thiolene microfluidic device fabrication scheme. Transparency printed mask was taped to a BK7 glass slide before being placed onto thiolene filled PDMS reactor. Exposure to UV light photopolymerized the thiolene resin and formed the microfluidic channels. A gold-coated SF10 slide was used to cap the channels. (f) The experimental setup followed the Kretschmann configuration where the SF10 prism and device were coupled using refractive index matching fluid. Images are collected using a CCD camera.

During device fabrication, the mask was attached to a BK7 glass (refractive index (RI) of 1.515 at $\lambda = 632.8$ nm) slide and lowered into contact with the thiolene resin filled PDMS reactor as shown in Figure 2.2(a). A UV light source was used to photopolymerize the thiolene resin with 200 $\mu W/cm^2$ power for 4.5 minutes (Figure 2.2(b)). After exposure, the thiolene resin was cured onto the glass slide and separated from the PDMS

reactor to form microfluidic channels. The channels were first rinsed with ethanol to remove any uncured material, and then rinsed with acetone followed by ethanol again before drying with a moderate flow rate of nitrogen gas. A secondary curing of the thiolene resins was performed with 1 minute UV exposure at 200 $\mu W/cm^2$ power. A thin film of thiolene was then carefully sprayed over cured thiolene patterns with a thin layer chromatography sprayer, providing a curable surface to bind to a gold-coated SF10 glass slide (RI of 1.723, $\lambda = 632.8$ nm). This is shown in Figure 2.2(d). The gold layer on SF10 glass slides was deposited by thermal evaporation using 1 nm thick chromium and 47 nm thick gold. The gold-coated SF10 glass slide was pressure sealed against the thiolene microfluidic channels on the BK7 glass slide and UV cured to form the final device (Figure 2.2(e)). Needles are then inserted and sealed at channel openings by applying thiolene resin and exposing to UV at 3 $mW/cm^2$. Exposing at a higher power setting ensures complete polymerization and reduces the amount of residual monomer in the completed device. The final device is heat cured at 50°C for 12 hrs. Overall, the device design and fabrication is low-cost, and can be completed within several hours.

**Surface Plasmon Resonance Imaging**

A SPRI system (SPRImager II, GWC Technologies, Madison, MI) consisting of a white light source with a 800 nm narrow band pass filter, polarizer, and a CCD camera was used for the *in situ* experiments. The finished thiolene-based microfluidic device was attached to the rotating stage of the SPRI system with a custom-made holder in the Kretschmann configuration.[5, 7, 9, 35] The light source of the SPRI system excited surface plasmon resonance at an angle intrinsic to the metal and substrate layers, as shown in Figure 2.2(f). A peristaltic pump was used to control the rate of fluid flow through the

microfluidic device. The system was setup to recycle fluid from the outlets back into the inlets; reducing the required volume to that of the microfluidic channel and connected tubing, totaling 1.0 mL for each solution. Upon changing solutions the system was taken out of recycle mode. The SPR signal intensity changes when the new solution passes across the sensor; from the flow rate and the remaining tubing volume the time to place the system back into recycle mode can be calculated preventing cross contamination of the solutions.

The binding of streptavidin (SA) to a biotinylated monolayer was used to determine the working parameters and detection limits of the microfluidic device with the SPRI system. Streptavidin has a tetrameric structure with a high affinity to biotin.[35] A thiolene microfluidic device with 600 μm by 1000 μm (aspect ratio, 1.67) was fabricated for the SA sensing. In order to coat the gold surface with biotin, a self-assembled monolayer was first deposited onto the gold by flowing 10 mM 11-mercaptoundecanoic acid (11-MUA) solution in ethanol through the microfluidic channels for 1.5 hours. The channels were rinsed with ethanol followed by isopropanol and deionized water for 30 minutes. Phosphate buffer solution (PBS) was flowed through the channels to ensure that any solvent mixing and the resulting refractive index change were minimized. A mixture of 0.2 M 1-ethyl-3-(3-dimethylaminopropyl) carbodiimide hydrochloride (EDC) and 0.05 M N-hydroxysuccinimide (NHS) was used to activate the carboxyl groups for reaction with amine terminated biotin. Finally, a solution containing 1 mg/mL amine-PEG3-biotin in PBS was flowed through the device at 3 μL/sec for 1.5 hours to coat the gold surface with biotin. Finally, streptavidin in PBS was flowed through the device at 3 μL/sec and the binding events were monitored in real-time by the SPRI system.

During the final PBS rinse, a thiolene microfluidic device attached on the rotating stage was adjusted to find the SPR minimum and then shifted 1 – 2 degrees to the left for the optimal imaging angle. Reference images are taken and regions of interest (ROI) were selected covering the channel for kinetics tracking. Subsequent SPR images are compared to the reference images from which the change in percent reflectivity (Δ%R) due to a binding event is monitored by difference image analysis.

**Results and Discussion**

A thiolene microfluidic device consisting of 600 μm wide channels was used to evaluate the binding kinetics of 75 μM streptavidin with a biotinylated monolayer, as depicted in Figure 2.3(a). The initial 500 seconds of the plot was PBS flow prior to streptavidin injection. The reflectivity difference before and after streptavidin injection clearly demonstrated that the gold surface was successfully functionalized with biotin, and the streptavidin was able to bind to biotin on the gold surface. Figure 2.3(b) compared a SPR image taken before streptavidin injection to an image taken after streptavidin flow for 100 minutes in recycle mode. Streptavidin-biotin binding shifted the SPR minimum to a larger angle, resulting in a clear reflectivity change as demonstrated by the pixel intensity level. Demonstrated in Figure 2.3(c) are difference images from which kinetic data is taken and provided ocular confirmation of the protein binding events allowing for high throughput protein sensing.

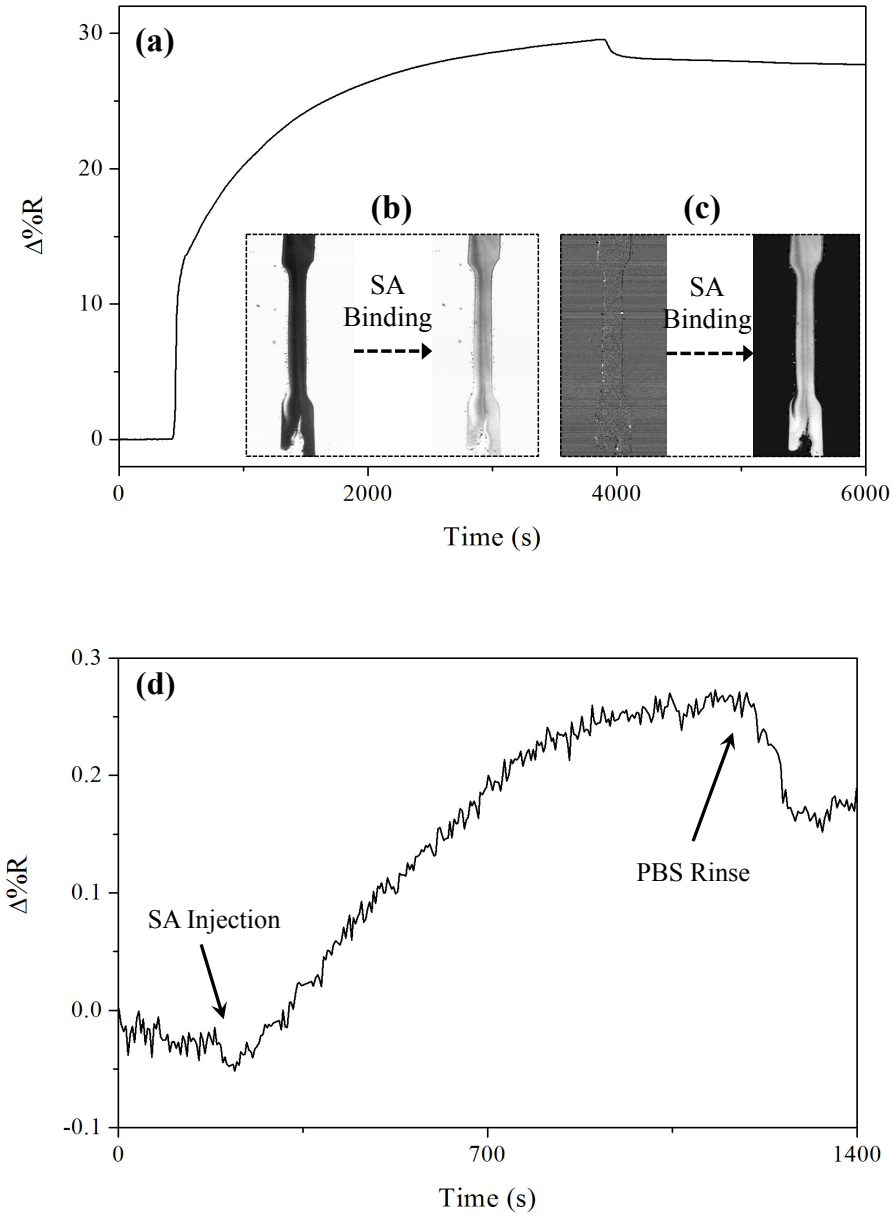


**Figure 2.3.** (a) Streptavidin (75 μM) binding to biotin functionalized monolayers on glass surface. SPR images (b) and difference images (c) taken before and after streptavidin flow in recycle mode. Unbound streptavidin was removed by PBS rinse at 65 min. (d) A low concentration of streptavidin (150 nM) injected over biotin functionalized monolayers on gold surface. Unbound streptavidin was removed by PBS rinse at 20 min.

The detection limit of streptavidin-biotin binding was characterized with a 150 nM streptavidin solution, as shown in Figure 2.3(d). Buffer solution is used to determine baseline reflectivity values prior to and after binding. After the initial SA binding, the peristaltic pump was stopped to allow for diffusion-limited binding to take place. The characteristic binding curve demonstrates the ability of thiolene based microfluidics to detect 5.4 ng/mm$^2$ of protein with an approximate limit of detection at 10 nM (0.4 ng/mm$^2$) in this system.

Thiolene microfluidic devices are more versatile in solvent compatablity than PDMS. Solvent compatiblity can be expressed in terms of a swelling ratio, $S = W/W_0$, where $W_0$ is the initial width and W is the width after solvent exposure.[29] Various solvents were passed through the thiolene microfluidic device for 2 hours to monitor thiolene swelling or delamination, $S^{\alpha}$ in Table 2.1. For channel swelling, values greater than one indicate delamination and values less than unity indicate swelling. SPR images of the channel were taken before and after exposure to solvent and the distance between the channal walls were measured using the number of pixals. A 24 hr swelling study on 2 mm square thiolene pieces, $S^{\beta}$, was also performed to compare directly to PDMS swelling ratios, $S^{\gamma}$ found in Reference 25. In the 24 hr study, thiolene squares were imaged with a microscope (Zeiss, AXIO Imager A2) using a 2.5x lens. For each solvent, three squares were measured and the edge-to-edge distance computed. Initial distances were determined from images taken prior to solvent exposure. After 24 hrs, the squares were imaged while still in solution to reduce the chances of deswelling associated with solvent evaporation. A value greater than 1 from the 24 hr experiment indicates the increase in size due to swelling effects. With little variation around unity for a majority of the solvents in Table

2.1, the perofrmance of the thiolene devices is excellent for most organic solvents. For halogenated solvents dichloromethane and chloroform, swelling causes the square to increase by 30 percent along any given cartesian coordinate. Solvents such as tetrahydrofuran can be used for limited time frames as indicated by the difference in $S^{\alpha}$ and $S^{\beta}$. Another important contrast is that thiolene microfluidic devices are compatible with certain organic solvents that PDMS is not, such as hexane, toluene, and ethyl ether.

**Table 2.1.** A swelling ratio ($S = W/W_0$) describes the amount of swelling or delamination due to solvent-thiolene interaction, a value of one denotes no change. $S^{\alpha}$ denotes microfluidic channel swelling after 2 hrs. $S^{\beta}$, solvent swelling on 2 mm squares of thiolene after 24 hrs. Thiolene swelling ratios are compared to PDMS's swelling ratio previously reported, $S^{\gamma}$, for 24 hrs. For channel swelling, $S^{\alpha}$, the initial width is larger than the final width resulting in values less than unity. ❖Value is for 1-propanol.

| | $S^{\alpha}$ | $S^{\beta}$ | $S^{\gamma}$ |
|---|---|---|---|
| $H_2O$ | 1.01 ± 0.02 | 1.01 ± 0.00 | 1.00 |
| Acetonitrile | - | 1.11 ± 0.01 | 1.01 |
| Ethyl Ether | - | 0.99 ± 0.01 | 1.38 |
| Acetone | 1.02 ± 0.03 | 1.12 ± 0.01 | 1.06 |
| Ethanol | 1.03 ± 0.03 | 1.00 ± 0.01 | 1.04 |
| Ethyl Acetate | 1.04 ± 0.02 | - | 1.18 |
| Hexane | 1.03 ± 0.04 | 1.00 ± 0.01 | 1.35 |
| Isopropanol | 0.93 ± 0.04 | 1.00 ± 0.00 | 1.09❖ |
| Tetrahydrofuran | 0.92 ± 0.01 | 1.16 ± 0.04 | 1.38 |
| Dichloromethane | - | 1.27 ± 0.03 | 1.22 |
| Chloroform | - | 1.34 ± 0.03 | 1.39 |
| Toluene | - | 1.02 ± 0.02 | 1.31 |

## Conclusions

A simple, low-cost thiolene microfluidic device has been designed and fabricated to allow for integration with SPRI systems with a wide range of solvents. Thiolene microfluidics are a robust tool for applications where PDMS devices fail, such as high pressure or applications that involve the use of organic solvents. These devices provide microfluidic channels with excellent adhesion and leave the underlying sensor surface free of contamination. Thiolene devices can sustain high flow rates and have excellent solvent compatibility, even with several organic solvents. The advantageous ability to use organic solvents with negligible swelling effects or channel leakage further increases versatility and utility of these devices for sensor applications on the microliter scale.

## References


1. Pei, R.; Yang, X.; Wang, E., *Analyst (Cambridge, United Kingdom)* **2001,** *126* (1), 4-6.

2. Harke, M.; Teppner, R.; Schulz, O.; Motschmann, H.; Orendi, H., *Review of Scientific Instruments* **1997,** *68* (8), 3130-3134.

3. Kim, S. J.; Gobi, K. V.; Iwasaka, H.; Tanaka, H.; Miura, N., *Biosensors & Bioelectronics* **2007,** *23* (5), 701-707.

4. Wang, Z.; Wilkop, T.; Xu, D.; Dong, Y.; Ma, G.; Cheng, Q., *Analytical and Bioanalytical Chemistry* **2007,** *389* (3), 819-825.

5. Ly, N.; Foley, K.; Tao, N., *Anal Chem* **2007,** *79* (6), 2546-2551.

6. Hsieh, H. V.; Stewart, B.; Hauer, P.; Haaland, P.; Campbell, R., *Vaccine* **1998,** *16* (9/10), 997-1003.

7. Iwasaki, Y.; Tobita, T.; Kurihara, K.; Horiuchi, T.; Suzuki, K.; Niwa, O., *Measurement Science and Technology* **2006,** *17* (12), 3184-3188.

8. Schasfoort, R. B. M., *Expert Review of Proteomics* **2004,** *1* (1), 123-132.

9. Lee, K.-H.; Su, Y.-D.; Chen, S.-J.; Tseng, F.-G.; Lee, G.-B., *Biosensors & Bioelectronics* **2007,** *23* (4), 466-472.

10. Georgiadis, R.; Peterlinz, K. P.; Peterson, A. W., *Journal of the American Chemical Society* **2000,** *122* (13), 3166-3173.

11. Lee, H. J.; Goodrich, T. T.; Corn, R. M., *Anal Chem* **2001,** *73* (22), 5525-5531.

12. Lee, H. J.; Wark, A. W.; Corn, R. M., *Langmuir* **2006,** *22* (12), 5241-5250.

13. Heyries, K. A.; Loughran, M. G.; Hoffmann, D.; Homsy, A.; Blum, L. J.; Marquette, C. A., *Biosensors & Bioelectronics* **2008,** *23* (12), 1812-1818.

14. Herrmann, M.; Roy, E.; Veres, T.; Tabrizian, M., *Lab on a chip* **2007,** *7* (11), 1546-52.

15. Brockman, J. M.; Nelson, B. P.; Corn, R. M., *Annual Review of Physical Chemistry* **2000,** *51* (1), 41-63.

16. Liu, J.; Eddings, M. A.; Miles, A. R.; Bukasov, R.; Gale, B. K.; Shumaker-Parry, J. S., *Anal. Chem.* **2009,** *81* (11), 4296-4301.

17. Grant, C. F.; Kanda, V.; Yu, H.; Bundle, D. R.; McDermott, M. T., *Langmuir* **2008,** *24* (24), 14125-14132.

18. Dhayal, M.; Ratner, D. M., *Langmuir* **2009,** *25* (4), 2181-2187.

19. Wegner, G. J.; Wark, A. W.; Lee, H. J.; Codner, E.; Saeki, T.; Fang, S.; Corn, R. M., *Anal. Chem.* **2004,** *76* (19), 5677-5684.

20. Luo, Y.; Yu, F.; Zare, R. N., *Lab on a chip* **2008,** *8* (5), 694-700.

21. Smith, E. A.; Thomas, W. D.; Kiessling, L. L.; Corn, R. M., *Journal of the American Chemical Society* **2003,** *125* (20), 6140-6148.

22. Taylor, J. D.; Linman, M. J.; Wilkop, T.; Cheng, Q., *Anal. Chem.* **2009,** *81* (3), 1146-1153.

23. Natali, M.; Begolo, S.; Carofiglio, T.; Mistura, G., *Lab on a chip* **2008,** *8* (3), 492-494.

24. Whitesides, G. M., *Nature (London, United Kingdom)* **2006,** *442* (7101), 368-373.

25. Sung, W.-C.; Chang, C.-C.; Makamba, H.; Chen, S.-H., *Anal Chem* **2008,** *80* (5), 1529-35.

26. McDonald, J. C.; Whitesides, G. M., *Accounts of Chemical Research* **2002,** *35* (7), 491-499.

27. Tirella, A.; Marano, M.; Vozzi, F.; Ahluwalia, A., *Toxicology in Vitro* **2008,** *22* (8), 1957-1964.

28. Cygan, Z. T.; Cabral, J. T.; Beers, K. L.; Amis, E. J., *Langmuir* **2005,** *21* (8), 3629-3634.

29. Lee, J. N.; Park, C.; Whitesides, G. M., *Anal. Chem.* **2003,** *75* (23), 6544-6554.

30. Wu, T.; Mei, Y.; Cabral, J. T.; Xu, C.; Beers, K. L., *Journal of the American Chemical Society* **2004,** *126* (32), 9880-9881.

31. Cabral, J. T.; Hudson, S. D.; Harrison, C.; Douglas, J. F., *Langmuir* **2004,** *20* (23), 10020-10029.

32. Vogel, B.; Cabral, J. T.; Eidelman, N.; Narasimhan, B.; Mallapragada, S. K., *Journal of Combinatorial Chemistry* **2005,** *7* (6), 921-928.

33. Wu, T.; Mei, Y.; Cabral, J. T.; Xu, C.; Beers, K. L., *Journal of the American Chemical Society* **2004,** *126* (32), 9880-9881.

34. Cramer, N. B.; Scott, J. P.; Bowman, C. N., *Macromolecules* **2002,** *35* (14), 5361-5365.

35. Azzaroni, O.; Mir, M.; Knoll, W., *Journal of Physical Chemistry B* **2007,** *111* (48), 13499-13503.

# CHAPTER 3

# SNAPSHOT DETERMINATION OF dn/dc BY SURFACE PLASMON RESONANCE IMAGING[1]

[1] Sheppard, G. R.; Zhu, T.; Mao, L.; and Locklin, J. To be submitted to *Lab-on-a-Chip.*

**Abstract**

Refractive index increments (dn/dc) are determined by surface plasmon resonance (SPR) imaging. A novel microfluidic linear mixer design is used to generate a controlled concentration gradient of a single sample of water-soluble polymers and proteins. Devices are fabricated by molding poly(dimethylsiloxane) (PDMS) around a photoresist master with micrometer-sized mixing baffles within the channels to induce turbulent back flow. The baffled design completely mixes inlet streams within 1.7 mm at a 1 μL/min flow rate and creates up to 5 new concentrations *in situ*. Polarized, band-pass filtered white light is used to excite surface plasmon resonance within the viewing region in order to accurately track the small refractive index changes generated by the mixer. The dn/dc of water-soluble polymers was determined using the SPRI gradient mixer to within 5 % error from reported literature values. Combining this automated lab-on-a-chip device with a CCD camera has enabled a solitary image to accurately describe dn/dc.

## Introduction

Surface plasmon resonance imaging (SPRI) is a sensing technique that is used to monitor the changes in a dielectric layer at a noble metal interface.[1-7] SPRI was developed from the more commonly utilized surface plasmon resonance (SPR) technique as label-free technique to monitor interfacial binding events.[6, 8, 9] SPR and SPRI use the Kretschmann configuration to match the wave vector of incident photons to the surface plasmons within a noble metal; this has been accomplished using a fixed wavelength light source and an altered the incident angle.[4, 6, 10, 11] The plasmon excitation is observed as a dip in reflectivity due to the absorbance of the photons.[10, 12, 13] Once excited, surface plasmons form an evanescent field on the dielectric side of the metal that decays perpendicular to the noble metal surface and is sensitive to changes within the dielectric medium in contact with the surface.[4, 10, 12, 14] In the case of a binding event, the dielectric layer will increase in thickness as molecules attach to a surface bound moiety, such as in the case of DNA-DNA and protein-analyte interactions.[4-8, 15, 16] These interfacial interactions can be tracked *in situ*, using a 1:1 correlation between the shift in the plasmon curve due to binding and reflectivity on the linear portion of the SPR curve.[4, 6, 7, 13, 17]

SPR Imaging uses a fixed wavelength and incident angle to monitor the shifts in the plasmon curve across a wide surface area by using a CCD camera.[5, 6, 13, 18] This expanded SPR sensing to incorporate array formats for high through put analysis.[9, 12, 16, 17, 19, 20] Parallel tracking of binding events can improve kinetic information by eliminating differences between experimental trials and reduce non-specific binding.[5, 18, 21] Through surface patterning techniques, multiple binding events can be monitored

simultaneously by separately functionalizing different regions of the noble metal surface to determine a range of effects such as non-specific binding, surface packing density, and uniformity.[12, 20, 22-24]

An alternative method to create parallel sensing regions uses microfluidics.[18, 25-29] With predictable fluid dynamics, the laminar flow present in microfluidic channels has been utilized to control reagent delivery to functionalized surfaces.[30-32] By adjusting the design of the microfluidic pattern a variety of devices have been created for a diverse range of applications such as proteomics, micromechanical systems, molecular diagnostics, micro-reactors, and separations.[28, 30, 31, 33-37] The reagent flow rate and channel size can be modified to create the fluid dynamic conditions needed for each of these applications.[31] Incorporation of microfluidic systems with SPR imaging has expanded current microfluidic microscopy methods to monitor *in situ* changes within the channels.[29, 38] By combining these two techniques the miniaturization of array sensors has lead to the production of lab-on-a-chip devices.[20, 26]

Current applications of microfluidic SPRI devices focus on monitoring thickness changes from a binding event.[29, 33] In these cases the refractive index of the bound layer and solvent are assumed to be constant. While in the case of a binding event such assumptions are appropriate, they do not hold true in all sensing applications as a mixture will have a different refractive index from the bulk materials.[39, 40] Such differences have been studied using effective medium approximations, where the refractive index of the mixture is dependent on the index of refraction of each chemical as well as the respective concentrations.[39-41] The refractive index dependence on concentration is well studied in systems that use light to probe things like nanoparticles, proteins, and polymers in

solution to determine hydrodynamic size and shape.[42, 43] The refractive index dependence of the solvent on solute concentration is known as the refractive index increment, dn/dc.[4, 6] For applications like light scattering, gel permeation chromatography, and differential refractometry, dn/dc must be known in order to predict the size and molecular weight of proteins and polymers.[4, 6, 42]

Obtaining dn/dc using a single SPR image will require the creation of different concentrations *in situ*. Concentration gradients in microfluidic devices are created through one of two methods, diffusion or convection.[30, 32, 44] Diffusion mixing has been shown to occur in laminar flow systems when a solvent channel is combined with a solution channel, however, this method of mixing takes time and long channel lengths.[44, 45] Alternatively, the design of the microfluidic channels can be altered to induce convective mixing.[32, 46-49] A variety of microfluidic mixer designs can be found in the literature.[16, 30, 31, 36, 50-52] The most straightforward designs utilize a T-junction followed by a serpentine pattern to provide a path-length long enough to mix two streams in the shortest amount of lateral distance.[44, 45, 53] Such devices are easily designed, however, their size remains a factor when trying to scale a device onto an SPRI viewing area of ~2 $cm^2$. In order to increase mixing rates, a form of convective mixing needs to be induced through alternating flow directions with the channels by continuously separating and recombining channels.[31, 32, 47, 49] While these designs work for certain applications, they can require complex microfluidic fabrication methods and long distances before complete mixing occurs. Adding structures within the microfluidic channel to induce alternating flow patterns along the channel yields rapid mixing.

In this paper, a microfluidic device was designed to generate a linear concentration gradient from which the refractive index increment was measured by SPRI. Our design for the linear mixer incorporates a series of baffles that create back flow currents along the channels. The baffles were designed on the walls of the channels in order to take advantage of rapid fabrication methods and to keep the bottom of the channel clear for SPR sensing. Through subsequent channel division and recombination of opposing streams a linear concentration gradient is created.[49] Attaching the linear mixer to an SPR substrate, the changes in the refractive index due to the formation of the concentration gradient can be observed using pictures taken by the SPRI's camera.

## Experimental

### Materials

All chemicals were used as received unless noted otherwise. SU-8 2025 photoresist and developer were purchased from MicroChem. Trimethylchlorosilane was purchased from Alfa Aesar. Silicon wafers with <100> orientation (native oxide) were purchased from University Wafer. PDMS was created using a silicone elastomer kit (SYLGARD 184, Dow Corning). Gold (99.999 %), silver (99.999 %) and titanium (99.99 %) were purchased from Kurt J. Lesker. High refractive index (RI) glass and prisms (SF10, n = 1.72) were purchased from Esco Products, Inc. Microfluidic masks were designed on AutoCAD (Autodesk, Inc., San Rafael, CA) and printed on transparencies at 20000 dpi by CAD/Art Services, Inc. (Bandon, OR).

**Lithographic Methodology**

Microfluidic master molds were created on silicon wafers using a mask aligner (MA6, Karl Suss). Negative photoresist, SU-8 2025, (~ 4 mL) was spun coated onto a clean, dry wafer at 3000 rpms for 30 seconds. The photoresist was then exposed through a mask to UV light ($\lambda$ = 365 nm) at 20 mW/cm$^2$. The wafer was then heat cured and washed with SU-8 developer for 30 min under constant agitation. Wafers were rinsed with isopropanol and dried before a final curing on a hot plate at 70 °C for 10 min.

Microfluidic devices were molded out of PDMS using a 10:1 SYLGARD mixture of the base to curing agent. The mixture was degassed before pouring over the master wafer. The PDMS was cured in an oven for 4 hrs at 70 °C. Pre-coating the wafers with trimethylchlorosilane by vapor deposition ensured that the PDMS could be easily removed after curing. The PDMS was oxygen plasma cleaned (Harrick Plasma, 18 W, 0.8 mbar) prior to sealing onto a SPR substrate.

**Generation and Treatment of SPR Substrates**

SPR substrates are comprised of high refractive index glass (SF10, RI of 1.72 at $\lambda$ = 632.8 nm) with a noble metal coating. Metal was deposited onto the glass using electron beam deposition. A 47 nm gold or silver layer was deposited at 0.5 Å/s on top of a 3 nm Ti adhesive layer using an electron beam deposition system (Kurt J. Lesker). Gold-coated SPR substrates were then coated with a 20 nm layer of silicon oxide using Ar plasma sputtering at a 0.5 Å/s rate and 50 W. Silver substrates were Ar plasma cleaned (Harrick Plasma, 18 W, 0.8 mbar) for 5 min before attaching the PDMS microfluidic mold. Silicon oxide coated gold substrates were oxygen plasma cleaned under identical conditions as the silver.

## Characterization

Thickness of the master mold used in soft-lithographic fabrication was determined by profilometry using a Dektak 150 with a 3 mm radius stylus. Microscope images were taken using a Zeiss microscope with a green fluorescent filter set (41001 FITC, Chroma Technology Corp., Rockingham, VT, USA). Surface plasmon resonance imaging was performed on a SPRImager II (GWC Technologies, Madison, MI) with a white light source, an 800 nm narrow band pass filter, polarizer, and a CCD camera. Angular surface plasmon resonance curves were taken using a Multiskop (Optrel GbR) in a custom flow cell. Analysis of angular SPR curves was performed on Winspall (v. 3.01).

## Fabrication of SPRI Microfluidic Devices

SPRI microfluidic devices were fabricated using soft-lithography to form the channels by molding an elastomeric polymer over a master mold.[54] Soft-lithography production of microfluidics utilizes poly(dimethylsiloxane) (PDMS) as the elastomer due to its ease of fabrication, rapid prototyping, and accurate transfer of sub-micron features from the inverse template.[30, 54] Master molds were created using photolithography which is commonly used to transfer microfluidic patterns from a printable mask into a photo-reactive polymer layer of finite thickness. The thickness of the polymer defines the depth of the microfluidic channels when the PDMS is cured over the master mold.

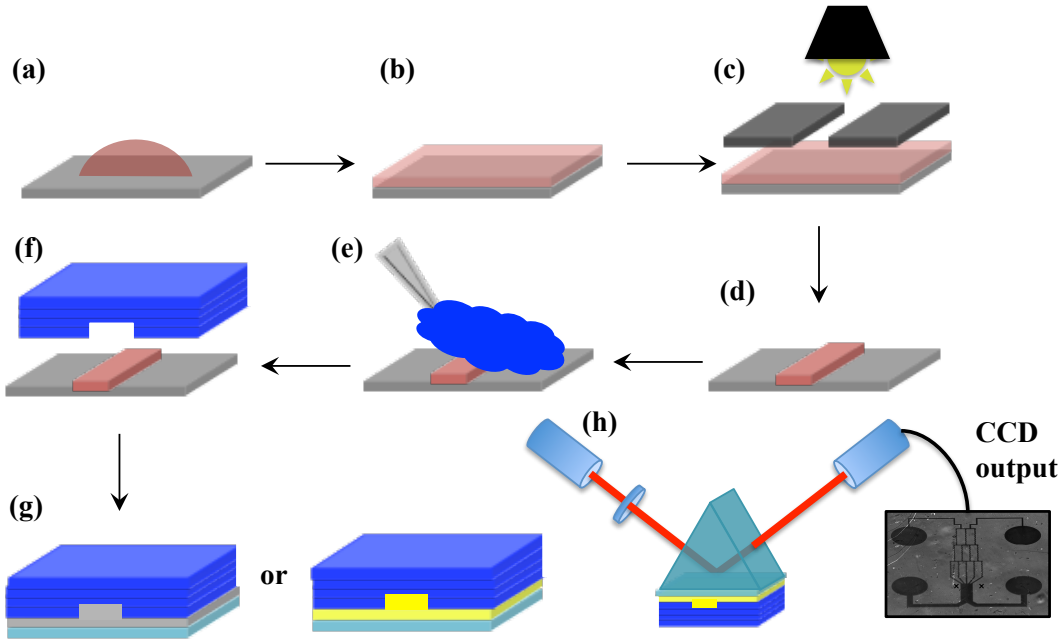


**Figure 3.1.** Fabrication of the linear mixer microfluidic device. (a-d) Master molds were created using photolithography. (e-f) Microfluidic devices were then created out of PDMS molding. (g) Devices were sealed against SPR substrates and (h) coupled to a prism for SPR imaging analysis.

In order to create the master mold, a negative photoresist (SU-8 2025, MicroChem) was deposited onto a clean, dry silicon wafer, Figure 3.1a. Spin coating uniformly spread the photoresist over the wafer, which ensures that the photoresist has the same height profile throughout, Figure 3.1b. Height variances can induce unwanted fluid dynamics effects that can disrupt the mixing capabilities of the device. The wafer was transferred to a mask aligner (MA6, Karl Suss) to use UV light to transfer the microfluidic design from a photo-mask into the photoresist. The linear mixer pattern was

designed on AutoCAD and was created to fit within a 2 $cm^2$ area by using channels with a 100 μm width. The microfluidic design was printed onto transparencies at 20000 dpi by CAD Art Services, Inc. (Bandon, OR). The high-resolution printing is required to accurately transfer the micron-sized features from the microfluidic design into the mask and reduces the amount of UV bleed through found in lower resolution printing. As a negative photoresist, when SU-8 is exposed to UV light the areas where the mask allows the light to pass through will polymerize, Figure 3.1c. The pattern was accurately transferred to the photoresist using a soft-contact method to reduce the amount of UV scattering that occurs at the patterns edges. This creates uniform, sharp edges within the photo-cured SU-8, Figure 3.1d. With uniform, vertical walls the baffles within the microfluidic channels will perform as designed while non-uniform transfer will alter the fluid dynamics reducing the effectiveness of the baffles to mix the solution. After UV exposure, the photo-cured SU-8 is solvent resistant while the unexposed photoresist can be removed by dissolving it in SU-8 photo-developer. Developed master molds were characterized by profilometry to confirm uniformity of the SU-8 thickness. An average thickness of 29 ± 0.4 μm was measured and was consistent throughout multiple molds. With such a reproducible master mold, each microfluidic device will exhibit similar fluid mixing.

As a negative photoresist, SU-8 forms a master mold that has raised features from which the microfluidic channels are formed when transferred into an elastomer such as PDMS. The PDMS was prepared by mixing the components of a SYLGARD silicone elastomer kit and was poured over the master mold, Figure 3.1e. After curing, the PDMS is a flexible, positive mold with well-defined microfluidic channels, Figure 3.1f. Inlet

and outlet holes for the fluid delivery system were created using a biopsy punch. Attachment of the PDMS mold to SPRI substrates and microscope slides was performed by plasma cleaning all surfaces, Figure 3.1g. Plasma cleaning of the PDMS exposes hydroxyl groups that improve adhesion to other oxide surfaces. This bonding procedure was used to attach the PDMS to the microscope slides and silicon oxide coated gold SPR substrates. Gold substrates are commonly used for SPR sensing applications because it is a stable metal with known reactivity with thiols. The excitation of the surface plasmon resonance in gold can be accomplished using light within the visible spectral range. While gold is more commonly used for SPR sensing, however, silver has been shown to produce sharper plasmon dips, increasing sensitivity when monitoring minute changes at the interface. Microfluidic PDMS molds were attached to silver SPR substrates without the use of a silicon oxide layer with similar adhesion strengths as with oxide coated gold surfaces. While gold is an inert metal and does not readily bond with the PDMS, silver has been speculated to react with oxygen to form a silver oxide layer. It is speculated that a thin silver oxide layer formed when the clean silver surface is attached to the exposed hydroxyls on the PDMS improving the adhesion. Once combined the adhesion between the PDMS and SPRI substrates was stable for several days.

The microfluidic coupled SPR substrates were then setup in the SPR Imager using a custom holder and an equilateral SF10 prism (RI of 1.72 at $\lambda$ = 632.8 nm), Figure 3.1h. The higher refractive index glass and angle of the prism allows for SPR excitation in an angular range for *in situ* reflectivity tracking. The SPRI uses a white light source with an 800 nm band-pass filter to excite surface polaritons. The CCD output image in Figure 3.1h represents a typical SPR image from a linear mixer device with all the channels in a

single snapshot. As the fluid is passed through the device any changes in refractive index can be monitored at any point within the device.

**Results and Discussion**

The baffles within the microfluidic channels will provide the back flow conditions needed to induce mixing, however, the flow rate of the solutions can be adjusted to improve the mixing conditions. At high flow rates the solution does not effectively mix due to increased inertial forces, which result in laminar flow even in the presence of the baffled sides. Lowering the flow rate reduces the inertial force allowing for the solution to mix. The dominate mixing method within a microfluidic channel can be described by the Péclet number which is a dimensionless number that describes the ratio of convective to diffusive forces.[31, 47] The Péclet number is calculated as $Pe = U_o w/D$ where $U_o$ is the characteristic velocity, $w$ is the channel width, and $D$ is the diffusion constant of the analyte.

Velocity fields corresponding to device geometry used in our experiments were computed via a 2D Navier-Stokes solver, and concentration profiles were computed via a 2D Convection-Diffusion solver in COMSOL Multiphysics to estimate the optimal flow rate required to induce mixing and to create complete mixing along the 2 mm channel length. A simulated concentration profile of the mixing is shown in Figure 3.2a, where blue and red inlets on are on the left of the image. Mixing occurs within the stream as indicated by the change in the concentration profile color scheme. The simulated fluid's characteristic velocity was 0.004 m/s, which taking the median cross section area indicates a flow rate of ~1 μL/min. To experimentally confirm the optimal flow rate, a microfluidic device was attached to a microscope slide (RI of 1.5151 at λ = 632.8 nm)

and fluorescein salt solution in water was flown through the linear mixer. A fluorescent microscope was used to image the mixing profiles within the microfluidic channels. At a flow rate of 1 μL/min, the two streams were completely mixed at a distance of ~1.7 mm down each baffled channel, Figure 3.2b. For fluorescein the diffusion constant has previously been determined to be 2 x $10^{-6}$ $cm^2/s$.[45] At the optimal characteristic velocity and fluorescein as a model system, the Péclet number would be 2000 which indicates that for a diffusion controlled mixing the length of the channel would have to 2000 times the width, or 200 mm. With a shorter lateral distance for mixing to be complete than the diffusive mixing within a straight channel, we can conclude that the baffles are inducing the mixing within the microfluidic channels.

The flow rate was established for fluorescein, however, the same characteristic velocity can be used to mix polymer solutions. Polymer molecules, with much higher molecular weights than fluorescein, will have a lower diffusion constant due to a higher hydrodynamic radius. Such an example would be poly(ethylene glycol) (PEG) which has been shown to have a diffusion constant on the order of $10^{-7}$ $cm^2/s$ with a molecular weight of 20,000 g/mol.[55] As the formula for the Péclet number indicates, an order of magnitude decrease in the diffusion constant increases the Pe value by the same magnitude. The larger the Pe value the longer the channel needs to be in order for diffusion mixing to occur. For a 450 repeat unit PEG, diffusion controlled mixing will require a 2 m long channel for complete mixing to occur.

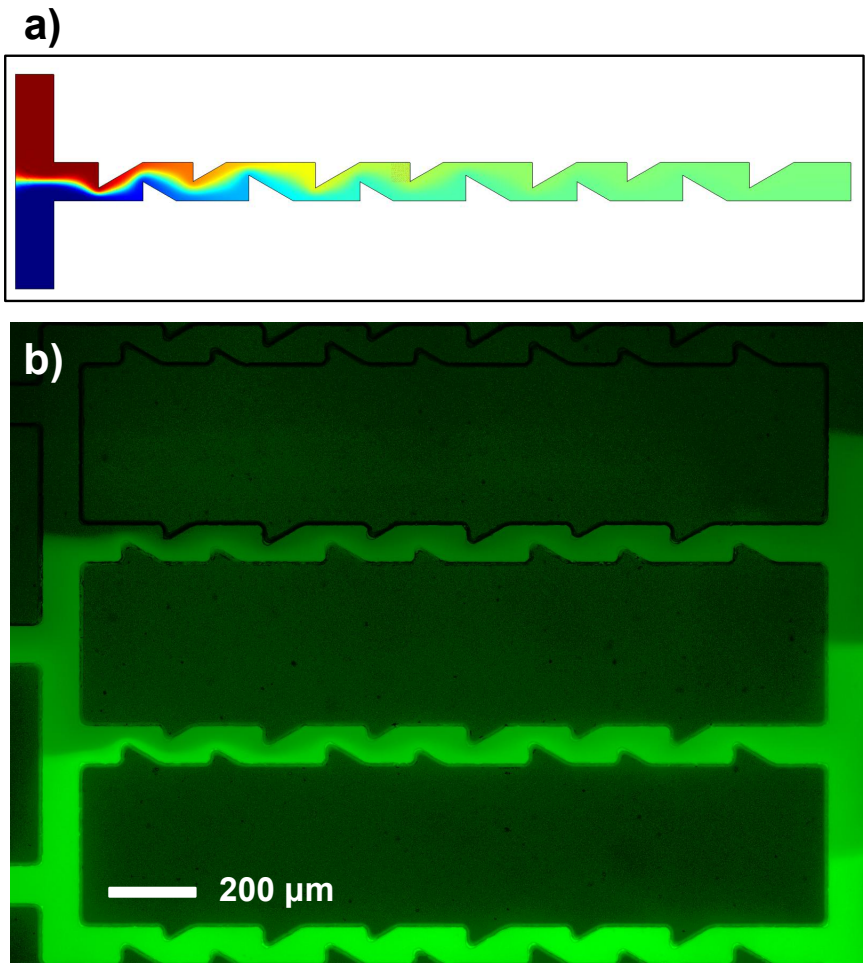


**Figure 3.2.** Depiction of the baffle induced mixing within the microfluidic channels. a) COMSOL simulation of the mixing that occurs within the channels. b) Fluorescent microscope image using fluorescein sodium salt solution (green).

Microfluidic linear mixer PDMS molds were attached to SPR substrates in order to monitor the refractive index changes of polymer solutions. The adhesion between the gold and PDMS has been shown to be poor due to weak interaction between the exposed siloxane groups from the PDMS with the inert gold. This can cause the PDMS to delaminate during SPRI tracking, resulting in device failure. In order to improve the

adhesion, a 10 nm $SiO_2$ layer was deposited on top of the gold substrates. Silver substrates exhibited sufficiently strong adhesion with PDMS molds without an oxide layer. Both noble metals, gold and silver, can be used to excite surface plasmon resonance with similar responses to refractive index changes of the dielectric in contact with the metal interface. The width and depth of the reflectivity curve is dependent on the refractive index and thickness of the metal layer. Reflectivity curves of silicon oxide coated gold and silver SPR substrates are shown in the Figure 3.3a along with model data to determine the thickness of each layer. The reflectivity curve for silver (black) is narrower and has a larger slope away from the plasmon dip angle while the gold substrate (red) has a broader plasmon dip than silver with a minimum in the reflectivity curve that is at a higher incident angle. The sharper the plasmon the more sensitive the tracking at a fixed incident angle, however, the broader the plasmon the larger the window in which changes can be determined.

In order to track the shift in the plasmon angle over time the incident angle must be held constant. The criterion for the tracking angle depends on the change in the dielectric medium such as increase in refractive index or thickness. For the linear mixing applications, the refractive index of the solvent will increase as the concentration of solute is elevated shifting the plasmon to the right, Figure 3.3b. In order to track the plasmon shift to higher incident angles, an incident angle on the linear portion of the reflectivity curve is chosen to the left of the plasmon dip. Using the linear portion of the curve allows for a 1:1 conversion of changes in reflectivity due to increasing refractive index. Monitoring angles outside the linear region will result in a non-linear relationship between reflectivity and refractive index.

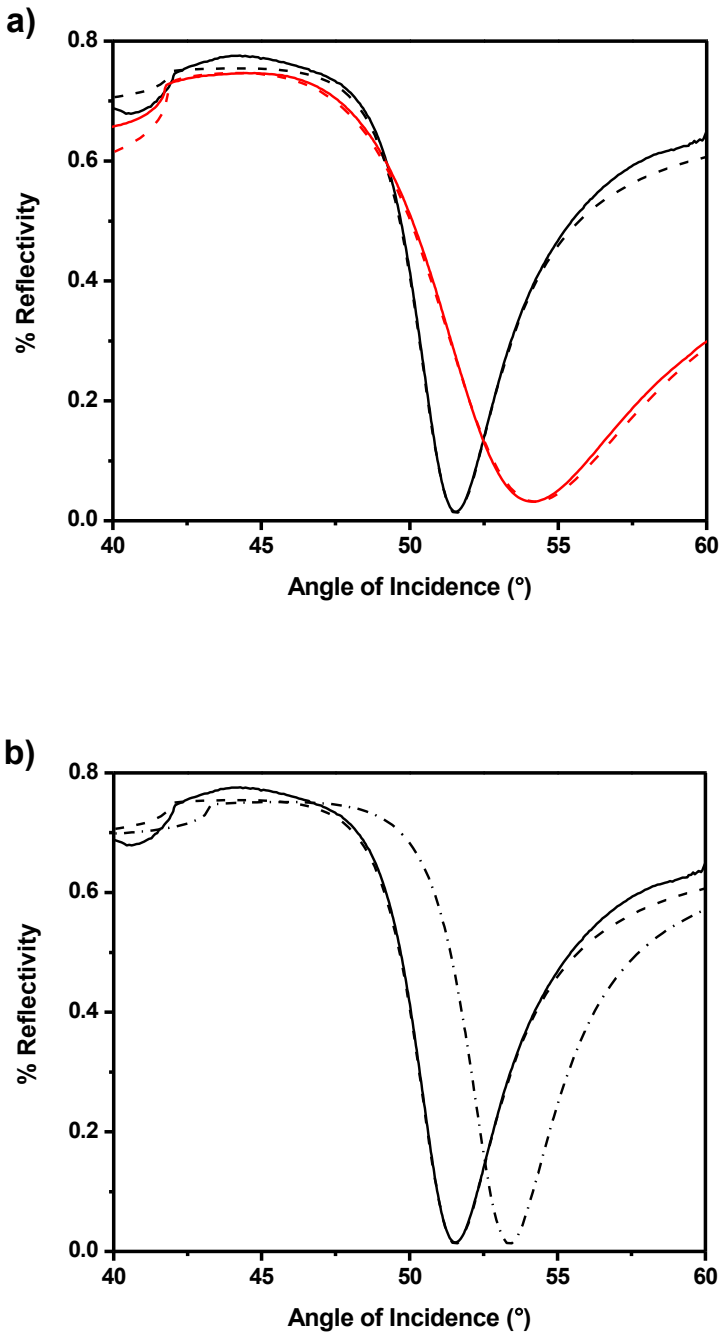


**Figure 3.3.** a) Reflectivity curves of silver (black) and gold (red) SPRI substrates. Dashed lines were fit using Winspall to determine the thickness of the metal. b) Maximum plasmon shift due to an increase in solvent refractive index by increasing solute concentration.

While larger refractive indices can be monitored using angular SPR scans, the reflectivity tracking method is limited to plasmon shifts equivalent to the angular difference in the linear portion of the curve. The maximum shift in the experimentally measured silver SPR substrate is shown in Figure 3.3b as indicated by the dashed lines. The reflectivity data was fit in Winspall (dashed fit line) to determine the refractive index and thickness of the silver film with ethanol (RI of 1.360 at $\lambda$ = 632.8 nm) as the solvent. The refractive index of the dielectric was then increased to until the linear portion of the curves no longer overlapped at a refractive index value of 1.376 at $\lambda$ = 632.8 nm.

In order to determine maximum refractive index increment, dn/dc, that can be measured by SPRI the shift of the plasmon dip must be within the range of the linear portion of the curve. For the silver film in Figure 3.3b, the 1:1 reflectivity-incident angle relationship will hold for 2.15° shift while the gold SPR substrate in Figure 3.3a, has a broader angular range of 3.8° with a maximum refractive index of 1.390 at $\lambda$ = 632.8 nm. The angular shift due to refractive index exhibits a linear relationship and can be expressed as $dn/d\theta$, which has a value of 0.0218 /° for the silver and 0.0196 /° for gold. With a predictable angular dependence on refractive index, the angular shift due to concentration $d\theta/dc$ can be determined from $dn/d\theta$ and dn/dc. With most polymer-solvent mixtures the refractive index increment is $\leq$ 0.15 mL/g.[56] While angular dependence on solution concentration will vary between samples the largest shifts will occur with the larger refractive index increment. Using a dn/dc of 0.15 mL/g, the $d\theta/dc$ is 6.88 ° $(g/mL)^{-1}$ and 7.65 ° $(g/mL)^{-1}$ for silver and gold, respectively. From this ratio the maximum concentration that can be monitored from a fixed angle can be determined. The available concentration range that can be monitored is 0.313 g/mL for silver and

0.497 g/mL for gold. These ranges were computed based on a measurement from a HeNe laser ($\lambda$ = 632.8 nm) rather than the 800 nm light used by the SPRI. Adjusting the plasmon fits in Winspall for the different light source does not affect the $dn/d\theta$ value for the silver or gold substrates, however, the plasmon dips broaden to increasing the linear portion of the reflectivity curve for both metals. With angular ranges of 2.5° and 4.0° for silver and gold, respectively, the theoretical maximum concentration for detection will be 0.363 g/mL and 0.523 g/mL. Using concentrations below these limits will ensure that the microfluidic linear mixer will be able to monitor the reflectivity and directly correlate it to the refractive index of the mixtures.

SPRI uses a white light with an 800 nm band-pass filter source and a 2 cm diameter circular beam to excite surface plasmons across the surface of the noble metal coated substrate. Software accompanying the SPR Imager converts the pixel values into reflectivity units for selected regions of interest within the image. An image of the microfluidic linear mixer design as well as an SPR image is shown in Figure 3.4. The SPR image depicts the three stage linear mixer with 50 mg/mL of PEG in water. False color was added to the image in order to better visualize the contrast between the solvated channels (black) and the PDMS master mold (blue). While plasmons are generated across the entire surface, the incident angle was tuned to pick up the plasmon dip associated with the solvated channels. The SPR Imager uses low pixel values, represented as black in Figure 3.4b, to denote a decrease in reflectivity. The reflectivity can be tracked *in situ* using the V++ software associated with the SPR Imager. Using the real time monitoring feature, the angle of incidence was tuned so that the solvent stream

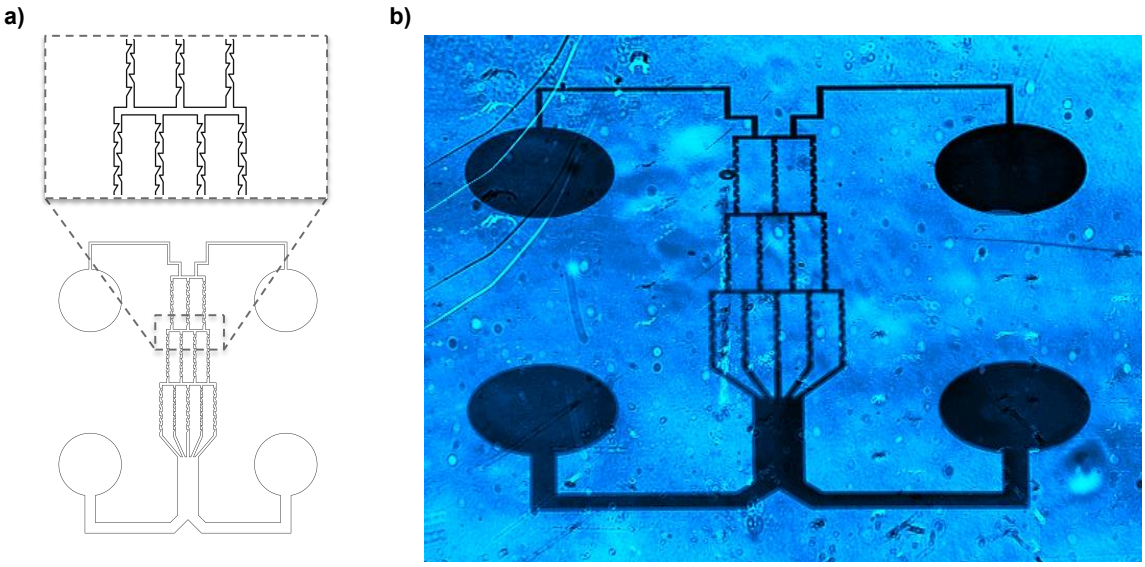


**Figure 3.4.** a) Microfluidic linear mixer design as replicated from AutoCAD. b) SPRI image of the linear mixer patter with 50 mg/mL PEG in water. False color was added to the image for visualization purposes.

(right side) had the lowest pixel value and appears as the darkest regions. As the plasmon dip shifts to higher angles of incident with increasing polymer concentration, the static angle image will become lighter where the PEG solution has mixed. The change in pixel intensity in the channels can then be correlated to the refractive index of the solution.

The linear mixer uses three stages to separate and mix the two inlet streams at the top of Figure 3.4a. A $4^{th}$ stage combines the outlet streams from stage three into a broad channel which was used for direct SPRI viewing of the linear change in reflectivity. The combination of the separate flow streams with different concentrations can be visually observed by the fluorescent image in Figure 3.5a. Extracting the pixel intensity values from the SPR image will provide the reflectivity data to determine the refractive index

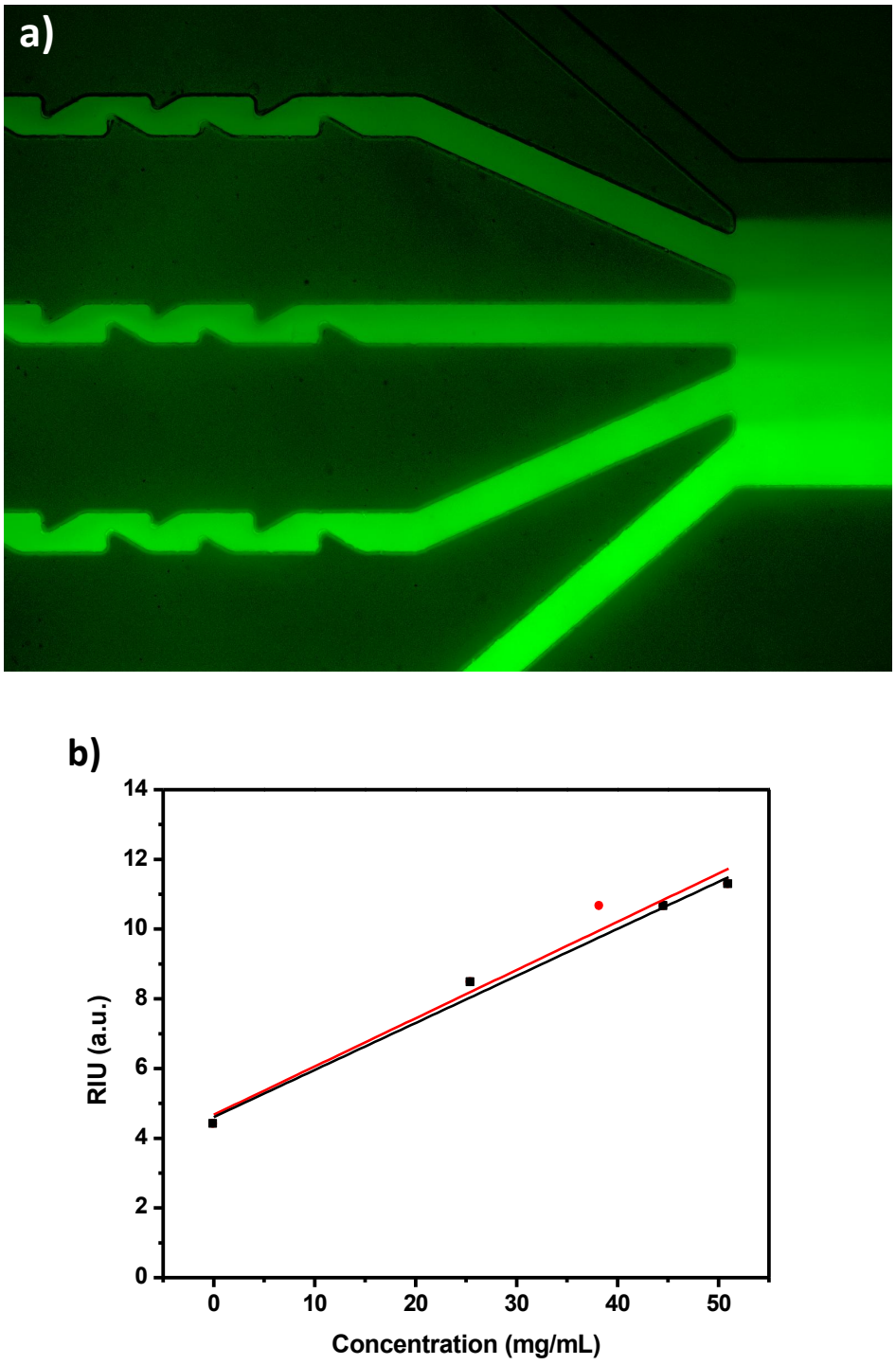


**Figure 3.5.** a) Fluorescent microscope image of stage 3 and SPRI viewing region of the microfluidic device. b) SPRI pixel values taken from the SPRI viewing region of the linear mixer with PEG in water.

increment. Data in Figure 3.5b was taken from pixel values at the end of the third stage of a PEG in water mixture. While the third stage has 5 mixing channels, one of the data points was excluded from the linear line due to a bubble within the channel that prevented complete mixing. Removal of this data point reduces the five channels to a device that only effectively produces two new concentrations. However, expanding the analysis to include the other mixing channels produces a maximum eight different concentrations. Denoting the device's inlet concentrations as $I_1$ for water and $I_2$ for polymer solution, the first stage mixes the inlet streams to produce a concentration $^1/_2$ $I_2$. The streams that are on the outside of each stage maintain the concentration from the inlets. The second stage produces concentrations that are $^1/_4$ and $^3/_4$ of $I_2$ while the last stage has $^1/_8$, $^1/_2$, and $^7/_8$ of $I_2$. The concentration profile of the mixer accounts for the data point spacing observed in Figure 3.5b. By adding the pixel values from the channels with different concentration the linear relationship between the refractive index and concentration can be correlated with improved certainty. The refractive index increment of the 50 mg/mL PEG solution with all the channels was determined to be 0.138 mL/g. With a literature value of 0.134 mL/g,[56] the refractive index increment taken from the SPRI measurement matches within a 3.0 % difference.

The accuracy of the fixed angle reflectivity tracking of the SPRI was confirmed with angular SPR measurements at $\lambda$ = 632.8 nm. SPR was used by Tumolo *et al*. to determine refractive index increments of several biological molecules.[42] Using the Kretschmann configuration and a custom flow cell with a silver SPR substrate, the dn/dc value from serial dilutions of 50 mg/mL PEG was measured, Figure 3.6. The flow cell was rinsed with solvent after each measurement to prevent sample mixing. An angular

scan of water before and after the injections, black solid and dashed lines, respectively, ensured that the polymer was not adhering to the silver. The concentrations for the dilutions were chosen to mimic the concentration profile produced by the linear mixer with highest concentration represented as the red line. The shift in the plasmon dip angle matched the dispersion of the SPR image data. Modeling the data with Winspall produced a refractive index increment value of 0.137 mL/g, which is 2.2 % different from the literature value for PEG.[56]

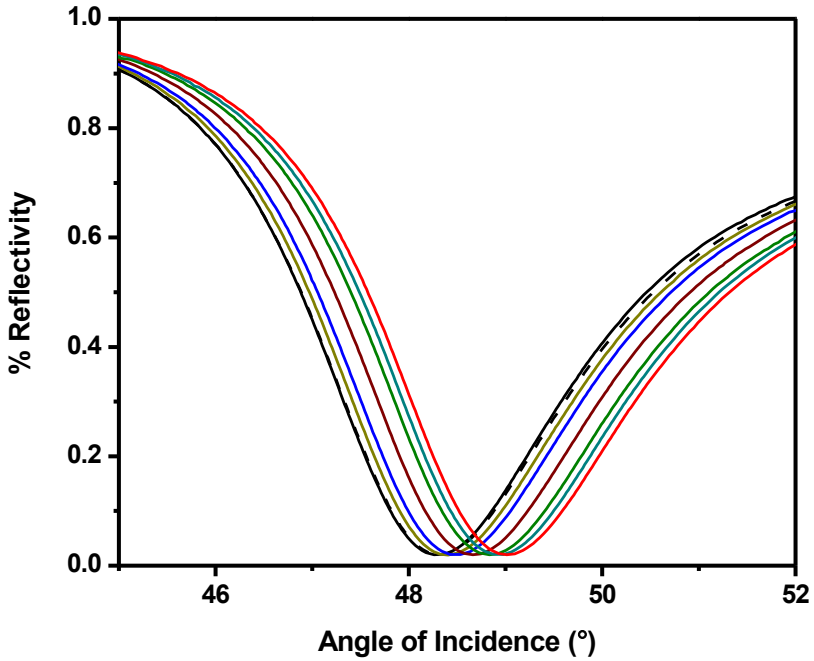


**Figure 3.6.** SPR angular shift due to serial dilution of PEG in water. Black lines represent the plasmon curves with water before (solid) and after (after) the PEG measurements. Concentrations for the dilution were adopted from those produced by the linear mixer microfluidic device with a 50 mg/mL PEG solution as the red line.

The angular SPR measurement uses multiple injections from previously prepared dilutions and requires a series of data modeling and conversions to determine dn/dc. Alternatively, the microfluidic SPRI method requires a single sample to determine a polymer's dn/dc from the slope of the reflectivity data. While *in situ* tracking with the SPRI is possible, the refractive index increment can be determined using individual snapshots of each solute. The linear gradient microfluidic design was applied to other water soluble polymers to determine the refractive index increment of Jeffamine M600 and poly(vinyl alcohol). Analysis of the SPR images produced dn/dc values of 0.038 mL/g and 0.031 mL/g, respectively. Using this technique, polymers with mixed monomers or newly developed polymers having unknown refractive index increments can be rapidly analyzed to improve other characterization techniques.

## Conclusions

Refractive index increments have been determined from a single image by incorporating a linear gradient microfluidic mixer design with SPRI. Introducing baffle structures into microfluidic channels produced controlled mixing of solutions within 1.7 mm at a 1 μL/min flow rate. The three-stage, linear concentration gradient design produced up to 5 concentrations in situ to determine dn/dc with less than 3 % error from reported values. With 2.5° and 4.0° angular scanning windows for silver and gold, respectively, samples with concentrations up to 0.363 g/mL and 0.523 g/mL can be used for dn/dc studies. This method of determining dn/dc can be used to quickly characterize refractive index dependence on concentration of samples that have not been previously studied. Utilizing this method in conjunction with other analytical techniques can improve the understanding of certain macromolecular properties like molecular weight and hydrodynamic radius.

## References


1. Smith, E. A.; Thomas, W. D.; Kiessling, L. L.; Corn, R. M., *J. Am. Chem. Soc.* **2003,** *125* (20), 6140-6148.

2. Brockman, J. M.; Nelson, B. P.; Corn, R. M., *Annu. Rev. Phys. Chem.* **2000,** *51* (1), 41-63.

3. Boozer, C.; Kim, G.; Cong, S.; Guan, H.; Londergan, T., *Curr. Opin. Biotechnol.* **2006,** *17* (4), 400-405.

4. Homola, J., *Chem. Rev.* **2008,** *108* (2), 462-493.

5. Scarano, S.; Mascini, M.; Turner, A. P. F.; Minunni, M., *Biosens. Bioelectron.* **2010,** *25* (5), 957-966.

6. Campbell, C. T.; Kim, G., *Biomaterials* **2007,** *28* (15), 2380-2392.

7. Lee, H. J.; Wark, A. W.; Corn, R. M., *Langmuir* **2006,** *22* (12), 5241-5250.

8. Jordan, C. E.; Frutos, A. G.; Thiel, A. J.; Corn, R. M., *Anal. Chem.* **1997,** *69* (24), 4939-4947.

9. Smith, E. A.; Erickson, M. G.; Ulijasz, A. T.; Weisblum, B.; Corn, R. M., *Langmuir* **2002,** *19* (5), 1486-1492.

10. Knoll, W., *Annu. Rev. Phys. Chem.* **1998,** *49* (1), 569-638.

11. Mayer, K. M.; Hafner, J. H., *Chem. Rev.* **2011,** *111* (6), 3828-3857.

12. Chen, Y.; Nguyen, A.; Niu, L.; Corn, R. M., *Langmuir* **2009,** *25* (9), 5054-5060.

13. Jordan, C. E.; Corn, R. M., *Anal. Chem.* **1997,** *69* (7), 1449-1456.

14. Murray, W. A.; Auguié, B.; Barnes, W. L., *The Journal of Physical Chemistry C* **2009,** *113* (13), 5120-5125.

15. Yuk, J. S.; Jung, J.-W.; Hyun, J.; Kim, Y.-M.; Ha, K.-S., *Sensors and Actuators B: Chemical* **2008,** *131* (1), 241-246.

16. Brockman, J. M.; Frutos, A. G.; Corn, R. M., *J. Am. Chem. Soc.* **1999,** *121* (35), 8044-8051.

17. Hook, A. L.; Thissen, H.; Voelcker, N. H., *Langmuir* **2009,** *25* (16), 9173-9181.

18. Luo, Y.; Yu, F.; Zare, R. N., *Lab on a Chip* **2008,** *8* (5), 694-700.

19. Liu, J.; Eddings, M. A.; Miles, A. R.; Bukasov, R.; Gale, B. K.; Shumaker-Parry, J. S., *Anal. Chem.* **2009,** *81* (11), 4296-4301.

20. Lee, H. J.; Wark, A. W.; Corn, R. M., *Analyst* **2008,** *133* (8), 975-983.

21. Ladd, J.; Taylor, A. D.; Piliarik, M.; Homola, J.; Jiang, S., *Anal. Chem.* **2008,** *80* (11), 4231-4236.

22. Kato, K.; Ishimuro, T.; Arima, Y.; Hirata, I.; Iwata, H., *Anal. Chem.* **2007,** *79* (22), 8616-8623.

23. Dhayal, M.; Ratner, D. M., *Langmuir* **2009,** *25* (4), 2181-2187.

24. Foley, J. O.; Fu, E.; Gamble, L. J.; Yager, P., *Langmuir* **2008,** *24* (7), 3628-3635.

25. Taylor, J. D.; Linman, M. J.; Wilkop, T.; Cheng, Q., *Anal. Chem.* **2009,** *81* (3), 1146-1153.

26. Ouellet, E.; Lausted, C.; Lin, T.; Yang, C. W. T.; Hood, L.; Lagally, E. T., *Lab on a Chip* **2010,** *10* (5), 581-588.

27. Wang, Z.; Wilkop, T.; Xu, D.; Dong, Y.; Ma, G.; Cheng, Q., *Analytical and Bioanalytical Chemistry* **2007,** *389* (3), 819-825.

28. Dong, Y.; Wilkop, T.; Xu, D.; Wang, Z.; Cheng, Q., *Analytical and Bioanalytical Chemistry* **2008,** *390* (6), 1575-1583.

29. Lee, H. J.; Goodrich, T. T.; Corn, R. M., *Anal. Chem.* **2001,** *73* (22), 5525-5531.

30. Sia, S. K.; Whitesides, G. M., *ELECTROPHORESIS* **2003,** *24* (21), 3563-3576.

31. Squires, T. M.; Quake, S. R., *Reviews of Modern Physics* **2005,** *77* (3), 977-1026.

32. Di Carlo, D., *Lab on a Chip* **2009,** *9* (21), 3038-3046.

33. Ly, N.; Foley, K.; Tao, N., *Anal. Chem.* **2007,** *79* (6), 2546-2551.

34. Wu, T.; Mei, Y.; Cabral, J. o. T.; Xu, C.; Beers, K. L., *J. Am. Chem. Soc.* **2004,** *126* (32), 9880-9881.

35. Chen, D. L.; Gerdts, C. J.; Ismagilov, R. F., *J. Am. Chem. Soc.* **2005,** *127* (27), 9672-9673.

36. Cygan, Z. T.; Cabral, J. T.; Beers, K. L.; Amis, E. J., *Langmuir* **2005,** *21* (8), 3629-3634.

37. Zhang, C.; Xu, J.; Ma, W.; Zheng, W., *Biotechnol. Adv.* **2006,** *24* (3), 243-284.

38. Sheppard, G.; Oseki, T.; Baba, A.; Patton, D.; Kaneko, F.; Mao, L.; Locklin, J., *Biomicrofluidics* **2011,** *5* (2), 026501-6.

39. Heller, W., *The Journal of Physical Chemistry* **1965,** *69* (4), 1123-1129.

40. Mallet, P.; Guérin, C. A.; Sentenac, A., *Physical Review B* **2005,** *72* (1), 014205.

41. Ruppin, R., *Optics Communications* **2000,** *182* (4-6), 273-279.

42. Tumolo, T.; Angnes, L.; Baptista, M. S., *Anal. Biochem.* **2004,** *333* (2), 273-279.

43. Homola, J.; Piliarik, M., Surface Plasmon Resonance (SPR) Sensors. Homola, J., Ed. Springer Berlin Heidelberg: 2006; Vol. 4, pp 45-67.

44. Kamholz, A. E.; Weigl, B. H.; Finlayson, B. A.; Yager, P., *Anal. Chem.* **1999,** *71* (23), 5340-5347.

45. Culbertson, C. T.; Jacobson, S. C.; Michael Ramsey, J., *Talanta* **2002,** *56* (2), 365-373.

46. Stroock, A. D.; Dertinger, S. K.; Whitesides, G. M.; Ajdari, A., *Anal. Chem.* **2002,** *74* (20), 5306-5312.

47. Mengeaud, V.; Josserand, J.; Girault, H. H., *Anal. Chem.* **2002,** *74* (16), 4279-4286.

48. Xia, H. M.; Wang, Z. P.; Koh, Y. X.; May, K. T., *Lab on a Chip* **2010,** *10* (13), 1712-1716.

49. Kim, C.; Lee, K.; Kim, J. H.; Shin, K. S.; Lee, K.-J.; Kim, T. S.; Kang, J. Y., *Lab on a Chip* **2008,** *8* (3), 473-479.

50. Harnett, C. K.; Templeton, J.; Dunphy-Guzman, K. A.; Senousy, Y. M.; Kanouff, M. P., *Lab on a Chip* **2008,** *8* (4), 565-572.

51. Song, H.; Chen, D. L.; Ismagilov, R. F., *Angew. Chem. Int. Ed.* **2006,** *45* (44), 7336-7356.

52. Groisman, A.; Quake, S. R., *Phys. Rev. Lett.* **2004,** *92* (9), 094501.

53. Nelson, K. E.; Foley, J. O.; Yager, P., *Anal. Chem.* **2007,** *79* (10), 3542-3548.

54. McDonald, J. C.; Whitesides, G. M., *Acc. Chem. Res.* **2002,** *35* (7), 491-499.

55. López-Esparza, R.; Guedeau-Boudeville, M. A.; Gambin, Y.; Rodríguez-Beas, C.; Maldonado, A.; Urbach, W., *J. Colloid Interface Sci.* **2006,** *300* (1), 105-110.

56. Theisen, A.; Johann, C.; Deacon, M. P.; Harding, S. E., *Refractive Increment Data-Book for Polymer and Biomolecular Scientist*. Nottingham Unversity Press: 2000.

# CHAPTER 4

# MOLECULAR IMRPTINGING ON BLU-RAY DISCS: AN INEXPENSIVE APPROACH TO GRATING COUPLED SURFACE PLASMON RESONANCE SENSORS[1]

[1] Sheppard, G. R.; Giasuddin, S.; Baba, A.; and Locklin, J. Submitted to *Analyst*, 10/15/12.

**Abstract**

Blu-ray discs (BD) were utilized to create a grating couple surface plasmon resonance (SPR) molecular sensors using a "grafting-through" photopolymerization to modify the sensor surface. Discs coated with a Ag film exhibit a sharp reflectivity dip when 632.8 nm light source excites surface plasmons at the gratings negative diffraction orders. The 320 nm pitch of the blu-ray disc creates a single plasmon dip, which can be used for chemical sensing when combined with molecular imprinting. The effects of the plasmon dip's angular shift were explored using rigorous coupled wave analysis to predict the imprinted polymer's thickness and refractive index. Imprinted polymers with small molecule toxins, histamine and microcystin-LR, were used to create 125 nm and 86 nm films, respectively. Plasmon shifts due to re-binding of the respective target molecules created 0.4° and 2.1° shifts due to changes in the film's refractive index by 0.005 and 0.02. The reproducible plasmon shifts of the blu-ray disc sensor were used to distinquish between binding pocket solvation effects and the selective binding of the target molecules.

## Introduction

Surface plasmon resonance (SPR) is a well-known, label-free technique that has been used to monitor interfacial binding events in a wide variety of disciplines.[1-9] Such binding occurs within a dielectric layer that is attached to a noble metal surface. Excitation of the surface plasmon resonance in the commonly used Kretschmann configuration occurs when the wave vector of the incident photon matches that of the surface polariton.[1, 9-13] These surface polaritons are sensitive to changes in thickness and refractive index (RI) of the dielectric medium in contact with the metal interface.[3, 9] As a binding event occurs, the thickness of the dielectric layer at the interface increases, resulting in a shift of the plasmon excitation angle. Monitoring the resulting change in angle allows for real-time detection of a binding event at the interface.

Recently, the use of diffraction gratings has attracted interest as an alternative method for exciting surface plasmon resonance.[14, 15] Gratings produce diffraction patterns that are dependent on the wavelength of incident light, angle of incidence, and grating structure.[16,18-20] When the grating is coated with a noble metal, the wave vector of the incident photons are coupled to the metal layer at different diffraction orders.[9, 16, 17] For a particular grating structure, the surface plasmon angle $\theta_m$ can be estimated through equation 1,

$$sin(\theta_m) + m\frac{\lambda}{\Lambda} = \pm Re\left\{\sqrt{\frac{\varepsilon_a n_d^2}{\varepsilon_a + n_d^2}}\right\} \quad (1)$$

where $m$ is the diffraction order for a wavelength $\lambda$ and period $\Lambda$ at the interface of a metal with a dielectric of $\varepsilon_a$ and medium with a refractive index $n_d$. Grating coupled surface plasmon resonance has demonstrated comparable sensitivity to the

Kretschmann configuration[18] with the added advantage that grating periodicity and amplitude can be adjusted to tune the SPR response to specific angles or wavelengths.[19]

Periodic grating structures for SPR sensors are typically fabricated through a variety of complex lithographic techniques that are not readily accessible.[20-22] On the other hand, optical storage media such as CDs, DVDs, and blu-ray discs (BDs) offer a low cost and reproducible grating structure that is commercially available.[19, 23, 24] These discs utilize a continuous spiral grating molded into the polycarbonate layer to guide a laser that reads the pits or grooves etched into a metal or dye layer along the disc's track. CDs and DVDs, with grating periods of 1600 nm and 740 nm, respectively, have been used to produce sharp SPR signals.[19, 24] However, these periods produce both positive and negative diffraction modes, each of which can excite surface plasmon resonance within the viewing region. At constant wavelength, an increase in the dielectric layer thickness or RI will shift a positive diffraction order to higher incident angles, while a negative diffraction order will shift to a lower angle. When multiple diffraction orders are present within the viewing region, the signal processing for sensing applications becomes complex. In order to produce a sharp and isolated plasmon resonance, the grating period can be lowered, resulting in a single diffraction order within the angular viewing region. Blu-ray discs, with a 320 nm pitch, satisfy the appropriate conditions for viewing an isolated diffraction order over a larger dielectric thickness range.

SPR platforms for biological sensing applications have been widely studied to track the binding events of specific analyte-antibody interactions.[1, 11, 25-27] However, isolating specific binding pairs and immobilizing them to the surface is often a

tedious and costly approach.[28, 29] An alternative strategy has been to create synthetic antibodies using molecular imprinted polymers (MIPs) to selectively bind a single analytes.[30-33] MIPs use a crosslinked polymer network to encapsulate a target molecule creating a synthetic binding pocket.[31, 34-36] This binding cavity is not only size selective, but exhibits energetic favorability to the imprinted molecule due molecular interactions, such as hydrogen bonding, between the target molecule and the polymer.[30, 33, 37, 38] This technique is amenable for chemical sensors as the artificial antibody can be rapidly produced while maintaining selectivity.

In this study, we have combined molecularly imprinted polymers with blu-ray discs to create a selective grating coupled SPR sensor. Molecular imprinting monomers with hydrogen bonding moieties were utilized to create an artificial binding cavity that is selective for the target molecule, following a previously optimized monomer-crosslinker ratio.[38-40] Using a "grafting through" technique, an imprinted polymer was attached to the surface of a noble metal coated disc. The effects of film thickness and RI on the plasmon dip angle were investigated using rigorous coupled wave analysis. Angular SPR measurements of imprinted films were monitored using a HeNe laser (632.8 nm). The binding of two toxins, histamine[39, 41] and microcystin-LR[42, 43], was used to determine the capabilities of the blu-ray disc as a molecular sensor.

## Experimental

### Materials

All chemicals were used as received unless noted otherwise. Allyl mercaptan and ethylene glycol dimethacrylate (EGDMA) were purchased from TCI. Solvent and initiator, dimethyl sulfoxide (DMSO, >99.5%) and azobisisobutyronitrile (AIBN) were purchased from Sigma Aldrich. Methacrylic acid, histamine dihydrochloride, and L-histidine were purchased from Alfa Aeser. Methacrylic acid (MAA) and EGDMA were passed through a plug of neutral alumina to remove inhibitor. Microcystin-LR was provided by Dr. Jia-Sheng Wang group's at the University of Georgia. Silver (99.99 %) and titanium (99.99 %) were purchased from Kurt J. Lesker. Blu-ray discs (RiData, BD-R, single layer) were purchased Amazon.com.

### Fabrication of SPR Grating Substrates

Blu-ray discs were cut into 2 cm x 3 cm substrates. The discs have a protective polymer layer over the grating which was peeled off after heating the substrates to 90 °C in air for 30 sec. The dye layer was removed by rinsing with ethanol and dried under a nitrogen stream. A silver film was deposited onto the exposed grating using an electron beam deposition system (Kurt J. Lesker, PVD75) at 0.5 Å/s after depositing 10 nm of titanium as an adhesion layer.

### Molecular Imprinting Polymerization

A molecular imprinting stock solution consisting of monomer (MAA, 12.7 mmol, 1.08 mL) and crosslinker (EGDMA, 25.4 mmol, 4.79 mL) was mixed with 5 mL of DMSO. Target molecules, histamine (30 mM) and microcystin (5 mM), were well mixed into aliquots of the stock solution. AIBN was added at one mole percent

equivalence of the combined molar amounts of monomer and crosslinker. The solution was degassed with argon for 10 min prior to polymerization. Stock solutions were stored at 0 °C in the dark.

The polymer was attached to the surface in a "grafting through" method. Silver gratings were coated with allyl mercaptan (10 mM) by overnight solution deposition in ethanol. Monomer solution (1 μL) with the template molecule was pipetted onto the grating. A clean glass slide was clamped to the grating substrate. The grating surface was exposed to 2 $mW/cm^2$ ultra-violet irradiation (365 nm) for 5 min. After polymerization was complete, the glass slide was removed and the imprinted polymer rinsed with ethanol and dried with nitrogen.

**Characterization**

Grating substrates are characterized by surface plasmon resonance using a Multiskop (Optrel GbR) in the surface plasmon scanning mode with a HeNe laser (632.8 nm). Atomic force microscopy (AFM) images were taken on a Multimode NanoScope V (Bruker) instrument using a silicon AFM probe with a spring constant of 48 N/m and resonant frequency of 190 kHz in tapping mode. The AFM software has a power spectral density analysis program built into the program. Thickness of the imprinted polymers was determined by spectroscopic ellipsometry (J.A. Woollam, M-2000V). Grating coupled SPR modeling was performed on G-Solver (Grating Solver Development, Co.) using rigorous coupled-wave analysis.

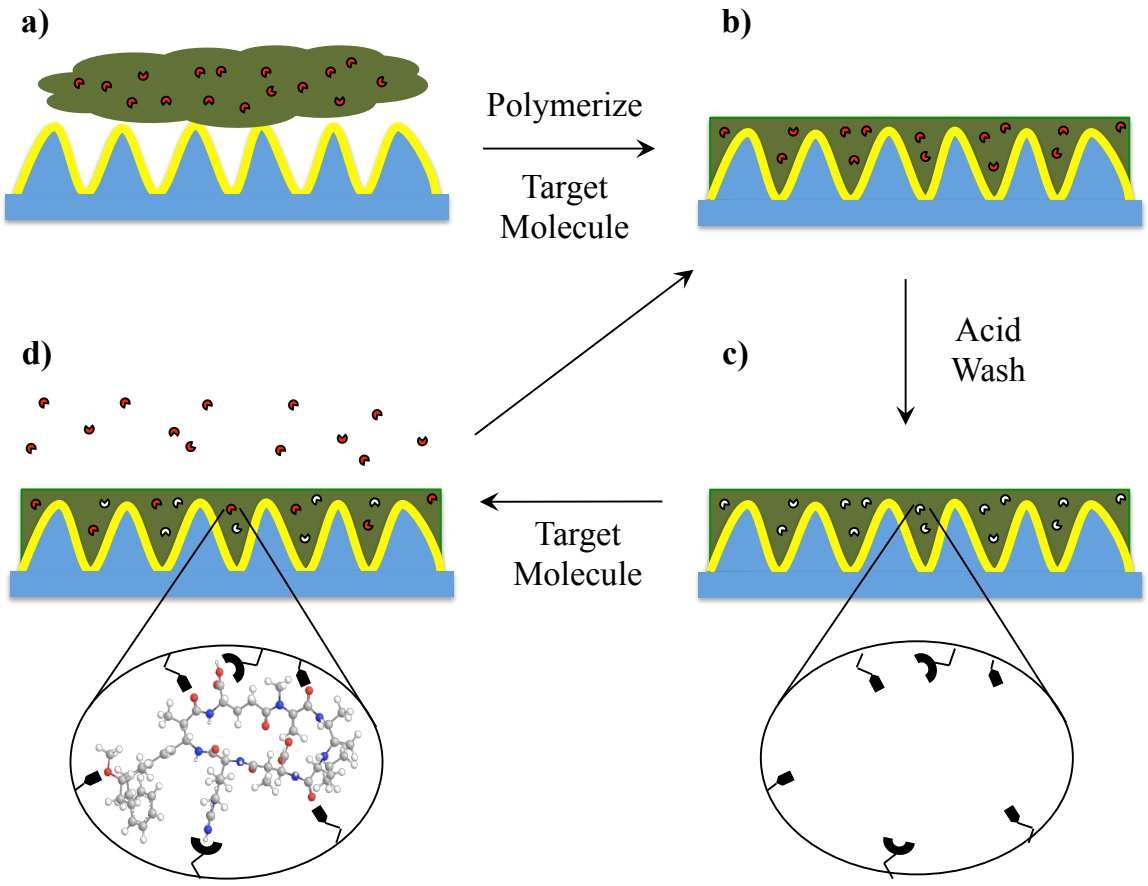


**Figure 4.1.** Fabrication scheme of the molecularly imprinted, grating coupled surface plasmon resonance sensor; a) monomer solution deposited onto a noble metal coated grating, b) exposure to UV light initiates polymerization, encapsulating the target molecule, c) the imprinted molecules removed by an acid wash, and d) the selective rebinding of the target molecule.

**Results and Discussion**

Molecularly imprinted sensors were fabricated on blu-ray discs by polymerizing the monomer solution onto a noble metal coated disc with a monolayer of allyl mercaptan, Figure 4.1a. The thiol moiety allows attachment to the noble metal layer, where the terminal double bond acts as a surface bound monomer for grafting through polymerization.[44-46] A variety of different molecular imprinting monomer combinations can be found within the literature.[39, 40, 47-49] For this study, the monomer and crosslinker ratio was adopted from those used by Horemans *et al.* who determined that for histamine a 1:2 ratio of methacrylic acid and ethylene glycol dimethacrylate was optimal for molecular imprinting.[39] The same ratio was used to monitor the binding of microcystin, as shown by Figure 4.1, where the hydrogen bonding donors and accepters are presented by the block and semi-circles. In order to produce a dispersed, uniform film, a piece of clean BK7 glass was clamped to the grating.[40] As the substrates are clamped together, the solution readily wets along the grating channels dispersing the monomer solution across the entire surface. Wetting the channels ensures that the mixture makes contact with the surface-bound allyl group, affording a covalently bound polymer network attach to the grating surface. Contact with the glass also imparts a smooth surface on the top portion of the imprinted polymer, which reduces any light scattering.

The solution was photo-polymerized in the presence of a target molecule to create the synthetic binding pockets, as shown in Figure 4.1b. A crosslinking monomer was used to impart rigidity to the polymer network to lock the hydrogen bonding donors and acceptors into positions that favor a thermodynamically stable pocket around the target

molecule. Molecules larger than the imprinted template will be precluded from binding due to steric congestion within the crosslinked polymer network. Size exclusion will not prevent smaller molecules from diffusing into the binding cavity, however, molecules that do not match the hydrogen bonding sites within the pocket will have a reduced binding affinity.

The target molecule was then removed from the imprinted polymer by disrupting the hydrogen bonding with an acidic solution, Figure 4.1c. In the subsequent studies, water at pH 3.0 was pipetted onto the polymer and allowed to sit for 30 min to remove the various imprinted chemicals. Removal of the target molecule was limited by the molecular diffusion through the crosslinked polymer. Adequate time frames for toxin removal and binding are needed to provide plasmon shifts that are statistically different between the unbound and bound analyte. Extraction at shorter time frames (10 and 20 min) resulted in minute SPR shifts indicating insufficient removal of the target molecule, while longer periods (> 30 min) produced no further SPR shifts for each of the target molecules studied. Molecular binding to the synthetic analyte was accomplished by pipetting a stock solution of the target molecule onto the molecularly imprinted polymer, Figure 4.1d. After 30 min of exposure, the MIP grating was rinsed with ethanol and nitrogen dried prior to measuring the plasmonic shift. Washing the grating removes any unbound molecules present on the polymer surface. The resulting shifts in the plasmon signal will therefore only be related to the bound molecules.

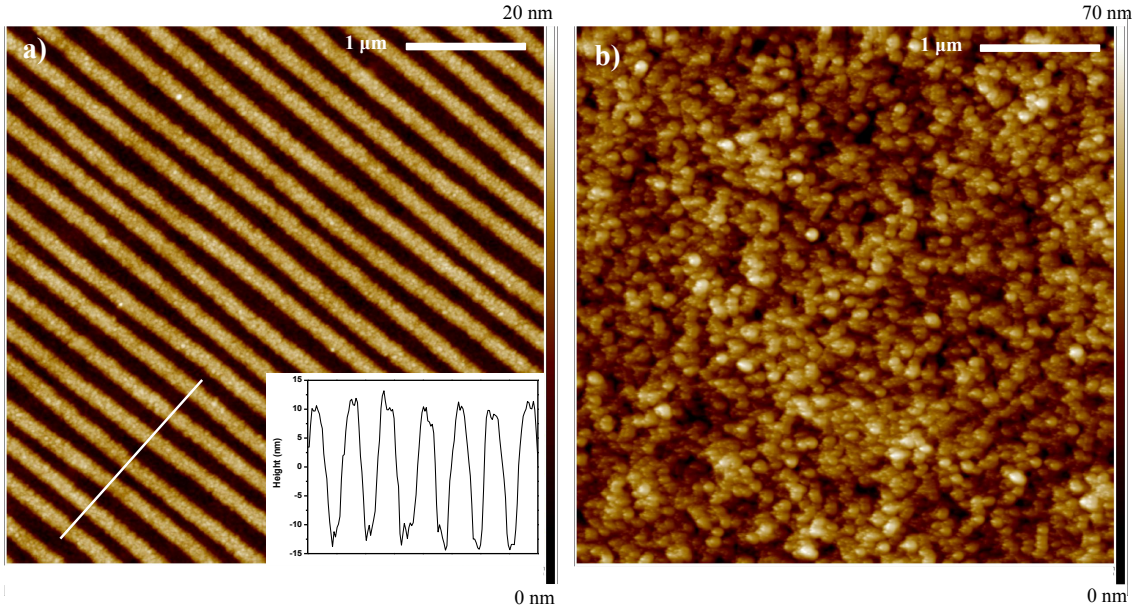


**Figure 4.2.** AFM images of the a) BD disc grating with noble metal coating and b) a molecularly imprinted blu-ray disc. Inset indicates the height profile along the diagonal line.

The surface morphology of the Ag coated blu-ray disc is demonstrated in Figure 4.2a by an AFM image. The inset indicates the height profile taken at the diagonal line. The 100 nm metal film does not alter the grating periodicity which has a 310 nm pitch before and after the metal deposition. Periods were measured at the positions where the molecularly imprinted polymer would be deposited for sensing. The amplitude of the sinusoidal grating was increased from 12 nm with the native metal on the blu-ray to 28 nm after noble metal deposition. The periodicity and amplitudes were calculated through the AFM software (Nanoscope Analysis, Bruker Inc.) using power spectral density analysis. Amplitude changes are a result of the e-beam deposition where the metal condenses on the first surface it comes into contact

with. As the metal deposition proceeds, condensation of the metal will begin on the peaks of the grating. The metal vapor has to diffuse into the troughs before the condensation of the metal can occur. With different deposition rates, the metal will deposit at different rates along the grating, which will affect the amplitude of the grating structure. SPR signals with different amplitudes has been previously investigated using CDs and DVDs.[19] Solvent etching of the polycarbonate layer was used to improve the SPR signal with the sharpest responses using amplitudes of 50 to 90 nm for CDs and 20 to 60 nm for DVDs. Alternatively for blu-ray discs, Kapalan *et. al.* determined that the 20 nm grating depth required no modification to achieve sharp plasmonic curves. As shown in Figure 4.2b, AFM analysis of the top surface of the molecularly imprinted polymer film created using photo-polymerization does not demonstrate any grating characteristics, indicating that the MIP was thicker than the grating's amplitude. Due to variations in the height of the grating structure (Figure 4.2a, inset) the monomer can wet the surface within the channels as well as laterally across the grating. After polymerization the imprinted films were ~130 nm nm thick with an RMS roughness of 9.8 nm. The thickness of the brush was estimated using spectroscopic ellipsometry (J.A. Woollam Co., M2000V) with incident light perpendicular and normal to the grating direction. The data was modeled within the accompanying software (CompleteEASE) by fitting the thickness and RI in the spectral regions where surface plasmon resonance were not observed to propagate. The RI was modeled using a Cauchy equation, which produced a value of 1.42 at 632.8 nm wavelength of light. The refractive index is consistent with the RI of bulk polymer as determined by spectroscopic ellipsometry on a non-grating surface.

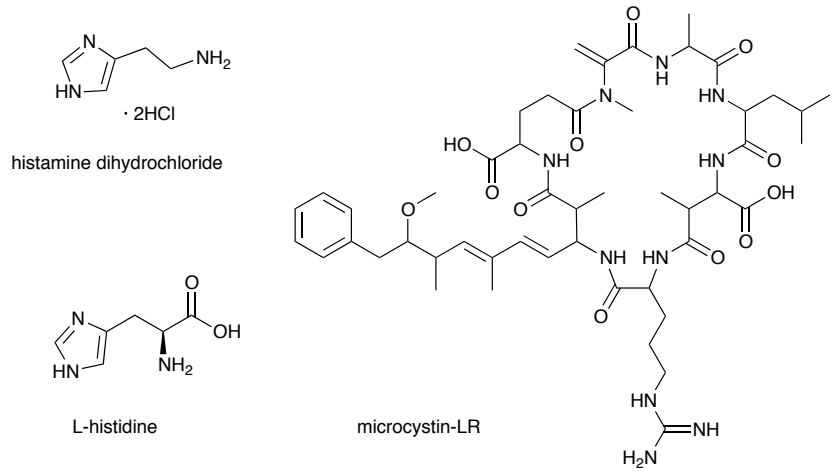


**Figure 4.3.** Structures of the molecularly imprinted molecules (histamine and microcystin-LR) and analogous molecules utilized in determining molecular selectivity.

Modeling the reflection intensity of a blu-ray disc produced an SPR response similar to that of a polymer coated sensor with a thickness of 125 nm, which coincided with the thickness value taken by spectroscopic ellipsometry.

Molecularly imprinted blu-ray disc sensors were created using histamine and microcystin-LR (Figure 4.3) as target molecules. Histamine has been previously studied with imprinted polymers and was used as comparative study.[39] Microcystin-LR is larger than histamine or histidine and was used to compare the selectivity of a larger binding pocket with smaller molecules. Grating structures excite surface plasmons by coupling the photon energy at the various diffraction orders, which can be tracked spectrally as shown by Kaplan *et. al.*,[19] or by using a fixed wavelength and varying the angle of incidence. In these studies, the wavelength of light was fixed to 632.8 nm with a HeNe laser with a 1 $mm^2$ incident area. A plasmonic excitation will occur when the incident photons matches one of the diffraction angles. The generation

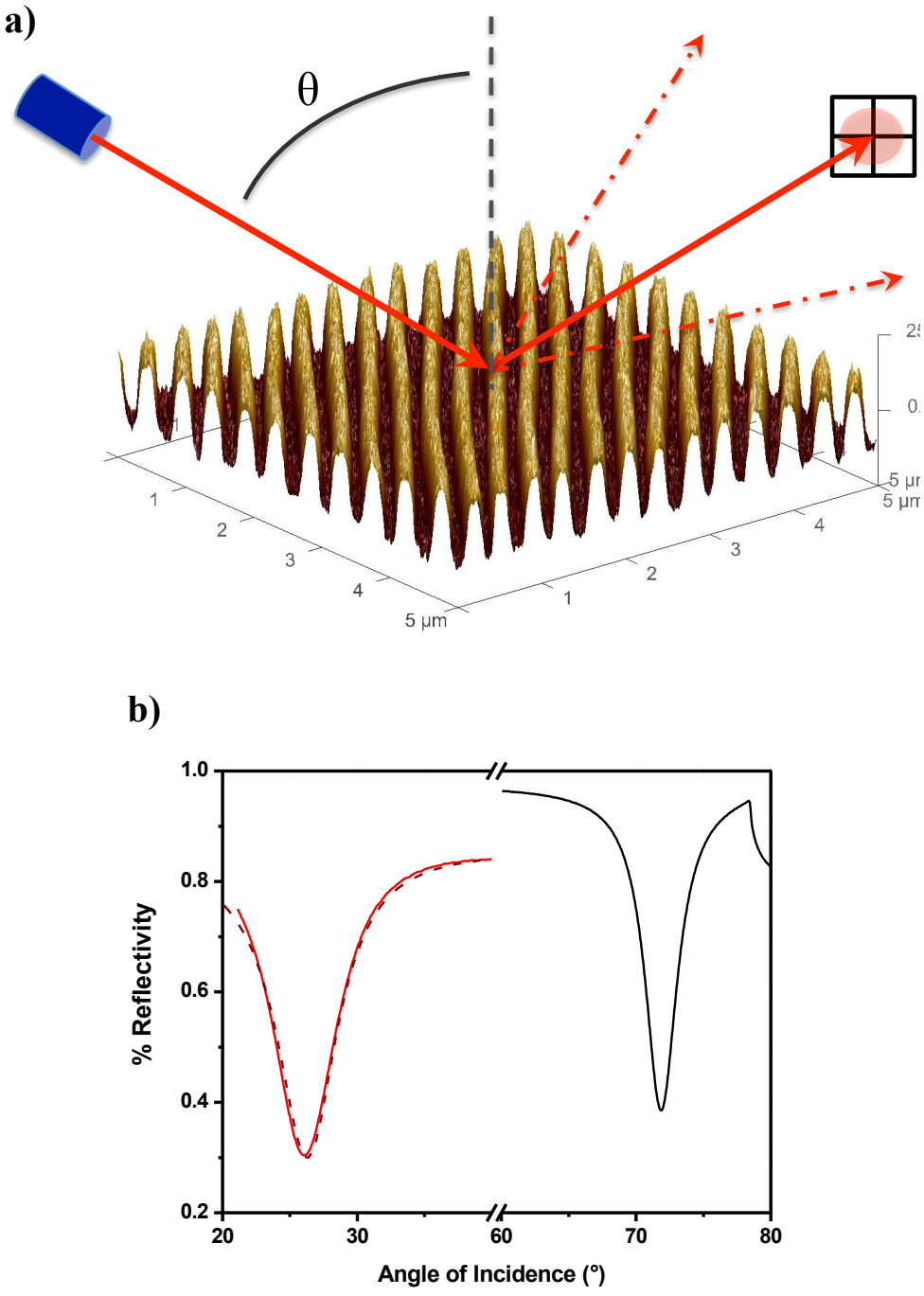


**Figure 4.4.** Diagram of the angular scanning setup on a blu-ray disc. a) Photons couple to the noble metal when the incident angle matches the diffraction order produced by the grating. b) The plasmonic response from a blu-ray grating with a 100 nm Ag film (black) and with a 125 nm imprinted polymer (red). Dashed line indicates modeled data.

of the surface plasmons is then recorded as a dip in the reflection intensity. The angular scanning setup is pictorially represented by Figure 4.4a with an AFM image of the blu-ray disc's grating. Representative reflectivity curves for a BD sensor are shown in Figure 4.4b. The black line is a 100 nm Ag coated BD with a sharp dip at an incident angle of 72°. The excitation for the metal coated disc is characteristic of a negative first order plasmon dip. When a dielectric layer, such as the imprinted polymer, is added to a negative diffraction order the plasmon dip shifts to lower incident angles as evidenced by the plasmon shift to 26° with a histamine imprinted polymer in Figure 4.4b (red).

Modeling the plasmonic dip produced by the imprinted polymer film confirmed the thickness of the imprinted polymer layer on the blu-ray sensors. The dashed line in Figure 4.4b represent the data fit by rigorous coupled-wave analysis using G-Solver. For the imprinted polymer curve, the thickness of the dielectric layer was adjusted to match the shift of the surface plasmon resonance. The calculation held the RI constant at 1.5 and varied the thickness of the polymer layer on top of the grating, Figure 4.5. As the thickness was increased from 70 nm to 150 nm by increments of 10 nm, the surface plasmon dip shifted to lower angles. A similar shift to lower angles of incidence occurs as the simulated RI was raised from 1.47 to 1.50 by 0.01 increments. This indicates that the angular shift observed during chemical binding could be a result of thickness or RI changes. As the molecular imprinting polymer is highly crosslinked, changes in thickness are considered to be negligible. During binding, the target molecule has to diffuse into the pocket resulting in minor changes in the localized polymer network. Once bound, the polymer network relaxes

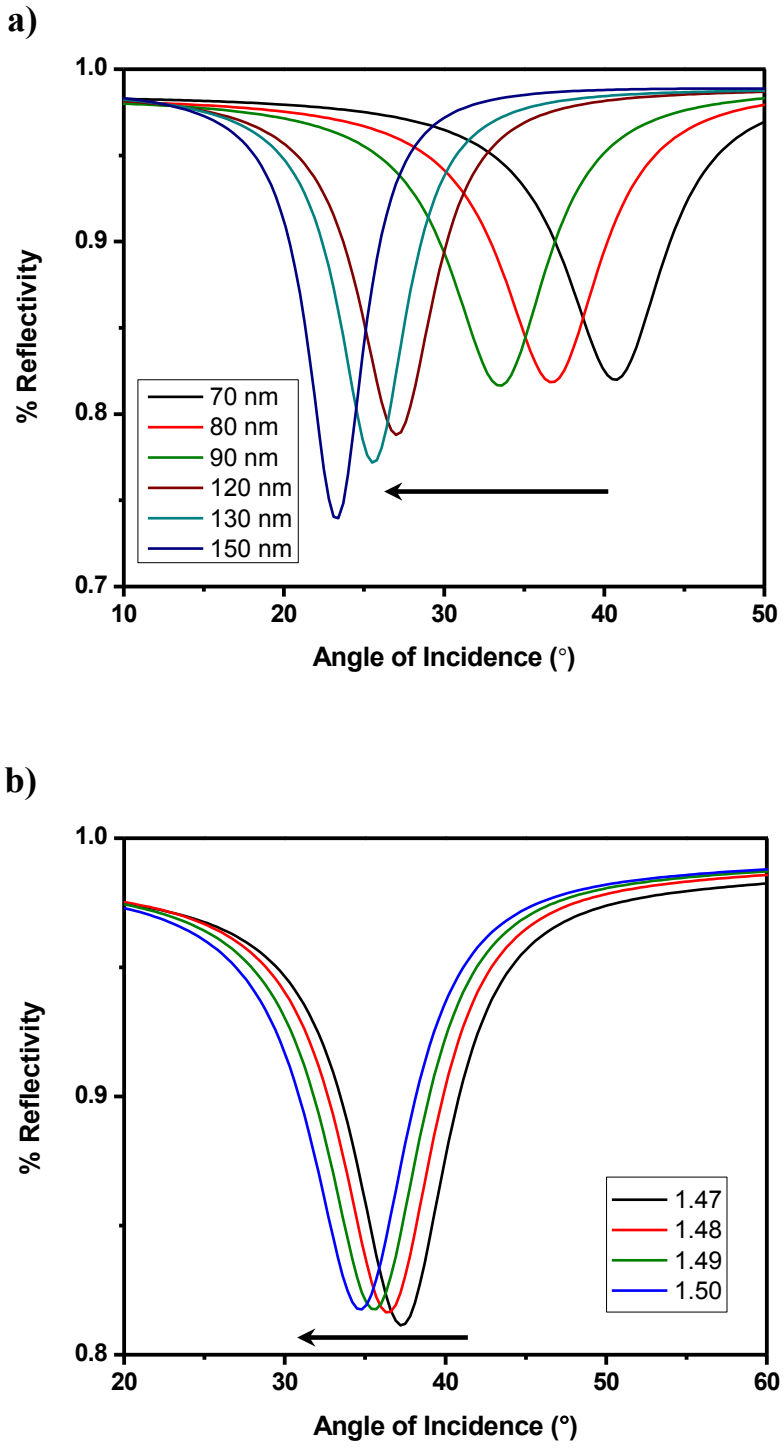


**Figure 4.5.** Modeled surface plasmon reflectivity curves for a blu-ray disc at various a) thicknesses and b) refractive indices. As the thickness or refractive index increases, the plasmon shifts to lower incident angles as indicated by the arrow.

to the energetically favorable positions formed during templating. Due to the presence of the bound molecule the RI of the film increased from the unbound state to a bound state. In this study the bound state is treated as a continuous organic layer with a constant RI of 1.5. The unbound state is not a continuous layer due to the absence of the target molecule within the binding cavity. The effective RI of the polymer will therefore be lower due to the presence of air or solvent within the pockets. Solvents with refractive indices lower than the bulk polymer were used for binding events to eliminate the possibility of false positives during detection of the target molecules.

A molecularly imprinted histamine sensor was cycled through removal and capture of the target molecule to determine the reproducibility of the binding event. The resulting polymer with histamine had a SPR minimum at 26°. The imprinted histamine was removed after an acid wash, which produced the black SPR curve in Figure 4.6. Histamine was rebound within the polymer by exposing to a 30 mM aqueous solution (Figure 4.6, red). After exposure, the MIP was rinsed with water and ethanol to remove any physisorbed material, leaving histamine within the binding pocket. The presence of the histamine changes the dielectric layer causing the plasmon to shift left. The rebound histamine produced a plasmon dip at 26°. Repeating the acid wash and binding event produces a consistent shift in the plasmon with the unbound plasmon dip at 26.4 ± 0.088° and the bound state at 26.0 ± 0.003°. The 0.4° shift in the plasmon indicates a 0.005 change in RI in the film due to the binding event. The selectivity of the sensor to histamine was determined by exposing the unbound imprinted polymer to histidine, a molecule which has a similar structure to histamine with an extra carboxylic acid group. Exposure to a 30 mM solution of

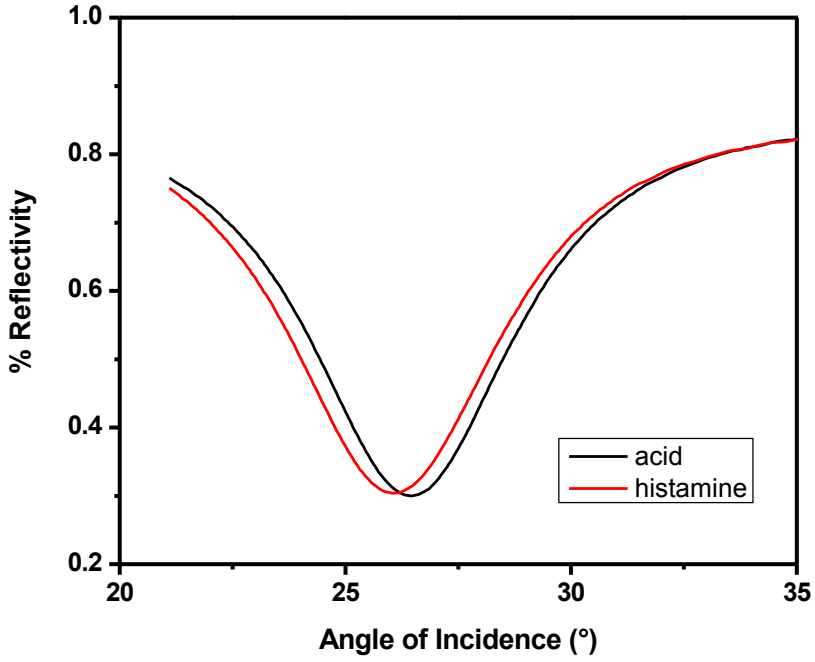


**Figure 4.6.** Sensing of histamine by a molecularly imprinted polymer on a blu-ray disc. The SPR shift from the black line to the red line indicates histamine binding.

histidine did not shift the surface plasmon resonance angular dip, which indicates the lack of a binding event (Figure 4.7). A final histamine binding produced the same plasmon shift as the initial binding event indicating that molecular sensing is reproducible even after exposure to complementary analytes.

The blu-ray imprinted sensor was tested on a larger molecule, microcystin-LR, in order to compare the sensing capabilities of different analytes. Microcystin has a larger hydrodynamic radius than histamine, which creates a larger binding pocket. As the molecule size increases, the diffusion of the molecule through the polymer network is impeded. In this study, the monomer concentrations used for molecular imprinting of

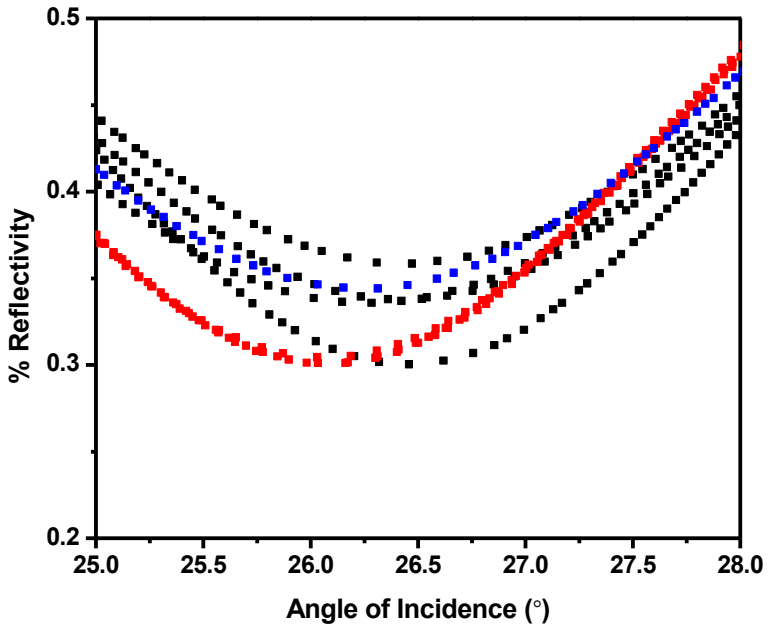


**Figure 4.7.** Variation in the histamine imprinted blu-ray disc sensor. Data in red represent histamine bound in the binding cavity while data in black is the unbound state. Histidine binding attempt is in blue.

histamine were used with a 5 mM microcystin imprinting. Polymerization of the solution followed the methods previously described, as well as the subsequent rinsing steps. Removal of the microcystin resulted in a plasmon dip with a minimum at an angle of incidence of 36.7°, Figure 4.8. Exposing the MIP to the DMSO solution with microcystin lowered the plasmon angle by 2.1°. The shift to a lower incident angle is consistent with the histamine blu-ray disc sensor, indicating that the dielectric film increased in RI. Fitting the reflectivity data from the bound microcystin using G-Solver produced a thickness of 86 nm with a RI of 1.5. In the bound state, the imprinted polymer was presumed to act as a uniform dielectric medium with no variations in the RI of an organic

thin film. Alternatively, the unbound state of the MIP has pockets where solvent can persist, decreasing the effective refractive index of the dielectric layer when a lower RI solvent was used. Modeling the imprinted polymer's unbound state produced an effective RI of 1.48. As the RI of the dielectric film decreases the blu-ray plasmon shifts to higher angles. The plasmon dips for the bound and unbound microcystin imprinted polymer were consistent over three binding trials with a variance of 0.3° for each state of the MIP, Figure 4.9.

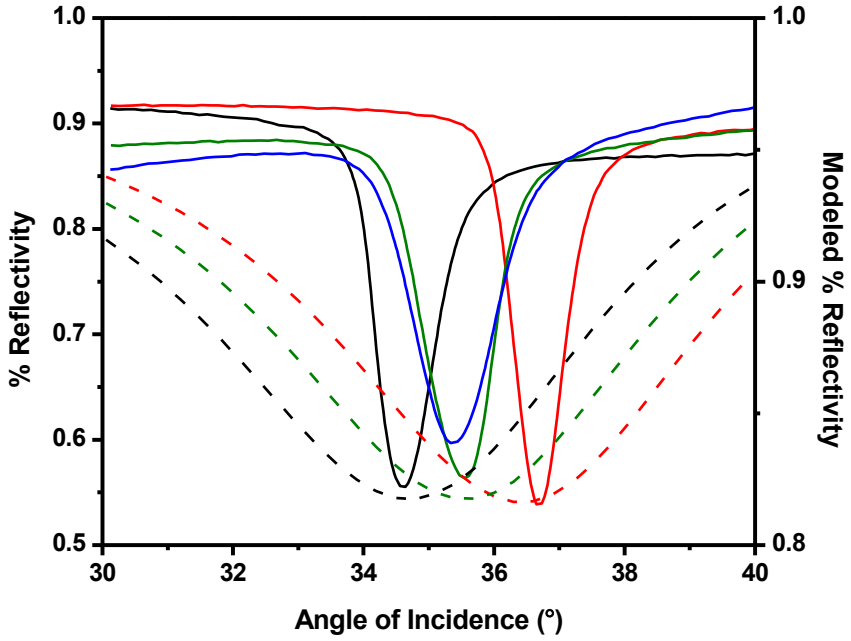


**Figure 4.8.** Shift in surface plasmon resonance angle due to binding of microcystin (black line) in a molecularly imprinted thin film on a blu-ray grating. Dashed lines indicate the modeled plasmon shift due to refractive index changes. Solvated binding cavities are shown in red and green for water and DMSO, respectively. SPR response from histidine binding is shown in blue.

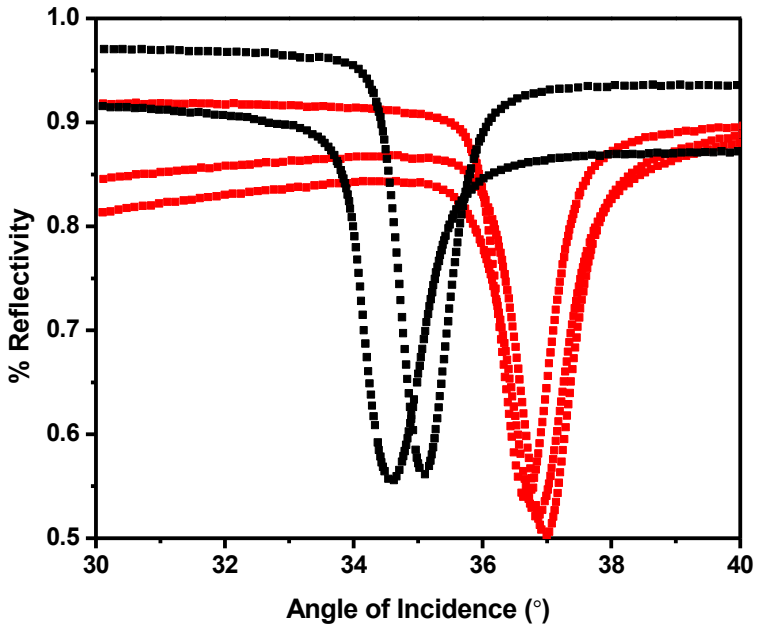


**Figure 4.9.** Binding of microcystin on a blu-ray disc molecular imprinted SPR sensor. Data in red indicates the unbound state of the imprinted sensor, while data in black shows the bound microcystin.

Pocket solvation effects were explored by exposing the unbound microcystin sensor to DMSO for 30 min. The modeled RI of the solvated film was 1.49 as determined by matching the 35.6° plasmon dip angle (Figure 4.8, green solid line) by rigorous coupled wave analysis (green dashed line). The lowering of the RI from a bulk organic film is consistent with a dielectric layer of mixed refractive indices. Due to the differences in RI, a DMSO (n = 1.48) solvated-binding cavity will shift the plasmon dip to lower angles than a water (n = 1.33) solvated imprinted polymer. With larger binding pockets, solvation effects must be taken into account when the sensor

is exposed to analyte solutions that do not have the target molecule, but are comprised of smaller molecules with hydrogen bonding moieties. Exposing the microcystin imprinted sensor to histamine in DMSO also produced a plasmon shift to 35.4° (Figure 4.8, blue line) which was within the 0.2° variance of the solvated plasmon dip. Histamine's hydrogen bonding moieties can interact with those within the synthetic antibody. However, the histamine or solvent molecules will not match all of the hydrogen bonding sites within the antibody, causing a thermodynamic instability resulting in a binding site that is partially solvated. With the histamine plasmon dip within the range of those measured for DMSO, solvation effects within the binding cavity likely cause the resulting plasmon shift.

## Conclusions

Blu-ray discs as a grating coupled surface plasmon resonance sensor were used to track the binding events of two small molecule toxins, histamine and microcystin-LR. Synthetic binding pockets were created using molecularly imprinted polymers to selectively sense the presence of the target molecules in solution. The addition of the polymer layer alters the plasmon dip angle at a fixed wavelength. Shifts of the plasmon dip angle due to different polymer thicknesses and refractive indices were predicted using rigorous coupled wave analysis. While the thickness of the polymer layer defines the initial plasmon angle, 26° and 36.7° for 125 nm and 86 nm thicknesses respectively, the change in the RI before and after chemical sensing induced the local shifts in the plasmon. The imprinted sensors exhibited 0.4° and 2.1° shifts for histamine and microcystin, respectively, which corresponeded to refractive index changes of 0.005 and 0.02. When binding larger molecules, microcystin-LR, the imprinted sensor was shown to retain selectively even when exposed to smaller molecules or as the pocket is solvated. When combined with selective techniques like molecular imprinting, blu-ray discs can provide a means to produce cost effective chemical sensors.

## References


1. Homola, J., *Chem. Rev.* **2008,** *108* (2), 462-493.

2. Kato, K.; Ishimuro, T.; Arima, Y.; Hirata, I.; Iwata, H., *Anal. Chem.* **2007,** *79* (22), 8616-8623.

3. Brockman, J. M.; Nelson, B. P.; Corn, R. M., *Annu. Rev. Phys. Chem.* **2000,** *51* (1), 41-63.

4. Wang, Z.; Wilkop, T.; Xu, D.; Dong, Y.; Ma, G.; Cheng, Q., *Analytical and Bioanalytical Chemistry* **2007,** *389* (3), 819-825.

5. Linman, M. J.; Taylor, J. D.; Yu, H.; Chen, X.; Cheng, Q., *Anal. Chem.* **2008,** *80* (11), 4007-4013.

6. Liang, P.-H.; Wang, S.-K.; Wong, C.-H., *J. Am. Chem. Soc.* **2007,** *129* (36), 11177-11184.

7. Lee, H. J.; Wark, A. W.; Corn, R. M., *Langmuir* **2006,** *22* (12), 5241-5250.

8. Scarano, S.; Mascini, M.; Turner, A. P. F.; Minunni, M., *Biosens. Bioelectron.* **2010,** *25* (5), 957-966.

9. Knoll, W., *Annu. Rev. Phys. Chem.* **1998,** *49* (1), 569-638.

10. Kurihara, K.; Suzuki, K., *Anal. Chem.* **2002,** *74* (3), 696-701.

11. Campbell, C. T.; Kim, G., *Biomaterials* **2007,** *28* (15), 2380-2392.

12. Homola, J.; Koudela, I.; Yee, S. S., *Sensors and Actuators B: Chemical* **1999,** *54* (1-2), 16-24.

13. Schuck, P., *Annu. Rev. Biophys. Biomol. Struct.* **1997,** *26* (1), 541-566.

14. Yu, F.; Knoll, W., *Anal. Chem.* **2004,** *76* (7), 1971-1975.

15. Lee, H. J.; Wark, A. W.; Corn, R. M., *Analyst* **2008,** *133* (5), 596-601.

16. Fernandez, U.; Fischer, T. F.; Knoll, W., *Optics Communications* **1993,** *102* (1-2), 49-52.

17. Raether, H., *Optics Communications* **1982,** *42* (4), 217-222.

18. Piliarik, M.; Homola, J., *Opt. Express* **2009,** *17* (19), 16505-16517.

19. Kaplan, B.; Guner, H.; Senlik, O.; Gurel, K.; Bayindir, M.; Dana, A., *Plasmonics* **2009,** *4* (3), 237-243.

20. Yeh, W.-H.; Kleingartner, J.; Hillier, A. C., *Anal. Chem.* **2010,** *82* (12), 4988-4993.

21. Marikkar, F. S.; Carter, C.; Kieltyka, K.; Robertson, J. W. F.; Williamson, C.; Simmonds, A.; Zangmeister, R.; Fritz, T.; Armstrong, N. R., *Langmuir* **2007,** *23* (20), 10395-10402.

22. McPhillips, J.; McClatchey, C.; Kelly, T.; Murphy, A.; Jonsson, M. P.; Wurtz, G. A.; Winfield, R. J.; Pollard, R. J., *The Journal of Physical Chemistry C* **2011,** *115* (31), 15234-15239.

23. Baba, A.; Aoki, N.; Shinbo, K.; Kato, K.; Kaneko, F., *ACS Applied Materials & Interfaces* **2011,** *3* (6), 2080-2084.

24. Singh, B. K.; Hillier, A. C., *Anal. Chem.* **2008,** *80* (10), 3803-3810.

25. Wegner, G. J.; Wark, A. W.; Lee, H. J.; Codner, E.; Saeki, T.; Fang, S.; Corn, R. M., *Anal. Chem.* **2004,** *76* (19), 5677-5684.

26. Smith, E. A.; Thomas, W. D.; Kiessling, L. L.; Corn, R. M., *J. Am. Chem. Soc.* **2003,** *125* (20), 6140-6148.

27. Zhou, W.-J.; Halpern, A. R.; Seefeld, T. H.; Corn, R. M., *Anal. Chem.* **2011,** *84* (1), 440-445.

28. Kodadek, T.; Reddy, M. M.; Olivos, H. J.; Bachhawat-Sikder, K.; Alluri, P. G., *Acc. Chem. Res.* **2004,** *37* (9), 711-718.

29. Law, W.-C.; Yong, K.-T.; Baev, A.; Prasad, P. N., *ACS Nano* **2011,** *5* (6), 4858-4864.

30. Asanuma, H.; Hishiya, T.; Komiyama, M., *Adv. Mater.* **2000,** *12* (14), 1019-1030.

31. Ye, L.; Mosbach, K., *Chem. Mater.* **2008,** *20* (3), 859-868.

32. Chen, H. C.; Lee, Y. C.; Hwang, D. F.; Chiou, T. K.; Tsai, Y. H., *Journal of Food Safety* **2011,** *31* (3), 320-325.

33. Mosbach, K.; Ramstrom, O., *Nat Biotech* **1996,** *14* (2), 163-170.

34. Cai, D.; Ren, L.; Zhao, H.; Xu, C.; Zhang, L.; Yu, Y.; Wang, H.; Lan, Y.; Roberts, M. F.; Chuang, J. H.; Naughton, M. J.; Ren, Z.; Chiles, T. C., *Nat Nano* **2010,** *5* (8), 597-601.

35. Byrne, M. E.; Park, K.; Peppas, N. A., *Advanced Drug Delivery Reviews* **2002,** *54* (1), 149-161.

36. Bossi, A.; Bonini, F.; Turner, A. P. F.; Piletsky, S. A., *Biosens. Bioelectron.* **2007,** *22* (6), 1131-1137.

37. Zhang, H.; Ye, L.; Mosbach, K., *Journal of Molecular Recognition* **2006,** *19* (4), 248-259.

38. Pichon, V.; Chapuis-Hugon, F., *Anal. Chim. Acta* **2008,** *622* (1-2), 48-61.

39. Horemans, F.; Alenus, J.; Bongaers, E.; Weustenraed, A.; Thoelen, R.; Duchateau, J.; Lutsen, L.; Vanderzande, D.; Wagner, P.; Cleij, T. J., *Sensors and Actuators B: Chemical* **2010,** *148* (2), 392-398.

40. Kugimiya, A.; Takeuchi, T., *Biosens. Bioelectron.* **2001,** *16* (9-12), 1059-1062.

41. Lehane, L.; Olley, J., *International Journal of Food Microbiology* **2000,** *58* (1-2), 1-37.

42. Chianella, I.; Piletsky, S. A.; Tothill, I. E.; Chen, B.; Turner, A. P. F., *Biosens. Bioelectron.* **2003,** *18* (2-3), 119-127.

43. van Apeldoorn, M. E.; van Egmond, H. P.; Speijers, G. J. A.; Bakker, G. J. I., *Molecular Nutrition & Food Research* **2007,** *51* (1), 7-60.

44. Rühe, J., Polymer Brushes: On the Way to Tailor-Made Surfaces. In *Polymer Brushes*, Wiley-VCH Verlag GmbH & Co. KGaA: 2005; pp 1-31.

45. Bialk, M.; Prucker, O.; Rühe, J., *Colloids and Surfaces A: Physicochemical and Engineering Aspects* **2002,** *198-200* (0), 543-549.

46. Beinhoff, M.; Appapillai, A. T.; Underwood, L. D.; Frommer, J. E.; Carter, K. R., *Langmuir* **2006,** *22* (6), 2411-2414.

47. Sibrian-Vazquez, M.; Spivak, D. A., *J. Am. Chem. Soc.* **2004,** *126* (25), 7827-7833.

48. Sibrian-Vazquez, M.; Spivak, D. A., *Macromolecules* **2003,** *36* (14), 5105-5113.

49. Takeuchi, T.; Haginaka, J., *Journal of Chromatography B: Biomedical Sciences and Applications* **1999,** *728* (1), 1-20.

# CHAPTER 5

# IN SITU DYNAMICS OF POLY(N-ISPROPYLACRYLAMIDE): EFFECTS OF HYDROGEL WATER CONTENT ON DRUG DELIVERY FROM THERMO-RESPONSIVE POLYMERS[1]

[1] Sheppard, G. R.; Giasuddin, S.; Orski, S.; and Locklin, J. To be submitted to *Analytical Chemistry.*

**Abstract**

Thermo-responsive polymer brushes were investigated as a controllable drug delivery mechanism for the release of chemotherapeutic drugs. Hydrogel polymer thin films were produced using surface initiated photo-polymerization of N-isopropylacrylamide. Poly(N-isopropylacrylamide) (pNIPAM) is a reversible thermo-responsive polymer with a lower critical solution temperature (LCST) of 32 °C. When the solution temperature is above the LCST, the polymer film will collapse, conversely swelling when below the LCST. Dynamics of the polymer swelling and collapse are studied by *in situ* spectroscopic ellipsometry in order to optimize drug loading and release from pNIPAM films. Applying effective medium approximations to the optical properties of a pNIPAM film provided insight into the amount of water and subsequently the quantity of drug within the thin film. In the swollen state the polymer contains up to 80 % water while the collapsed state maintains 30 % water as determined by differences in the refractive index of the polymer below and above the LCST, respectively. With a 70 % water lose upon collapse the amount of a chemotherapeutic drug, doxorubicin, loaded and released into a 150 nm pNIPAM film was determined. The absorbance of doxorubicin release was monitored by UV-vis with incremental sampling of a release medium as a doxorubicin loaded film was collapsed at 50 °C. A maximum cumulative absorbance of 0.012 was determined to occur within 60 min, which indicates an effective single collapse release of 1.04 nmol/cm$^2$ of doxorubicin.

## Introduction

In the development of smart surfaces, a recent focus has been on the use of stimuli-responsive polymers to induce physical and chemical changes in a film using an externally control stimulus.[1-7] Stimuli-responsive polymers are a unique class of organic thin films that respond to changes in their environment whether it be pH, temperature, salinity, or electrical signal.[1, 5, 6, 8, 9] Selectively applying the stimulus through control of the local environment these polymers can be utilized as a drug delivery mechanism.[6, 10, 11] Of the stimuli-responsive polymers, poly(N-isopropylacrylamide) (pNIPAM) has taken on a lot of interest as it exhibits what is known as a lower critical solution temperature (LCST) of 32 °C which is close to the internal body temperature of 38 °C.[5, 10, 12-14] For thermo-responsive polymers, raising the temperature of the LCST induces a conformation change within the pNIPAM causing the polymer to collapse.[14-16] In the case of pNIPAM, the collapse is due to the disruption of hydrogen bonding between water and the amide side groups of the polymer.[14-16] During the collapse the polymer chains undergo a rearrangement, which reduces the overall polymer size.[16]

As a reversible thermo-responsive hydrogel, pNIPAM can be used to deliver drugs by raising the local temperature above the LCST collapsing the polymer and releasing water.[16, 17] With water as the mobile phase, a water-soluble drug can be loaded into pNIPAM by swelling the film in the presence a drug-laden solution.[11, 18] This limits the amount of drug that can be loaded into the polymer as water only takes up a fraction of the volume of the swollen pNIPAM.[11, 18, 19] In order to accurately determine the amount of drug loaded into the polymer the quantity of water used to swell the hydrogel needs to be determined.

In this study, the swelling dynamics of a pNIPAM thin film are investigated to determine the amount of water-soluble drug that can be loaded into a thermo-responsive hydrogel. Polymer brushes are grown by photo-initiated free-radical polymerization using a surface bound initiator.[17, 20] The surface bound initiator produces polymer in a "grafting from" method, which leads to high grafting densities with polymer chains oriented away from the substrate.[17, 21-24] Adjusting the weight fraction of NIPAM monomer in solution controlled polymer brush thickness. As a hydrogel, pNIPAM brushes can be analyzed using effective medium approximations along with optical techniques such as spectroscopic ellipsometry to determine the amount of water contained within the brush.[19] Changes within the polymer brush can also be observed in situ to determine the dynamics of the thermo-responsive thin film as it collapses and swells. The delivery rate and effective dosage of doxorubicin delivered by the collapse of the hydrogel are determined by UV-vis spectroscopy.

## Experimental

### Materials

All chemicals were used as received unless noted otherwise. Tetrahydrofuran (THF), methanol, ethanol, and dichloromethane (DCM) were purchased from BDH. THF and DCM were distilled over sodium-ketyl and calcium hydride, respectively. N-isopropylacrylamide (NIPAM) was purchased from TCI and flashed through a basic alumina column to remove inhibitor prior to polymerization. Anhydrous dimethylformamide (DMF) (Drisolv, 99.8 % by GC) was purchased from EMD. Phosphate buffer saline (PBS) solution (10x) was purchased from Fisher and diluted to 5x with 18 MΩ water. PBS pH adjustments were made with hydrochloric acid. Silicon wafers (orientation ⟨100⟩, native oxide) were purchased from University Wafer. $TiO_2$ (99.99 % purity) sputtering targets were purchased from Kurt J. Lesker.

### Synthesis of Photo-initiator

4,4′-Azobis(4-cyanovaleric acid) (2.19 g, 7.8 mmol) was added to thionyl chloride (50 mL) under nitrogen atmosphere. The reaction mixture was refluxed for 15 min in a 100 °C oil bath. The hot solution was immersed in an ice bath and cooled to room temperature. Excess thionyl chloride was removed by vacuum evaporation at room temperature to yield a yellow solid. To the crude product was added 25 mL of dry tetrahydrofuran and the solution was bubbled with argon gas one hour to remove dissolved oxygen. In a separate flask, sodium borate decahydrate (2.97 g, 7.8 mmol) was dissolved in 18 MΩ water (40mL) and also deoxygenated with argon gas for one hour. Dopamine HCl (2.975 g, 15.7 mmol) was added to the water solution, followed by sodium carbonate (2.66 g, 25.11 mmol) and dissolved. The aqueous solution was kept

under inert atmosphere and chilled to 0 °C in an ice bath and stirred vigourously. The THF/cyanovaleric acid chloride solution was added dropwise to the chilled solution and stirred 24 hours. The reaction mixture was acidified to pH 2 using a 2 M HCl solution and washed three times with 30 mL portions of ethyl acetate. The ethyl acetate layers were collected, dried with $MgSO_4$, and evaporated to dryness. The crude product was purified by column chromatography using a mixture of ethyl acetate and hexane (2:1) as the eluent. The product was a yellow solid. 0.923g, 25.6 % yield. $^1$H NMR (DMSO $D_6$, 300 MHz) δ (ppm): 8.02 (br s, 1H, OH); 8.00 (br s, 1H, O*H*); 6.61 (d, 7.9 Hz, 2H, Arom.); 6.57 (s, 2H, Arom.); 6.44 (d, 8.0 Hz, 2H, Arom.); 6.34 (br s, 1H, N*H*); 3.18 (d, 5.9 Hz, 4H, C$H_2$NH); 2.54 (d, 7.6 Hz, 4H, C$H_2$CH$_2$NH); 2.38-2.24 (m, 8H, C$H_2$); 1.68 (s, 3H, C$H_3$); 1.64 (s, 3H C$H_3$). $^{13}$C NMR (DMSO $D_6$, 300 MHz) δ (ppm): 173.29, 145.70, 144.16, 130.81, 119.84, 116.58, 116.11, 72.62, 35.23, 33.94, 32.69, 30.71, 23.60, 21.42.

**Fabrication of $TiO_2$ Substrates**

Stripes of 1 cm wide $TiO_2$ were deposited onto clean silicon wafers by physical vapor deposition from a $TiO_2$ target using magnetron sputtering (PVD75, Kurt J. Lesker). Wafers were rinsed with isopropanol, nitrogen dried, and argon plasma cleaned (Harrick Plasma, PDC-001, 600 mTorr, 29.6 W) for 5 min prior to deposition. A tape mask was used to control the width of the stripe. The $TiO_2$ was deposited at 0.5 Å/s using a 50 W power setting and a 5 mTorr capman pressure. The thickness and optical properties of the native $SiO_2$ and $TiO_2$ were determined with spectroscopic ellipsometry.

**Growing pNIPAM Brushes**

$TiO_2$ substrates were rinsed with ethanol and DCM before being dried under a nitrogen stream prior to argon plasma cleaning (Harrick Plasma, PDC-32G, 600 mTorr,

18 W) for 5 min. The cleaned wafers were placed in 1 mg/mL catechol photo-initiator in methanol and kept in the dark overnight. Catechol monolayers were rinsed with methanol and nitrogen dried to remove any physisorbed material. Formation of the $TiO_2$ selective monolayer was confirmed by spectroscopic ellipsometry.

NIPAM was dissolved in degassed DCM in an air-free glove box at various weight fractions of monomer in a glass vial. $TiO_2$ substrates with catechol monolayers were placed into the NIPAM solution and the vial was sealed. Vials were transferred out of the glove box and into a UV light reactor (Rayonet, RPR-600, $\lambda$ = 350 nm). The surface bound photo-initiator created polymer on the surface and in solution. In order to remove physisorbed polymer, the contents of the vial were Soxhlet extracted in THF for 12 hrs. Polymer brushes were rinsed with THF and dried under a stream of nitrogen.

**Characterization**

Substrates were characterized by spectroscopic ellipsometry (M-2000V, J.A. Woollam Co., Inc.) after each film addition, reducing the number of variables required to fit the model over the spectral range, 380-1000 nm. *Ex situ* measurements were taken at 65°, 70°, and 75° angles of incidence in order to fit the refractive indices and film thicknesses of the dry pNIPAM brush using specialized software provided by the company. *In situ* measurements were performed in a custom flow cell at a 60° angle of incidence. The $\psi$ and $\Delta$ values were monitored as the temperature of the water within the cell was cycled between 25 °C and 50 °C.

Drug release experiments were monitored by UV-vis spectroscopy using a Varian 50 Bio spectrometer. Aliquots of the release medium (5x PBS at pH of 3.0) were scanned between 200 and 800 nm wavelengths to track the absorbance at $\lambda_{max}$ = 480 nm.

AFM images were taken using tapping mode on a Multimode NanoScope IIIa (Digital Instruments/Veeco Metrology) using silicon AFM probes with a 300 kHz resonant frequency and a 40 N/m spring constant.

Contact angles of water drops were measured (Kruss, DSA100) using a white light source and a CCD camera. The syringe was fixed to an automatic dispenser that controls the size and deposition of the droplet. The contour of a sessile drop is analyzed and fitted to the Young-Laplace equation using a contour tracing algorithm that distinguishes the drop from the surface. For statistical purposes, at least three drops were measured on each sample. The reported contact angles are the average of these measurements.

**Results and Discussion**

pNIPAM brushes were grown from a surface attached AIBN-catechol monolayer using photoinitiated free radical polymerization.[25] The thickness of the polymer brush was controlled by adjusting the monomer concentration in solution from 50 to 85 w/w % using a 24 hr exposure to 350 nm UV light at 1.25 mW/cm$^2$. A non-linear relationship between brush thickness and monomer concentration was observed in Figure 5.1. The exponential increase is attributed to the gel or Trommsdorff effect.[26-28] As the polymerization reaches high monomer conversion, the solution starts to gel due to the creation of polymer in solution, which decreases the diffusion rates of polymer end groups while leaving monomer diffusion unchanged. This increases the propagation rate relative to the rates termination, which results in a drastic increase in thickness. At high concentrations the gel effect is more pronounced due to the larger amount of monomer relative to initiator released into solution. Concentrations below 50 w/w % resulted in no

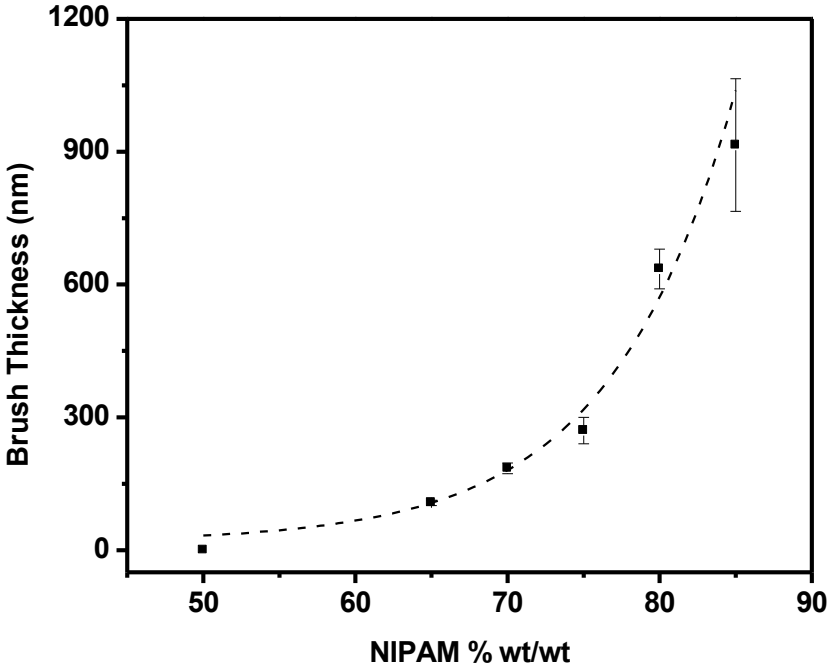


**Figure 5.1.** pNIPAM brush thickness relative to the weight percent of monomer in solution. Polymerization was carried our for 24 hrs under 350 nm UV light. The dashed line is meant to guide the eye.

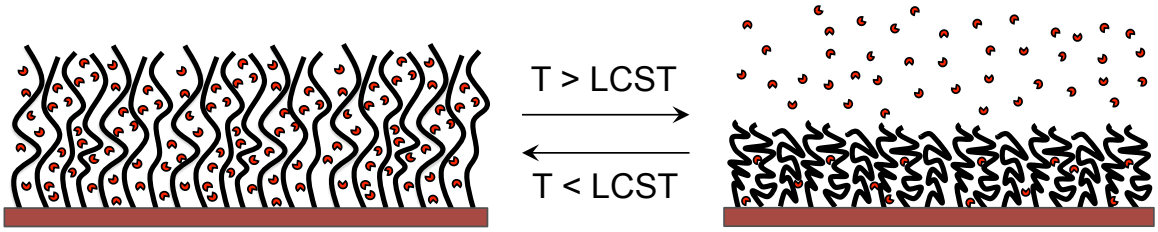


**Figure 5.2.** Diagram depicting the swelling and collapse of a thermo-responsive polymer brush as the temperature is cycled above and below the LCST. Red dots depict either solvent molecules or drug molecules.

polymer growth from the surface or in solution, which can be attributed to poor mass transport of monomer and initiator in the absence of convective mixing. The brush thickness was reproducible at all weight fractions where polymer formed as indicated by error bars in Figure 5.1.

When exposed to water, pNIPAM acts like a hydrogel at temperatures below the LCST absorbing water and swelling the polymer, as depicted on the left in Figure 5.2, while above the LCST the polymer will collapse. The morphological differences between the swollen and collapsed state are presented by the AFM images in Figure 5.3. The swollen brush image a) was taken after placing the substrate in 25 °C water for 1 hr, while the collapsed brush b) was heated on a hot plate at 50 °C. Any excess surface water was removed using a nitrogen stream after swelling and during heating. The RMS roughness of the swollen film was 6.80 nm, while the collapsed film had a roughness of

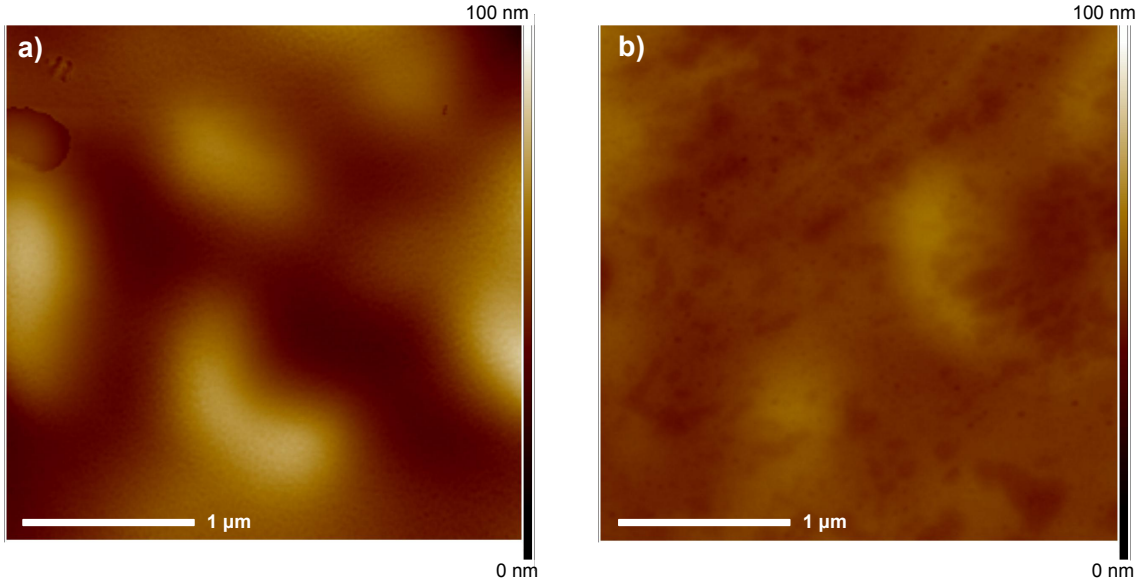


**Figure 5.3.** AFM images of a 120 pNIPAM film in the a) swollen and b) collapses states with RMS roughness of 6.80 nm and 3.29 nm, respectively.

3.29 nm for the 3 μm images. The ratio of swollen roughness to collapsed maintained a factor of 2 for multiple images. The larger roughness in the swollen state can be attributed to non-uniform heights of the polymer chains as they interact with the surrounding water.[14, 16, 29] When the polymer collapses on itself these chain ends are no longer in a diffuse state thus decreasing the surface roughness.

To understand the surface wettability of the pNIPAM brush above and below the LCST the contact angles at two different temperatures, 25 °C and 40 °C, were measured. After swelling the film at 25 °C for 1 hr, the top of the brush was cleared of any surface droplets with a moderate stream of nitrogen. In the swollen state, a contact angle of 62° was observed indicating a hydrophilic surface. Using a temperature above the LCST, 40 °C, the brush collapses, forcing out the water as the hydrogen bonding is disrupted. In the collapsed state pNIPAM is slightly hydrophobic with a contact angle of 73 °C. At temperatures below the LCST, pNIPAM chains stay in a brush conformation due to the hydrogen bonding with water and amide group increasing the hydrophilicity of the brush.[7] Above the LCST, the pNIPAM chains adopt a collapse confirmation due to the breaking of the hydrogen bonds with the amide group, increasing the hydrophobicity.[14, 30, 31] The reversibility of the stimuli-responsive swelling and collapse were investigated, Figure 5.4. The temperature cycle was performed several times and consistent contact angles below and above LCST verified the reversibility of the pNIAPM brushes.

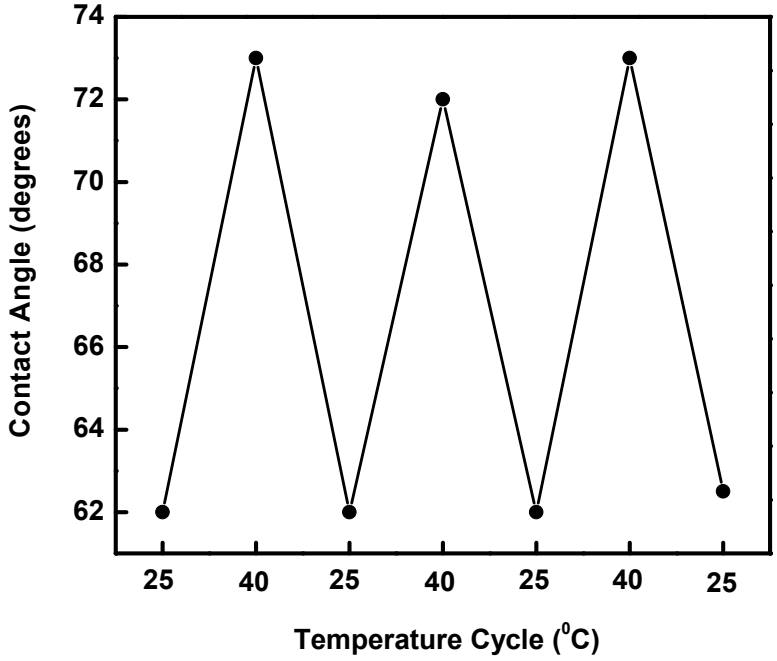


**Figure 5.4.** Contact angle response due to temperature cycling of the pNIPAM brush through the LCST. At 25 °C the brush is in the swollen state and collapses when carried above the LCST. A 40 °C water bath was used to bring the brush above the LCST.

Dynamic tracking of pNIPAM swelling was monitored by spectroscopic ellipsometry.[19] Polymer brushes were grown on 3 by 1.5 cm substrates with 1 cm wide $TiO_2$ stripes. Each layer was characterized by spectroscopic ellipsometry using *ex situ* measurements of $\psi$ and $\Delta$ and known refractive indices for the silicon, silicon oxide, and titanium oxide layers. The polymer film was characterized by fitting the brush thickness, refractive index, and extinction coefficient. The Cauchy model, Eq. 1, was used to fit the refractive index, n,[19, 30] while the Urbach equation, Eq. 2, was used to determine the extinction coefficient, k,[32]

$$n = A + \frac{B}{\lambda^2} + \frac{C}{\lambda^4} \quad (1)$$

$$k = k_o e^{D(E-B')} \quad (2)$$

where A, B, and C are Cauchy parameters and $k_o$ and D are Urbach parameters. Fitting the above model to $\psi$ and Δ spectra produced an average refractive index of 1.52 ± 0.03 and extinction coefficient of 0.04 ± 0.005 at a wavelength of 632.8 nm. Most organic film models assume a value of zero for the extinction coefficient indicating no light scattering within the film.[9] For thin pNIPAM films, 20-30 nm, fitting the extinction coefficient results in a zero value. Thicker films exhibit non-zero values, which can be attributed to light scattering due to the heterogeneity within the film.

The software, CompleteEASE, used to fit the model computes a mean square error (MSE) as an indicator on how well the model fits the data. When modeling the NIPAM brush layer, values for each parameter are estimated using standard values for organic materials and the software varies until a good fit is achieved. One way to monitor how well the model fits the data is by using the mean square error (MSE) between the data and the model. CompleteEASE uses the following equation to produce MSE values for each spectra as provided by the software manual,

$$MSE = 1000\left[\frac{1}{3n-m}\sum_{i=1}^{n}\left(\left(N_{D_i}-N_{M_i}\right)^2+\left(C_{D_i}-C_{M_i}\right)^2+\left(S_{D_i}-S_{M_i}\right)^2\right)\right]^{1/2} \quad (3)$$

$$N = cos(2\psi) \quad (4)$$

$$C = sin(2\psi)cos(\Delta) \quad (5)$$

$$S = sin(2\psi)sin(\Delta) \quad (6)$$

where n is the number of wavelengths, m is the number of fit parameters, D denotes the experimentally obtained data, and M indicates the model generated values. N, C, and S

are functions of $\psi$ and $\Delta$ as reported by Eq. 4-6. As reported in Eq. 3, a single MSE value is computed across all wavelengths for a single spectrum of $\psi$ and $\Delta$.

*In situ* tracking of the hydrogel swelling and collapse was performed at a 60° incident angle in a custom flow cell. The substrate was immersed in 18 MΩ $H_2O$ at 25 °C for 1 hr to ensure that the polymer brush was intercalated with water. Spectral curves of $\psi$ and $\Delta$ were taken for several minutes prior to flowing in 50 °C water followed by a rinse with 25 °C water. Flowing in water above the LCST produces a change in $\psi$ and $\Delta$ due to polymer collapse, as shown in Figure 5.5. In tracking mode the spectroscopic ellipsometer takes complete spectral data at each time interval. The dynamic data was modeled using Eq. 1 and 2 using dry film parameters as an initial guess for the solvated layer. Changing the Cauchy and Urbach parameters produces the fits shown in Figure 5.5 for the swollen and collapsed film. The dynamic measurement was modeled at each time interval for thickness, refractive index, and extinction coefficient which are reported in Figure 5.6. Injecting water above the LCST produces an immediate response in the polymer as indicated by the drastic decrease in brush thickness from 90 nm to 72 nm at 2 min. These changes in thickness are consistent with that reported in literature.[13, 14, 30, 33, 34]

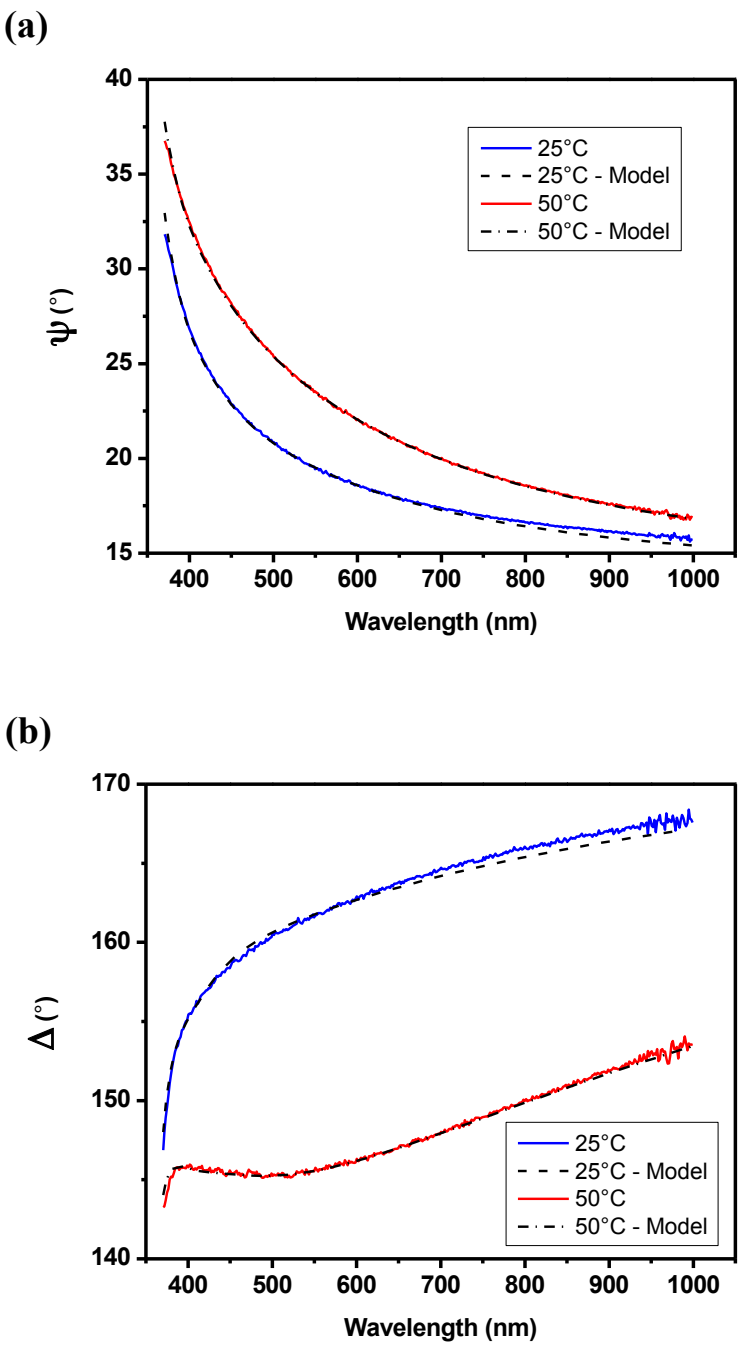


**Figure 5.5.** Spectropscopic ellipsometry values of $\psi$ and $\Delta$ for pNIPAM swelling and collapse due to temperature changes between 25 °C and 50 °C. Dashed lines represent modeled values of $\psi$ and $\Delta$ from fitted parameters; film thickness, refractive index, and extinction coefficient.

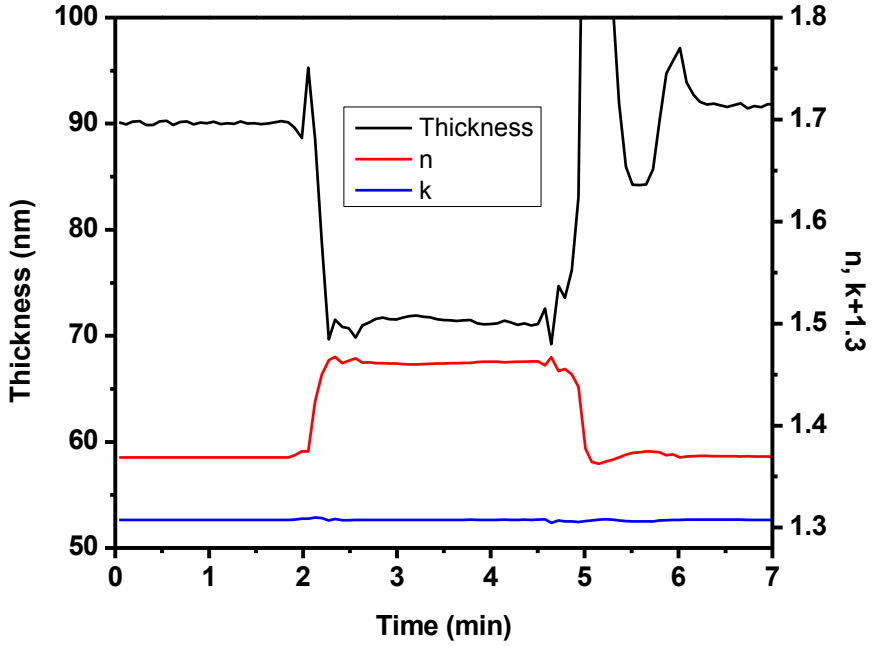


**Figure 5.6.** *In situ* spectroscopic elliposometry tracking NIPAM collapse due to solvent temperature changes. Thickness, refractive index, and extinction coefficients are derived from modeling $\psi$ and $\Delta$ values. The film collapses when 50 °C water is injected at 2min. Replacing the solvent with 25 °C water swells the polymer to the starting thickness after a period of rearrangement.

Substantial changes in the film's refractive index are also observed. In the dry state the polymer brush has a refractive index of 1.52. The refractive index of the hydrogel resembles that of a polymer-water mixture producing an effective refractive index for the brush layer that is lower than the dry polymer.[9, 19, 30, 35, 36] When the brush collapses, the polymer contracts squeezing water out of the film and the effective refractive index for the layer increases towards that of the dry film. Changes in the

extinction coefficient are not observed indicating similar light scattering properties for the swollen and collapsed film. In Figure 5.6, an adjustment factor of 1.3 was used to plot the extinction coefficient on the same scale as refractive index. The extinction coefficient during the dynamic tracking fluctuates within the error range reported for the dry film, $k = 0.04 \pm 0.005$, and was attributed to similar scattering within the dry and solvated films.

In the swollen and collapsed states the MSE is less than 5 indicating an accurate fit of the reported thickness and complex refractive index from Figure 5.6. Where the modeled brush thickness exceeds the swollen thickness correspond to a large increase in MSE, Figure 5.7. The 5 to 6 min region where the film under goes rearrangement the MSE increases drastically indicating a deviation from an ideal fit. This can be attributed to an inadequacy of a block layer model for tracking the submicron polymer rearrangements that occur within the film. As the water is cycled above and below the LCST, a temperature gradient forms within the polymer brush. The differential layers that form along the gradient during polymer chain rearrangement are not incorporated within the block layer model thus causing the observed fluctuations.

When exposed to 50 °C water, the temperature gradient rapidly collapses the brush from the top-down. During collapse the heat transfer rate through the brush is facilitated by interaction between polymer chains at higher temperatures with those below at lower temperature. The proximity of the chains during heating improves the interaction between polymer side groups as hydrogen bonding between chains becomes more prevalent. Alternatively, the rate of swelling will be drastically decreased from the collapse rate due to entropic limitations as the polymer brush uncoils from the collapsed

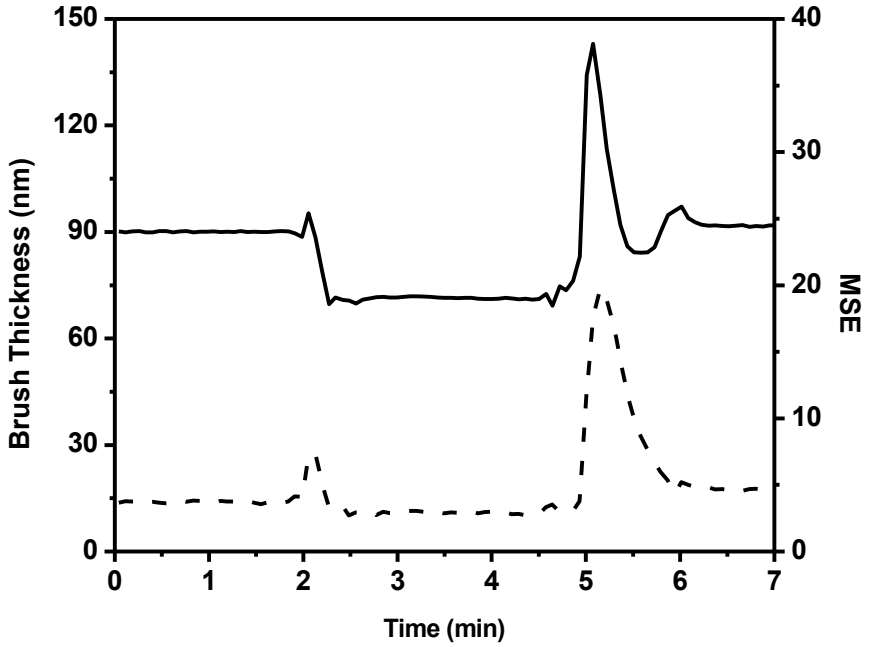


**Figure 5.7.** Modeled NIPAM brush thickness (solid line) and MSE (dashed line) across the dynamic time frame. Where the hydrogel thickness exceeds the swollen brush thickness an increase in the MSE is also observed.

state. Re-swelling of the pNIPAM not only involves the rearrangement of the polymer brush but the diffusion of water into the polymer to form the preferential hydrogen bonding with water.[14, 34] Using a temperature of 50 °C the polymer contracts completely within 25 seconds, Figure 5.6. Injecting 25 °C water at 4.5 min the polymer is taken below the LCST and the film again swells to a 0.80 water volume fraction in ~30 sec with rearrangements occurring for another 30 sec thereafter. For each case, collapse or swelling, changes in a 90 nm film occured rapidly.

Polymer brush thickness will effect the time it takes for the rearrangements to occur during swelling. The variance in these rates are observed with a 268 nm swollen polymer brush over repeated temperature cycling between 25 °C and 40 °C, Figure 5.8. With a lower hot water bath, the system had begun to cool due to heat loss to the surrounding environment. As the water bath cooled towards the LCST, the film began to swell as can be seen by the slow increase in thickness and decrease in refractive index after each initial collapse at t = 9, 67, and 115 min. Injection of water at 25 °C, increased the swelling rate causing a similar fluctuation in the measurements as previously

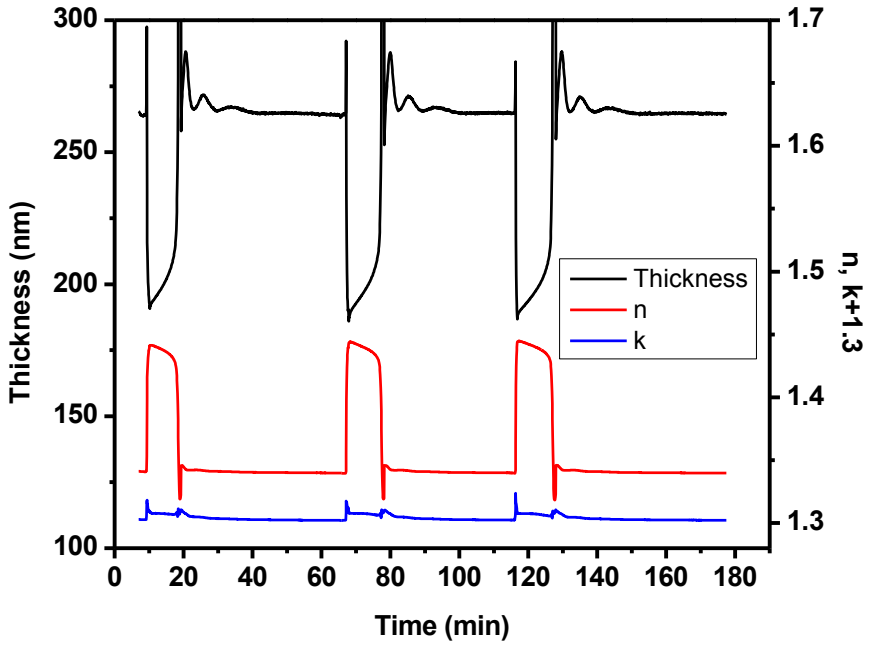


**Figure 5.8.** *In situ* tracking of NIPAM film swelling and collapse due to solvent temperature changes when cycled between 25 °C and 40 °C in triplicate. As the 40 °C water cools towards the LCST, the brush starts to undergo rearrangement as indicated by the increasing thickness once the polymer is collapsed.

observed. However, with the thicker pNIPAM film the fluctuations in the modeled data continue for 10 min before stabilizing to the swollen state while the collapse occurred within the same timeframe as the thinner film. With similar collapse time frames for 90 nm and 268 nm films, the rate of drug delivery can occur expeditiously which is imperative in single dose releases. Muti-dosing with thermo-repsonsive films can be peformed by removing the heat source returning the polymer to the swollen state. In this case the time difference in the swelling rates for the different brush thicknesses will limit how fast multiple doses can be administered.

While using a block layer model does not accurately describe the swelling region, limiting the organic brush model to a single layer does provide the effective refractive index for the polymer layer in the swollen and collapsed state.[9, 19, 35] The pNIPAM film is actually a mixture of water and polymer each with distinct refractive indices and volume fractions. By applying the Maxwell-Garnett effective medium approximation[37, 38], Eq. 7,

$$\frac{n_m^2 - n_p^2}{n_m^2 + 2n_p^2} = \phi_w \frac{n_w^2 - n_p^2}{n_w^2 + 2n_p^2} \quad (7)$$

where $n_p$ and $n_w$ are the refractive indices for NIPAM and water, and $n_m$ is the modeled refractive index profile, was applied to the dynamic data in Figure 5.6 to compute the water volume fraction $\phi_w$ shown in Figure 5.9. The refractive index of the dry polymer was used for $n_p$ and a value of 1.33 was used for $n_w$.[9, 19, 30, 35] Below the LCST the hydrogel is swollen with a 0.80 water volume fraction, which is comparable to literary values for pNIPAM.[9, 19, 22] In the collapsed state, above the LCST, the polymer film contains a 0.30 water volume fraction indicating that not all the water is released during polymer contraction. The water that remains within the film can be intercalated with the

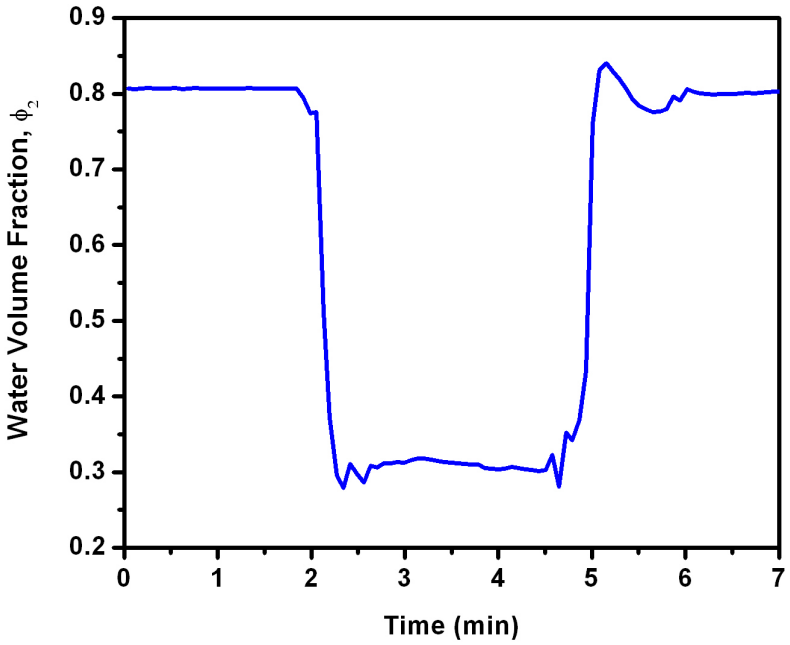


**Figure 5.9.** Volume fraction of water in the NIPAM brush as computed by the Maxwell-Garnett effective medium approximation. The dynamic data starts out with a swollen brush at 25 °C. Water is released when the film contracts reducing the volume fraction in the thinner collapsed film.

polymer chains as individual molecules or trapped water pockets created during polymer collapse. Any drug molecule loaded into the polymer with the water will also be trapped thus decreasing the effective release amount.

The pNIPAM brush releases water when going from a swollen to a collapsed volume. In order to estimate the amount of water lost compared to the swollen state the difference in volumes $V$ needs to be taken into account using Eq. 8,

$$x_{lost} = \frac{\phi_{w,S}V_S - \phi_{w,C}V_C}{\phi_{w,S}V_S} \quad (8)$$

where $\phi_w$ indicates the water volume fraction while S and C subscripts denote the swollen and collapsed states of the brush, respectively. During dynamic tracking, the spectroscopic ellipsometer tracks the same area of the polymer brush, thus the area of the swollen and collapse film are the same, $A_S = A_C$, which reduces the volume terms in Eq. 8 to a function of brush thickness, Eq. 9,

$$x_{lost} = \frac{\phi_{w,S} h_S - \phi_{w,C} h_C}{\phi_{w,S} h_S} \quad (9)$$

where h is the brush thickness. In raising the temperature above the LCST, the 90 nm hydrogel loses ~70 % of the water contained in the swollen polymer due to contraction. With a known amount of water released within the initial collapse the instantaneous delivery of any water-soluble drugs can be computed relative to the amount of water contained within the hydrogel.

Drug release experiments were performed using doxorubicin as a modal drug using techniques previously utilized with microgel thin films.[11, 18] pNIPAM brushes were loaded with the cancer drug by cycling the brush above and below the LCST in the presence of 80 μM DOX in 5x PBS solution at pH 7.0. The repeated collapse and swelling of the brush increases the rate in which the drug was loaded relative to diffusion limited loading by using the mechanical changes in the film. During swelling the polymer takes on any water to reach a thermodynamic equilibrium in the swollen state. By using water loaded with DOX, the brush takes on both water and the drug molecule simultaneously upon swelling. Constant contraction and expansion of the pNIPAM film expel and replenishes the water within the film to intercalate the polymer with a uniform concentration. Once loaded, the pNIPAM films were rinsed with water and placed into the release solution (5x PBS). Storing the substrates in PBS was performed over several

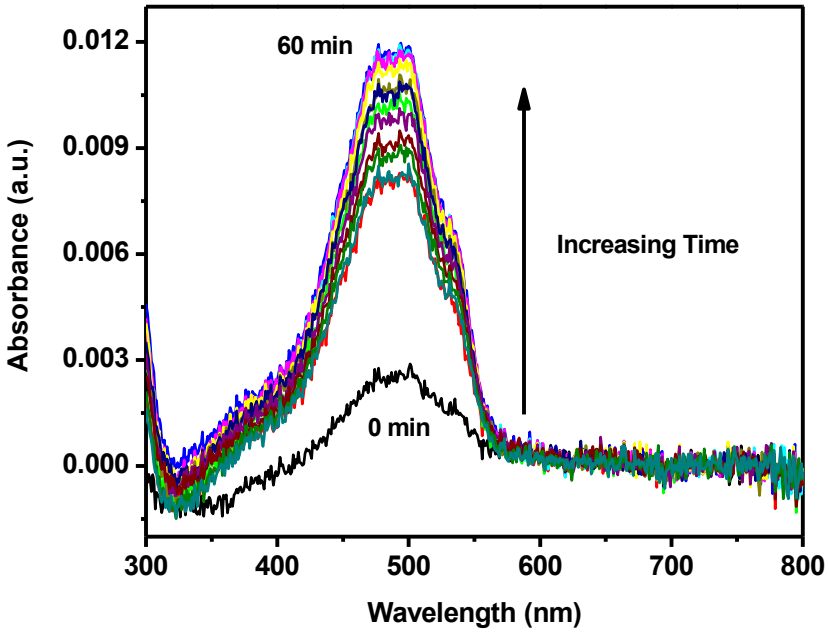


**Figure 5.10.** UV-vis absorbance of DOX release from a 150 nm pNIPAM film. Aliquots of the release medium were measured at various intervals over 3 hours. The maximum absorbance was observed within 60 min of exposing the pNIPAM film to water at 50 °C.

days to determine if DOX would be released from the film. Aliquots of the storage solution were measured by UV-vis after 24 hrs and exhibited no significant increase in absorbance at 480 nm relative to the solution background.

Controlled release of the DOX from a 150 nm pNIPAM film was performed using a 50 °C water bath to maintain uniform temperature on all sides of a submersed vial. The vial was filled with 10 mL of 5x PBS solution and a stir bar to provide complete mixing during the release. Once heated to 50 °C, a 1 $cm^2$ pNIPAM substrate was placed into the release solution. A 1 mL aliquot was taken as the substrate was placed into the hot

solution and the UV-vis spectrum was recorded once the solution had cooled to room temperature, Figure 5.10 black line. The presence of the absorption peak at 480 nm indicates that the pNIPAM began to collapse upon immediate exposure to the hot solution releasing DOX. Subsequent aliquots were taken at 15 min time intervals at the start of the release and at 7 min intervals after the first hour. The increasing absorbance due to DOX release from the continuously collapsed brush is presented in Figure 5.10. The maximum absorbance was observed after 60 min of exposure to the hot water solution.

With a maximum absorbance in the release time of 60 min, the drug release data seemingly contradicts the spectroscopic ellipsometry data, which indicates the collapse is complete within 30 sec. However, the disparity between the data lies in the experimental conditions of the drug release. By continuously releasing into the same solution the concentration measured by UV-vis is an indication of the cumulative release at each time interval. Similarly, with a 10 mL starting volume the 1 mL aliquot sampling would deplete the release solution within 10 measurements. In order to offset this and extend the measurement time frame, 1 mL of 50 °C PBS solution was added to the vial to maintain a 10 mL volume. By maintaining a constant volume while removing a 10 % of the cumulative solution will dilute the sample over time. This can be seen by plotting the absorbance at $\lambda_{max}$ = 480 nm relative to the sampling times, Figure 5.11 black data. The absorbance plateaus at 60 min before starting to decrease, which is indicative of beginning to form the serial dilution. The limit at which serial dilution takes over as the dominate measurement can be computed when the linear portion of the kinetic data approaches the red line in Figure 5.12.

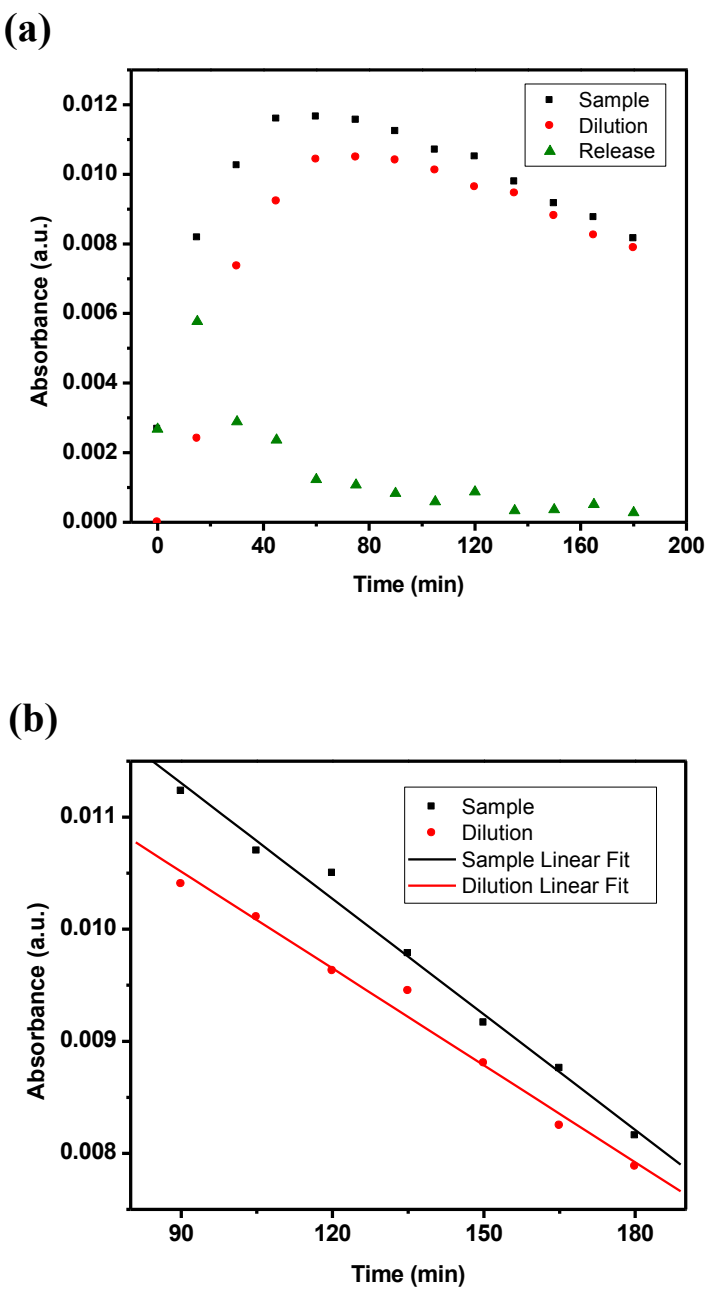


**Figure 5.11.** Kinetic release rate of DOX from a 150 nm pNIPAM film. a) Data in black is taken at λ = 480 nm from the UV-vis spectrum and is the cumulative DOX in the release medium. Serial dilution effects are computed and reported as red data points. Net DOX release between each aliquot is reported as green data points. b) Serial dilution becomes the dominant change in absorbance as the black line approaches the red.

While the recorded data is the cumulative release, the absorbance from each sampling can be computed by adjusting for the serial dilution effects shown in red. Subtraction of the absorbance due to dilution from the cumulative absorbance yields the amount of DOX released at each time interval, Figure 5.11 green data points. While the maximum absorbance was achieved at the end of an hour of continuous pNIPAM collapse, the maximum release was observed within the first 15 min. The non-zero absorbance at the time the substrate was submersed (t = 0 min) also indicates a rapid collapse of the pNIPAM film, which is comparable to the spectroscopic ellipsometry data. The incremental release of DOX decreases over time after the initial 15 min. This trickle release is attributed to gradual changes in the polymer film that cause the chains to reduce the hydrogen bonding with water and increase the polymer-polymer interaction. As the polymer chains adjust, water pockets trapped within the film are forced out releasing the minute amounts of DOX contained within the sequestered pockets.

The concentration per area of drug released from the pNIPAM film was computed from the maximum absorbance in Figure 5.11 using the Beer-Lambert Law, Eq. 10,

$$A = \varepsilon l c \tag{10}$$

where $\varepsilon$ is the emissivity, $l$ is the thickness of the polymer brush, and $c$ is the concentration. With an emissivity of 11500 $cm^{-1}M^{-1}$ at $\lambda$ = 480 nm[39-41] and a 150 nm polymer film, a concentration of 1.04 $nmol/cm^2$ was released from the pNIPAM brush. During collapse the film maintains a water content leaving 30 % trapped within the film, which can be used in a second drug release. The amount of drug loaded into the film can be estimated from the quantity released. For the 150 nm film, a maximum of 1.48 $nmol/cm^2$ can be loaded into the film.

## Conclusions

The dynamics of a thermo-responsive, thin film polymer have been determined using optical techniques to investigate the amount of water contained within a hydrogel. Using *in situ* spectroscopic ellipsometry, a pNIPAM film was monitored as the polymer brush was collapse and swollen. By fitting the spectral $\psi$ and $\Delta$ data an accurate model was produced for the swollen and collapsed film using a single effective medium approximation for the refractive of the thin film. While this model, was adequate for a polymer in equilibrium with an MSE value less than 5, the rearrangement of the polymer chains produced deviations in the fit during polymer swelling. Applying effective medium theory to the changes in refractive index of the thin film yielded an estimate on the water content within the polymer brush. In the swollen state the polymer contains approximately 80 % water, while in the collapsed state 30 % water remains located in sequestered regions of the brush where the water cannot be forced out of the brush. Using a cycling method, a hydrogel pNIPAM film was loaded with a water-soluble drug, doxorubicin, which has an absorbance in the visible range. Once loaded, the drug was expelled from the polymer by collapsing the film and producing a maximum cumulative release within 60 min. Analysis of the release profile indicated that the largest incremental release occurred within 15 min with a rapid increase as the polymer was exposed to 50 °C water. With a 70 % water loss from the polymer brush and maximum absorbance of 0.012, the amount of drug released in a single collapse of a 150 nm brush was determine to be 1.04 nmol/ $cm^2$. In knowing the effective drug loadings and release rates from thermo-responsive polymers, thin film drug delivery systems can be tailored to carry the appropriate amount of water-soluble drug for patient treatment.

## References


1. Ulbricht, M., *Polymer* **2006,** *47* (7), 2217-2262.

2. Ionov, L.; Minko, S.; Stamm, M.; Gohy, J.-F.; Jérôme, R.; Scholl, A., *J. Am. Chem. Soc.* **2003,** *125* (27), 8302-8306.

3. Ionov, L.; Sapra, S.; Synytska, A.; Rogach, A. L.; Stamm, M.; Diez, S., *Adv. Mater.* **2006,** *18* (11), 1453-1457.

4. Kumar, A.; Srivastava, A.; Galaev, I. Y.; Mattiasson, B., *Prog. Polym. Sci.* **2007,** *32* (10), 1205-1237.

5. Rzaev, Z. M. O.; Dinçer, S.; Piskin, E., *Prog. Polym. Sci.* **2007,** *32* (5), 534-595.

6. Stuart, M. A. C.; Huck, W. T. S.; Genzer, J.; Muller, M.; Ober, C.; Stamm, M.; Sukhorukov, G. B.; Szleifer, I.; Tsukruk, V. V.; Urban, M.; Winnik, F.; Zauscher, S.; Luzinov, I.; Minko, S., *Nat Mater* **2010,** *9* (2), 101-113.

7. Zhou, F.; Huck, W. T. S., *PCCP* **2006,** *8* (33), 3815-3823.

8. Friebe, A.; Ulbricht, M., *Macromolecules* **2009,** *42* (6), 1838-1848.

9. Junk, M. J. N.; Anac, I.; Menges, B.; Jonas, U., *Langmuir* **2010,** *26* (14), 12253-12259.

10. Yan, H.; Tsujii, K., *Colloids and Surfaces B: Biointerfaces* **2005,** *46* (3), 142-146.

11. Serpe, M. J.; Yarmey, K. A.; Nolan, C. M.; Lyon, L. A., *Biomacromolecules* **2004,** *6* (1), 408-413.

12. Wu, C.; Wang, X., *Phys. Rev. Lett.* **1998,** *80* (18), 4092.

13. Vidyasagar, A.; Majewski, J.; Toomey, R., *Macromolecules* **2008,** *41* (3), 919-924.

14. Yim, H.; Kent, M. S.; Mendez, S.; Balamurugan, S. S.; Balamurugan, S.; Lopez, G. P.; Satija, S., *Macromolecules* **2004,** *37* (5), 1994-1997.

15. Laloyaux, X.; Mathy, B.; Nysten, B.; Jonas, A. M., *Langmuir* **2009,** *26* (2), 838-847.

16. Estillore, N. C.; Park, J. Y.; Advincula, R. C., *Macromolecules* **2010,** *43* (16), 6588-6598.

17. Orski, S. V.; Fries, K. H.; Sontag, S. K.; Locklin, J., *J. Mater. Chem.* **2011,** *21* (37), 14135-14149.

18. Vasani, R. B.; McInnes, S. J. P.; Cole, M. A.; Jani, A. M. M.; Ellis, A. V.; Voelcker, N. H., *Langmuir* **2011,** *27* (12), 7843-7853.

19. Bittrich, E.; Burkert, S.; Müller, M.; Eichhorn, K.-J.; Stamm, M.; Uhlmann, P., *Langmuir* **2012,** *28* (7), 3439-3448.

20. Jia, X.; Jiang, X.; Liu, R.; Yin, J., *Macromol. Chem. Phys.* **2009,** *210* (21), 1876-1882.

21. Edmondson, S.; Osborne, V. L.; Huck, W. T. S., *Chem. Soc. Rev.* **2004,** *33* (1), 14-22.

22. Jones, D. M.; Smith, J. R.; Huck, W. T. S.; Alexander, C., *Adv. Mater.* **2002,** *14* (16), 1130-1134.

23. Barbey, R.; Lavanant, L.; Paripovic, D.; Schüwer, N.; Sugnaux, C.; Tugulu, S.; Klok, H.-A., *Chem. Rev.* **2009,** *109* (11), 5437-5527.

24. MILNER, S. T., *Science* **1991,** *251* (4996), 905-914.

25. Tulevski, G. S.; Miao, Q.; Fukuto, M.; Abram, R.; Ocko, B.; Pindak, R.; Steigerwald, M. L.; Kagan, C. R.; Nuckolls, C., *J. Am. Chem. Soc.* **2004,** *126* (46), 15048-15050.

26. Tulig, T. J.; Tirrell, M., *Macromolecules* **1981,** *14* (5), 1501-1511.

27. Arnold, R. M.; Sheppard, G. R.; Locklin, J., *Macromolecules* **2012,** *45* (13), 5444-5450.

28. Prucker, O.; Rühe, J., *Macromolecules* **1998,** *31* (3), 602-613.

29. Cullen, S. P.; Mandel, I. C.; Gopalan, P., *Langmuir* **2008,** *24* (23), 13701-13709.

30. Plunkett, K. N.; Zhu, X.; Moore, J. S.; Leckband, D. E., *Langmuir* **2006,** *22* (9), 4259-4266.

31. Annaka, M.; Yahiro, C.; Nagase, K.; Kikuchi, A.; Okano, T., *Polymer* **2007,** *48* (19), 5713-5720.

32. Dow, J. D.; Redfield, D., *Physical Review B* **1972,** *5* (2), 594-610.

33. Kidoaki, S.; Ohya, S.; Nakayama, Y.; Matsuda, T., *Langmuir* **2001,** *17* (8), 2402-2407.

34. Liu, G.; Zhang, G., *The Journal of Physical Chemistry B* **2004,** *109* (2), 743-747.

35. Toomey, R.; Freidank, D.; Rühe, J., *Macromolecules* **2004,** *37* (3), 882-887.

36. Toomey, R.; Mays, J.; Tirrell, M., *Macromolecules* **2004,** *37* (3), 905-911.

37. Mallet, P.; Guérin, C. A.; Sentenac, A., *Physical Review B* **2005,** *72* (1), 014205.

38. Ruppin, R., *Optics Communications* **2000,** *182* (4-6), 273-279.

39. Zeman, S. M.; Phillips, D. R.; Crothers, D. M., *Proceedings of the National Academy of Sciences* **1998,** *95* (20), 11561-11565.

40. Missirlis, D.; Kawamura, R.; Tirelli, N.; Hubbell, J. A., *European Journal of Pharmaceutical Sciences* **2006,** *29* (2), 120-129.

41. Eliaz, R. E.; Szoka, F. C., *Cancer Research* **2001,** *61* (6), 2592-2601.

# CHAPTER 6

# CONCLUSIONS AND OUTLOOK

In this dissertation, a variety of label-free tracking techniques were explored as a means to probe interfacial interactions of polymer thin films. These interactions can take a variety of forms from polymer-solvent interactions to chemical reactions within the polymer film. The optical techniques employed in these studies have focused on monitoring these interactions by tracking the changes in refractive index and thickness of the polymer films. While surface plasmon resonance (SPR) and spectroscopic ellipsometry are well known optical techniques the study of *in situ* polymer dynamics can become complex as the different layers interact inducing unique shifts in the data.

The effects of the various changes that occur during in situ label-free tracking are explored in Chapter 1. While both SPR and ellipsometry monitor changes in reflectivity their interaction with the films are distinctively different. In the standard Kretschmann configuration, SPR monitors interactions within the thin film using backside reflection tracking as the light is coupled to a thin noble metal surface using a prism. The optical properties of each dielectric layer and the subsequent variations of refractive index and thickness within the layer model were discussed as a template from which any *in situ* SPR tracking can be established. While SPR is the more sensitive of the two techniques, the evanescent wave decay length limits the thicknesses that can be monitored. Alternatively, spectroscopic ellipsometry uses an optically thick reflective surface to

reflect the light being passed through the film. Utilizing the wavelength dependence of the optical properties, this method can deconvolute the refractive index and thickness of polymer thin films.

During the progression toward a comprehensive understanding of *in situ* dynamics of polymer thin films it is crucial to not only fully characterize each layer but to control the delivery of any external stimulus or reactive analyte. Chapter 2 focused on the development of a microfluidic system that could be coupled with surface plasmon resonance imaging (SPRI). Prior to this work, the common material to use for microfluidic devices was poly(dimethylsiloxane) (PDMS) which exhibited poor adhesion to gold and is incompatible with many organic solvents. In order to expand SPRI microfluidics to the organic solvents used in polymeric reactions, a photolithographic methodology was developed to utilize thiolene resins. Thiolene was used as a positive photoresist to create channels on a glass slide rather than on the SPRI substrate leaving the gold sensor surface free of contamination and available for surface modification by self-assembly. Microfluidic SPRI devices were able to maintain high flow rates and have excellent compatibility with a broader range of solvents. The sensitivity of the sensing surface was explored by tracking the detection of 150 nM streptavidin binding to biotinylated monolayers.

The protein binding event monitored in the thiolene microfluidic device tracked the changes in thickness as streptavidin was attached to the surface. SPRI can also track the changes in refractive index of the dielectric material that is in contact with the noble metal surface. In Chapter 3, the refractive index increments of polymers were determined by using a novel microfluidic design. A linear concentration gradient was

produced *in situ* by combining two streams containing different quantities of polymer. The combined streams were mixed within the microfluidic channels by inducing turbulent back flow caused by baffles along the channels. Seven concentrations were produced with a three-stage linear mixer device that is less than 2 $cm^2$. The refractive index of each channel was tracked simultaneously by SPRI. Analyzing the change in pixel intensity at the end of each channel produces a linear line from which the refractive index increment was computed. For 50 mg/mL poly(ethylene glycol) sample, the refractive index increment was determined to be 0.138 mL/g by the SPRI linear gradient mixer, which was within 3 % of the value reported in literature. With this linear mixer design, polymers with unknown refractive index increment can be determined improving other analytical techniques such as gel permeation chromatography and light scattering, which depend on the refractive index increment to determine a polymer's molecular weight and hydrodynamic size.

In Chapter 4, the grating structures found on optical storage media, such as blu-ray discs, were used to generate SPR when coated with a noble metal. While CDs and DVDs can also generate SPR, the 320 nm corrugations on the blu-ray disc produce a single plasmon dip for chemical sensing through a molecularly imprinted polymer attached to the surface of a silver coated disc. Imprinted polymers are formed by polymerizing monomers containing hydrogen bonding moieties in the presence of a target molecule produces a synthetic antibody that is distinct to the imprinted molecule. The resulting polymer was grown from the surface in a "grafting through" approach by using a surface bound monomer to attach the polymer to the silver. The addition of the polymer layer shifted the plasmon dip caused by the negative first diffraction to lower

angles of incidence. Removal and rebinding of two imprinted small molecule toxins, histamine and microcystin-LR, were shown to induce a plasmon shift of 0.4° and 2.1°, respectively. Modeling the plasmon shift by rigorous coupled wave analysis determined that the change in the dip angle was caused by a 0.005 and 0.02 change in refractive index. Exposing the binding imprinted polymer to analogous molecules produced no shift for the histamine sensor and slight shifts for microcystin sensor due to solvation of the larger binding cavity. By incorporating the selectivity of molecular imprinting with grating coupled SPR, a cost effective chemical sensor was produced using blu-ray discs.

Chapter 5 tracks the dynamic changes of a stimuli-responsive hydrogel, poly(N-isopropyl acrylamide) (pNIPAM), as the film undergoes a mechanical rearrangement induced by temperature. As a thermo-responsive polymer, pNIPAM exhibits a lower critical solution temperature (LCST) above which the polymer collapses in the presence of water and swells below the LCST. With a LCST of 32 °C, pNIPAM is an attractive stimuli-responsive polymer for the use in water-soluble drug delivery. Upon collapse, the water contained within the hydrogel is forced out along with any drug loaded into the film. Hydrogel films were analyzed by spectroscopic ellipsometry to determine the amount of water contained within a pNIPAM brush. Effective medium approximations were applied to dynamic tracking of a polymer as it was cycled through the LCST *in situ*. It was determined that the pNIPAM film lose 70 % of its water content upon collapse. Applying the amount of water expelled from the brush to a release profile of a chemotherapeutic drug, doxorubicin, an effective delivery dose of 1.04 nmol/cm$^2$ was delivered from a 150 nm film in 60 min.

In summary, this dissertation has provided a foundation of the fundamental principles from which any organic thin film can be monitored by *in situ*, label-free optical techniques. With the development of a robust microfluidic device, we have been able to expand lab-on-a-chip devices to be able to track reactions in aqueous and organic solvents while maintaining clean surfaces for interfacial reactions. SPRI microfluidic devices were utilized to track the refractive index increments of polymers in solution by generating a linear concentration gradient *in situ*. Expanding the use of these devices to incorporate parallel analysis or air free reactions can lead to the monitoring of the formation of polymers as they are grown from the surface.

Employing blu-ray discs as a grating SPR sensor we were able to monitor the binding of small molecule toxins within a molecular imprinted polymer by tracking the changes in refractive index. While grating SPR has been known for some time, it's implementation as a sensing mechanism has been limited and only recently has been utilized in areas such as chemical sensing and dye-sensatized solar cells. However, in order to distinguish between simultaneous changes in refractive index and thickness a multiple incident angle and wavelength technique is required. A spectroscopic ellipsometer was used to monitor the dynamic changes within a thermo-responsive hydrogel. While this study focused on a polymer-solvent interaction, the methodologies presented can be applied to other interfacial reactions such as post-polymerization functionalization of activated ester polymer brushes or the phase separation of polymer blends.

In conclusion, as research in polymer thin films continues to expand, how the polymers interact with the local environ will dictate the efficacy of the films as adequate sensing and diagnostic tools. Label-free optical techniques can assist in elucidating the dynamic changes that the polymer thin films undergo, whether it be polymer-solvent, polymer-polymer, or polymer analyte interactions. The fundamental methodologies for tracking *in situ* reactions by SPR and spectroscopic ellipsometry presented in this dissertation can be applied to illuminate the complex interactions that can occur within polymer thin films.